General two-dimensional linear flows of particle suspensions

Thomas Roger Brickell

DEPARTMENT OF MATHEMATICS
UNIVERSITY COLLEGE, LONDON

A THESIS PRESENTED FOR THE DEGREE OF
MASTER OF PHILOSOPHY

SUPERVISOR
Dr Helen Wilson

February 2012

I, Thomas Roger Brickell, confirm that the work presented in this thesis is my own. Where information has been derived from other sources, I confirm that this has been indicated in the thesis.

SIGNED

Contents

Acknowledgements

I would primarily like to acknowledge my supervisor Helen Wilson. Dr Wilson has show massive patience throughout the course of this PhD. I have grown as a mathematician under her supervision and her knowledge still continues to amaze me. As well as providing academic support she has been invaluable in helping me keeping my sanity. I would further particularly like to thank her for the gargantuan effort Dr Wilson has made in the final days and weeks of my PhD, whilst heavily pregnant still guiding me through the final stages, always on hand with a email.

I am indebted to the Engineering and Physical Sciences Research Council for the financial support received without which I would have not been able to embark on my research.

The department in which I work has been inspiring and fun and for that I would like to thank all of the postgraduates and staff at UCL mathematics department.

The support of my mother, Gill, father, Roger and girlfriend, Jo has been essential to push me through the PhD and this represent yet another debt I will struggle to ever repay.

Abstract

This thesis investigates the flow of suspensions of solid spheres in a viscous fluid. We look at a monolayer of particles in an unbounded fluid, and carry out numerical simulations of its behaviour under a variety of linear flows.

In chapter 1 we review the field and discuss the different approaches to simulating a suspension of solid spheres in a viscous fluid. We outline the case for the method of Stokesian Dynamics, and explain its derivation.

In chapter 2 we introduce the concept of a spatially periodic lattice which self-replicates in time under flow. We then go on to derive a suitable periodic box for each possible two dimensional linear flow, from pure strain to pure rotation, through simple shear and flows of intermediate type.

Using the numerical method of Stokesian Dynamics, in chapter 3 we proceed to investigate the macroscopic properties of our two-dimensional suspension in the various flows. The viscosity and normal stress difference are probed at both short and long times. We find evidence of crystallisation, and our major discovery is that crystallisation sets in earlier (in terms of increasing concentration) for flows that are closer to shear flow than those with a larger component of rotation or of strain. We also present results on the duration of transients in start up flow.

In chapter 4 we consider the effects of surface roughness on viscosity. Two different models for roughness are considered, the usual hard contact and a new soft contact model first proposed by Wilson in [65]. A comparison of the results of the two models is undertaken and we discuss about the effects of lower viscosity occurring at low concentrations due to surface roughness.

In Appendix A we consider the method of Ewald summation which can be used to properly account for far-field interactions in a lattice-periodic system, and derive the relevant forms for a system which is periodic in only two dimensions. Unfortunately we discover a problem with the Hankel transform but the real space relations are still valid. This will have application both to monolayer systems such as the one we have studied, and to confined suspensions in a variety of applications where the relevant geometry has a large aspect ratio.

List of Figures

List of Tables

Chapter 1

Introduction and Background

1.1 Introduction

In this thesis we shall be looking at the area of suspended particles in Stokes flow. The subject area and history will be introduced in this chapter. Following on from that, numerical methods for studying these systems will be discussed in section 1.3. We then present work on self-replicating lattices for linear flows in chapter 2. Chapter 3 contains the main results of the thesis. In a variety of two-dimensional linear flows, we present results on short-time rheology, steady-state rheology and the transients between the two. The suspension is considered to consist of hard spheres at various solids concentrations in a viscous fluid. In chapter 4 we study the effect of surface roughness. Finally in chapter 5 we summarise our work and consider future directions which may be followed. The appendix A, looks at the extension of a monolayer Stokesian dynamics to an infinite domain using Ewald summation and explains the difficulties encountered in two dimensions.

1.2 Background

1.2.1 Suspensions

Suspension flows are fluid flows in which particles are suspended within the fluid. The fluid can be in the most general sense; Newtonion or non Newtonian; the particle also be general; regular or irregular; homogeneous or inhomogeneous. The suspended particles may be individual particles or collections of particles in linked chains. Suspension problems may be encountered in many different forms and on different scales. Lava or pyroclastic flows in which the suspended particles are rocks, trees and other types of debris are at one end of the scale with drug delivery systems affected by Brownian motion at the other end of the scale. With an area of study this wide it is clear that there will also be a wide variety of industrial uses. The following are just a few examples.

- Integrated circuit boards

  The production of integrated circuit boards uses screen printing of a solder suspension to create the tracks of circuit. The geometry involved in the printing is a confined monolayer, to which our work of appendix A is applicable.

- Drug delivery

  The delivery of some drugs within biological systems occurs through dispersion of particles in, for instance, the bloodstream.

- Oil pumping

  Efficient oil pumping is of course an important problem for rigs all over the world. Particles suspended within the oil affect the fluid flow, hence understanding how the system behaves is important for oil companies.

- Filled materials

  The plastics industry increasingly uses solid filler particles in their products. The filler may provide extra strength (often through fibre-shaped

inclusions), colour (e.g. carbon black) or simply be cheaper than the plastic being used. These are suspension systems during processing, when the polymer matrix is molten but the fillers remain solid.

The study of suspensions frequently encompasses rheological behaviour. Even when the fluid in which the particles are suspended is Newtonian, the effect of the particles can add a non-Newtonian aspect to the Cauchy stress tensor. There has been much theoretical and experimental work done on this subject. Suspensions are a well studied area from both a theoretical and experimental standpoint. Experimental studies tend to concentrate on shear thinning and thickening of suspensions in Newtonian and non-Newtonian fluids. In this thesis we shall be concentrating on theoretical modelling, so we shall concentrate more on the history of the theoretical side of the subject, after a brief review of experimental work.

1.2.2 Experimental work on suspensions

Real systems

Arp and Mason [5] showed that in the real world it is inevitable that even smooth particles have some surface roughness, and (unlike the theoretical picture for ideally smooth particles) if two particles pass close enough to each other they may come into contact. Rampall's 1977 paper [49] is relevant to our two dimensional problem as they find that in a shear flow, particles whose closed orbits (relative to one another) are in the same plane of shear have an approach which is realistically close enough for interparticle contact to occur. Much experimental work focusses on shear thickening or shear thinning near the glass transition point. Experimental work also regularly considers suspensions of polymers and non Newtonian fluids such as corn starch [25] and gelatin [38]. These complex systems are very difficult to study theoretically, and we will not address them further in this thesis.

Idealised systems

As mentioned above the experimental work tends to concentrate on shear thickening or shear thinning near the glass transition point, however there does exist some experimental work on idealised systems. In an attempt to create some data for idealised systems some experiments have been done with glass spheres which are a good approximation to a hard smooth sphere.
Manley in 1954 [46] did some work on the particle interaction coefficient for particles in the same plane of shear. These idealised systems yielded an empirical equation in terms of concentration, building on previous work of Vand [57, 58].

Two dimensional idealised systems

There is not a huge amount of experimental monolayer work. What is available concentrates on shear flow and aggregate break up.
Vassileva [59] considers glass particles in a two dimensional shear flow. The monolayer is created by an air-water interface containing glass particles. Investigation of the shear rate for which the aggregates break up is undertaken and the rate at which this happens appears to be largely independent of particle size. More recently, the same group [60] carried out a similar study using a water–oil interface. They determined that there were two distinct mechanisms for aggregate break-up: erosion, in which single particles became separated from the bulk, and fragmentation, in which a large aggregate would break into several smaller ones. Fragmentation was found to occur predominantly for larger particles (radius over $100\,\mu$m) whereas erosion happened to aggregates of any size of particle.

1.2.3 Theoretical work on suspensions: History

Almost all the prior work on suspensions has considered particles suspended in a Newtonian fluid, and this is also the scenario for which most numerical

methods have been designed. This thesis is no exception: the suspending fluid in our case will be assumed to be Newtonian, but of course the particles will contribute to the total fluid stress. We are considering a system of identical solid smooth spherical particles suspended in an unbounded Newtonian fluid at low Reynolds number ($Re \ll 1$), such that the system may be considered a Stokes flow.

The area of study of suspended particles in a Stokes flow has been considered for many years and was until the 1970s mainly concerned with exact solutions. This early work considered either a very dilute system or a small number of particles immersed in a simple flow.

Einstein [22] considers a dilute suspension of solid spheres where each particle is considered isolated. If c represents the solids volume fraction or concentration (and for a dilute system, $c \ll 1$) the suspension is said to have viscosity $\mu(1 + \frac{5}{2}c)$ where μ is the viscosity of the fluid. In fact, using the minimum dissipation theorem for Stokes flow, it is possible to show that this formula gives us a lower bound for the stresses in any suspension at volume fraction c. Flows containing just two spherical particles have been thoroughly studied, from the isolated problems studied by O'Neill and coworkers (e.g. a sphere rotating close to a wall [14], two spheres translating or rotating very close together [48]) to the extensive study on the motion of two spheres by Jeffrey & Onishi [34].

However, the problem of exact solutions to suspension flows soon becomes very complicated for anything other than a very small number of particles or a dilute suspension. As the suspension concentration increases many body interactions become increasingly important and cannot be ignored. Computational methods start to become necessary at this point. In suspensions of even moderate concentration, lubrication interactions also become necessary and neglecting them misses key physical characteristics of the flow.

1.2.4 Survey of Numerical Methods

In the seventies several new numerical methods arose that allowed some inroads to be made in to the subject:

- The boundary integral equation method.
- The multipole method.
- The multipole collocation method.

More recently we have seen the development of Stokesian Dynamics, lattice-Boltzmann methods and Dissipative Particle Dynamics, amongst others. We will give a brief overview of these methods before returning in section 1.3 to a full description of Stokesian Dynamics, our method of choice.

Boundary integral equation method

The boundary integral equation method is a useful method for dealing with particles with complex geometries. The boundary integral equation method offers an advantage over the standard finite element or finite difference methods, because rather than solving a three dimensional PDE we are instead solving a two dimensional integral equation discretised over the particle surfaces. This is still however computationally expensive, and for a large system the expense is hard to overcome even with parallel computing. The boundary integral method's strength, its ability to deal with odd-shaped particles, becomes a weakness if the particles have some symmetry, as there is unneccessary computational expense in integrating over the surface of the particles.

Multipole method

The multipole method is a prerequisite of the multipole collocation method, as the name suggests. The method involves expanding the integral (equation (1.29) of section 1.3) used in the boundary integral method, and truncating the expansion at the desired accuracy. This method does offer a computa-

tional advantage for low order expansions. Lubrication interactions, however, are only included if all terms of the expansion are included. For low concentrations, lubrication interactions are unimportant but for higher concentrations they become important and this is the strongest limitation of the multipole method.

Multipole collocation method: Stokesian Dynamics

We shall instead be using the multipole collocation method, or rather the Stokesian Dynamics method derived from it.

Stokesian Dynamics (SD) [11] is a computational method specifically to model suspensions of spheres in low Reynolds number flows developed by Durlofsky and Brady [50]. The motivation behind its development was to create a method of modelling many-body suspensions that is computationally feasible but still contains the lubrication interactions necessary for accurate rheological behavior to be predicted. Stokesian Dynamics has become the standard for simulating the flow of idealised spherical hard-sphere colloids. We will give the full details of SD in section 1.3.

Lattice-Boltzmann methods

The main long-standing alternative to SD is that of the lattice-Boltzmann technique applied to particle suspensions developed by Ladd in [41] and [42] and developed further by Sangani [51]. The lattice-Boltzmann technique, as the name suggests, solves the Boltzmann equation, it does so by a statistical distribution of fluid particles within a fluid and extending this to a lattice, hence allowing the consideration of an infinite domain. As the lattice-Boltzmann method is not explicitly solving the Navier–Stokes equation, it is a computationally fast method. However, it does not contain the lubrication interactions as standard and hence fails to compute many of the key macroscopic behaviours of a suspension.

Dissipative Particle Dynamics

Another alternative method is that of Dissipative Particle Dynamics (DPD). Dissipative Particle Dynamics is a relatively new method which is based on stochastic simulation. DPD was developed to avoid the lattice artifacts of Lattice Gas Automata (cellular automaton), where isotropy and Galilean invariance are broken. Developed by Hoogerbrugge [33] it is a popular method for modelling macroscopic, non-Newtonian flow. DPD (like the lattice-Boltzmann method described above) fails to capture the lubrication interaction, and hence fails to compute many of the key macroscopic behaviours of a suspension.

Other alternatives

There are of course other alternatives, many of which are discussed in Brady's 1987 paper [21], but we shall review them briefly here. Ganatos [30] uses a collocation technique. For the use of a collocation technique, the problems need to have a high order of symmetry in order to leave a sufficiently small number of unknowns that these are practical to compute.

Another method suggested by Brady in [21] is to use the solution of the integral equation for Stokes flow by Young [67]. This method is similar in form to the boundary integral technique discussed above. Its strength is its ability to calculate with general particle shapes. The use of finite difference and finite element methods to solve the resulting discretised system could work well for a small finite domain, but there is no easy way to extend the method to an infinite domain; and since many body interactions in Stokes flow decay relatively slowly (at a rate $\sim 1/r$ in particle separation r), we do require a very large domain to gain accurate results.

A more in-depth review and summary of all the methods discussed here can be read in the review paper by Weinbaum [61].

All of these methods have their own strengths and weaknesses; the biggest weakness in many of them is that the lubrication forces are not explicitly

included and hence are either added on "by hand" for lattice-Boltzmann and DPD, or included approximately by increasing accuracy for methods such as those used by Ganatos [30]. This greater accuracy is achieved by means of more collocation points, hence increasing the number of unknowns and creating a more computationally expensive problem. The big advantage of Stokesian Dynamics is the explicit inclusion of the pairwise exact two body resistance functions calculated by Arp [5].

1.3 Stokesian Dynamics

1.3.1 Introduction

The method of Stokesian Dynamics was first proposed by Durlofsky, Brady and Bossis [21]. As described above, SD was developed to overcome many of the shortcomings of other methods.

The primary problem in creating an accurate model for suspensions in a low Reynolds number flow is the inclusion of lubrication forces while keeping the computational expense affordable. Just like any computational model there is a balancing act of speed *vs.* accuracy. The dominant hydrodynamic forces involved are the many body interactions and the lubrication forces. Lubrication forces become more important the higher the particle concentration / volume fraction becomes: this is because the increased number of particles within the given space results in a greater number of close interactions. Even at relatively low concentrations, failure to include lubrication interactions results in physically unrealistic models. Stokesian Dynamics uses the exact two-body interactions calculated by Kim [36]; Arp [5]; and Jeffrey [34] to include the lubrication interactions through the resistance matrix.

Hydrodynamic interactions in a many-body system are calculated by using the method of reflections. Two-body interactions are considered to be the most important as within the mobility matrix three-body interactions do not arise

until $O(1/r^4)$ with interparticle separation r, and four-body interactions until $O(1/r^7)$ (Kynch [40]). In contrast three-body interactions are said to arise at $O(1/r^7)$ within the resistance matrix. Bossis and Brady [21] however continue to neglect three-body and higher interactions in their formulation as it is felt that at high concentrations (where many-body effects become important) these interactions would be dominated by lubrication forces.

The SD model calculates an approximation for the many-body far field interactions by truncation of an exact integral representation. The details of how this is implemented are discussed in section 1.3.11. The lubrication forces are then added later in the formulation via exact forms.

Stokesian Dynamics is well established for same sized particles, however, Jeffrey [34] has extended the two-sphere mobility relations to allow for different sized particles.

In the remainder of this section, we will show the derivation of Stokesian Dynamics from the basics of Stokes flow, culminating in its full implementation and a discussion of the method of Ewald summation for simulating infinite systems.

1.3.2 Quasi-static Property of the Stokes equations

We are considering low-Reynolds number flow of an incompressible Newtonian fluid, that is inertial forces are neglected. The governing equations for this system are:

$$\nabla \cdot \mathbf{u} = 0 \qquad \nabla p = \mu \nabla^2 \mathbf{u} \tag{1.1}$$

in which $\mathbf{u}$ is the fluid velocity, p its pressure, and μ is the viscosity of the fluid. These are known as the Stokes equations.

An important property of these equations is that they are quasi-static, meaning that there is no explicit time-dependence in the equations. The flow is hence determined instantaneously by the boundary conditions (in our case on the particles). In the case of a suspension the boundary conditions consist of

the particle configuration, and the external forces and torques acting on them. The SD method exploits this property, and depends only on the configuration of the particles at any moment in time and not their velocities. The general problem it considers is a system of N particles suspended in a Newtonian fluid with a background flow $\mathbf{u}^{\infty}(\mathbf{x})$ and it calculates the translational and angular velocity of each particle.

1.3.3 Derivation Overview

The Stokes equations are linear, they are amenable to solution by Green's function methods. Essentially, the concept is to represent all the boundary conditions (in our case, external forces and torques on the surface of various solid particles, plus the constraints that each particle must move as a rigid body) through a distribution of point forces on the boundary of the fluid. For a suspension of solid spheres, the point forces will be distributed over the surfaces of the particles.

In the next few sections we will construct a multipole expansion based on the Green's function solution to the Stokes equations. In section 1.3.4 we begin by deriving the Green's function itself: that is, the response of a viscous fluid to a point force. In section 1.3.5, we formulate the Green's function form of the solution for a system of many spherical particles, take an expansion of the solution, valid for well-spaced particles, and show how this expansion may logically be truncated. Then in section 1.3.6, as an illustration, we show how this truncated expansion provides the correct solution for the fluid flow around a solid sphere moving under a prescribed force through a quiescent fluid (a problem which we had already solved in section 1.3.4). An overview of Stokesian Dynamics derivation can be seen in figure 1.1.

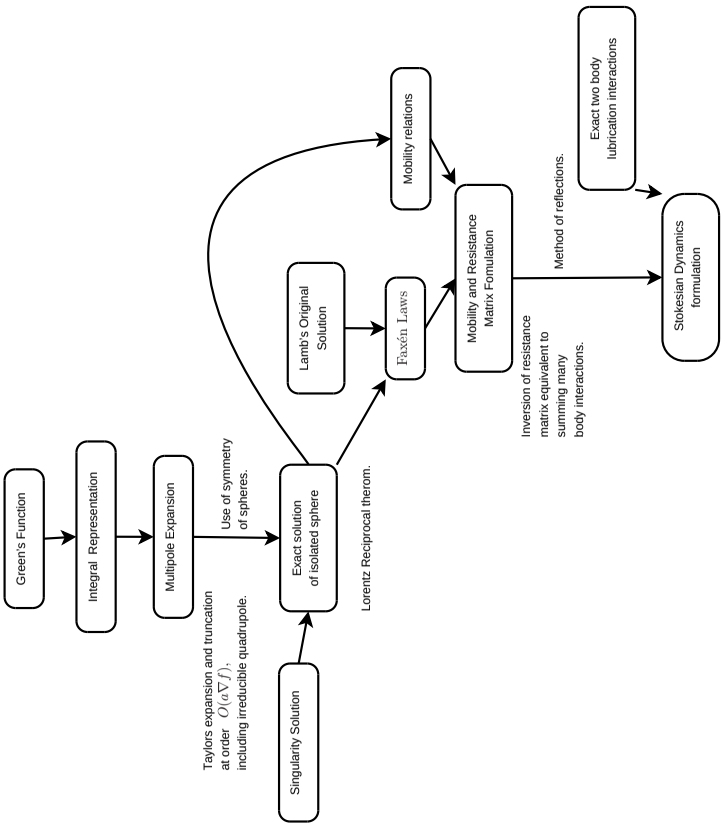

Figure 1.1: Map of Stokesian Dynamics derivation and relationship to other solutions of suspension dynamics.

1.3.4 Green's Function Derivation

To model a flow with many spherical particles we must first consider a single particle's effect on a fluid. We derive the Green's function for Stokes flow, that is, the response of the Stokes equations to a point force, which we will calculate by looking first at a spherical particle with an external force applied to it, and then taking the radius of the particle to zero.

We consider a sphere of radius a moving with speed U in the z direction, shown in figure (1.2).

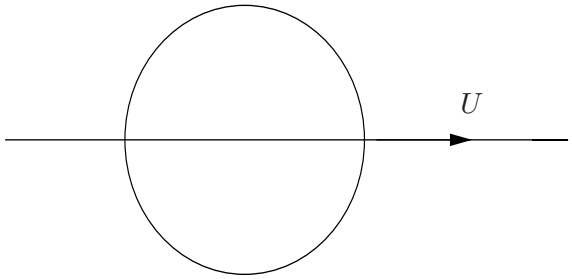

Figure 1.2: Translating Sphere

We expect the solution for the velocity and pressure everywhere in the fluid to be axisymmetric about the z-axis, and we use the standard spherical polar coordinates (r, θ, ϕ).

We shall use the Stokes stream function $\psi(r, \theta)$ such that

$$\mathbf{u} = \nabla \wedge \left(\frac{\psi \, \mathbf{e}_\phi}{r \sin \theta} \right), \tag{1.2}$$

with $\mathbf{e}_\phi$ denoting the unit vector in the ϕ direction. If we take the curl of the Stokes equation we have

$$\nabla^2 (\nabla \wedge \mathbf{u}) = 0, \tag{1.3}$$

so we define $\omega = \nabla \wedge \mathbf{u}$ and, taking the curl of $\mathbf{u}$, obtain

$$\omega = -\frac{1}{r \, \sin \theta} D^2 \psi \, \mathbf{e}_\phi, \tag{1.4}$$

where $D^2\psi$ is the Stokes operator:

$$D^2 \psi = \frac{\partial^2 \psi}{\partial r^2} + \frac{\sin \theta}{r^2} \frac{\partial}{\partial \theta} \left(\frac{1}{\sin \, \theta} \frac{\partial \psi}{\partial \theta} \right). \tag{1.5}$$

Since $\nabla^2\omega = 0$, we may say

$$D^2\psi = -\Omega, \tag{1.6}$$

$$D^2\Omega = 0, \tag{1.7}$$

in $r \geq a$, for some unknown function $\Omega(r, \theta)$. The boundary conditions we wish to apply are those of no slip at the surface of our sphere:

$$\mathbf{u} = (U\,\cos\theta, -U\,\sin\theta, 0) \qquad \text{on } r = a \tag{1.8}$$

and decay of the velocity in the far field, $\mathbf{u} \to \mathbf{0}$ as $r \to \infty$. The no-slip condition means that

$$\frac{1}{a^2\sin\theta}\frac{\partial\psi}{\partial\theta} = U\,\cos\theta, \qquad -\frac{1}{a\,\sin\theta}\frac{\partial\psi}{\partial r} = -U\,\sin\theta \quad \text{on } r = a. \tag{1.9}$$

Integrating the first equation results in

$$\psi = \frac{1}{2}U\,a^2\,\sin^2\theta + C, \qquad \frac{\partial\psi}{\partial r} = U\,a\sin^2\theta \qquad \text{on } r = a. \tag{1.10}$$

The far-field boundary condition requires $\psi = o(r^2)$. The form of these boundary conditions suggests that the constant C will lead only to an additional constant in ψ, which may be neglected as the velocity depends only on derivatives of ψ. Thus we set $c = 0$ and with our full set of boundary conditions we can start to seek a full solution of the form

$$\psi = f(r)\sin^2\theta. \tag{1.11}$$

Substituting this into $D^2\psi = -\Omega$ gives

$$D^2\psi = f''\sin^2\theta - \frac{2}{r^2}f\sin^2\theta \equiv F(r)\sin^2\theta = -\Omega. \tag{1.12}$$

We recall that

$$D^2\Omega = 0, \tag{1.13}$$

hence

$$F'' - \frac{2\,F}{r^2} = 0, \tag{1.14}$$

yielding

$$F = A\,r^2 + \frac{B}{r}, \tag{1.15}$$

and furthermore

$$f(r) = C\,r^2 + \frac{D}{r} + A'\,r^4 + B'\,r. \tag{1.16}$$

Using our boundary conditions this leads us to our final result of

$$\psi(r,\theta) = a^2\,U\,\sin^2\theta\left(\frac{3\,r}{4\,a} - \frac{a}{4\,r}\right). \tag{1.17}$$

The next step is to find the pressure, which will then allow us to find the drag and hence the relationship between velocity and force. Calculating $\mathbf{u}$ gives

$$\mathbf{u} = U\left(2\cos\theta\left[\frac{3a}{4r} - \frac{a^3}{4r^3}\right],\ -\sin\theta\left[\frac{3a}{4r} + \frac{a^3}{4r^3}\right],\ 0\right), \tag{1.18}$$

and after substituting into the Stokes equations and integrating in r,

$$p - p_\infty = -\frac{3}{2}\frac{\mu\,U\,a}{r^2}\cos\theta \tag{1.19}$$

where p_∞ is the background (far-field) pressure. We can now calculate the drag from

$$D_i = \int_S \sigma_{ij}\,n_j dS, \tag{1.20}$$

where $\sigma_{ij} = -p\,\delta_{ij} + 2\,\mu\,e_{ij}$ and $e_{ij} = \frac{1}{2}(\nabla_i u_j + \nabla_j u_i)$. This results in the well known relationship

$$\mathbf{D} = -6\pi a\mu U\mathbf{e}_z. \tag{1.21}$$

If we use this relationship to eliminate U from $\mathbf{u}$, and denote the magnitude of the drag force as $|\mathbf{D}| = D$, we can arrive at

$$u_r = -\frac{D\,\cos\theta}{3\,\pi\mu}\left[\frac{3}{4\,r} - \frac{a^2}{4\,r^3}\right], \tag{1.22}$$

$$u_\theta = \frac{D\,\sin\theta}{6\,\pi\mu}\left[\frac{3}{4\,r} + \frac{a^2}{4\,r^3}\right]. \tag{1.23}$$

Now consider the case $r \gg a$: either looking at points far from the particle, or decreasing the particle radius a. In the limit $a \to 0$ the particle (with the drag force acting on it) looks like a point force, and the velocity field becomes

$$\mathbf{u} = \frac{D}{3\,\pi\mu}\left(-\frac{3\,\cos\theta}{4\,r}, \frac{3\,\sin\theta}{8\,r}, 0\right). \tag{1.24}$$

We now change to Cartesian coordinates for convenience. In order to make our particle move as described above, we need to apply an external force equal and opposite to $\mathbf{D}$: we will denote this point force as $\mathbf{f}$. After the change of coordinates we are left with

$$u_i = \frac{1}{8\,\pi\mu}\left(\frac{\delta_{ij}}{r} + \frac{x_i x_j}{r^3}\right) f_j, \tag{1.25}$$

which we shall rewrite as

$$8\,\pi\mu u_i = J_{ij} f_j, \tag{1.26}$$

with

$$J_{ij}(\mathbf{r}) = \frac{\delta_{ij}}{r} + \frac{r_i r_j}{r^3}, \tag{1.27}$$

which is known as the stokeslet or Oseen tensor. This can be rewritten as

$$J_{ij} = \left(\delta_{ij}\nabla^2 - \nabla_i \nabla_j\right) r. \tag{1.28}$$

Equation (1.25) gives the velocity field induced by a point force acting on the fluid.

1.3.5 The Multipole Expansion

It has been shown that we can represent any particle by a series of point forces, and the fluid's response to each is given by equation (1.25). The linearity of the Stokes equations allows us to superimpose these flows.

Now we will apply the Green's function representation to the system we are actually interested in. We want to investigate fluid flow past a collection of spheres. To do so, we consider a boundary which is, in some sense, a more general shape: N identical spherical particles within a three-dimensional infinite domain, with in addition a linear background flow $\mathbf{u}^\infty$. Equation (1.29) gives the velocity field anywhere in the fluid: it is simply derived from equation (1.25) integrated over every particle surface:

$$u_i(\mathbf{x}) = u_i^\infty(\mathbf{x}) - \frac{1}{8\pi\mu}\sum_{\alpha=1}^{N}\int_{S_\alpha} J_{ij}(\mathbf{x}-\mathbf{y}) f_j(\mathbf{y}) \mathrm{d}S_y. \tag{1.29}$$

Here S_α is the surface of the particle α, f_j represents the force distribution on the surface of each particle, and u_i^∞ is the velocity of the fluid without particles. We shall be considering only linear background flows of the form $\mathbf{u}^\infty = \mathbf{G} \cdot \mathbf{x}$. J_{ij} is, of course, the Green's function known as the stokeslet or Oseen tensor, derived above in section 1.3.4:

$$J_{ij}(\mathbf{r}) = \frac{\delta_{ij}}{r} + \frac{r_i r_j}{r^3}, \tag{1.30}$$

with $\mathbf{r} = \mathbf{x} - \mathbf{y}$ and $r = |\mathbf{r}|$. The force at any surface point is expressed by

$$f_j(\mathbf{y}) = \sigma_{jk}(\mathbf{y}) n_k. \tag{1.31}$$

where n_k is the unit vector normal to the sphere's surface. Note the change of sign in equation (1.29) relative to equation (1.25). We are now using f_j to represent the force acting on the **particle** from the fluid: thus the force acting on the fluid is $-f_j$.

This integral formulation can of course be numerically solved on its own but this would be computationally prohibitive. The surface of each particle could be divided into M elements and the linear equations could be solved over these elements. In a system with N particles the number of unknowns is $(3M + 6)N$; three force components for each element, and translational and angular velocities for each particle. In two dimensions there are $(2M + 3)N$ unknowns. According to Brady in [21], $M = 12$ is the minimum number of elements in three dimensions, and $M = 6$ in two dimensions. This is due to the maximum possible number of nearest neighbours, and can be seen easily in two dimensions in figure 1.3.

To simplify the integral equation (1.29) and the computations that follow from it, we expand the Green's function J_{ij} as a Taylor series around $\mathbf{x}_\alpha$. This method is referred to as the multipole expansion, and will result in an expansion in moments of the force distribution. We begin by introducing a notation for these moments. The n^{th} moment is given by

$$Q^n_{i\ldots j} = -\int_{S_\alpha} \prod_{i\ldots}^{n} (y_i - x_i^\alpha) f_j(\mathbf{y}) \mathrm{d}S_y. \tag{1.32}$$

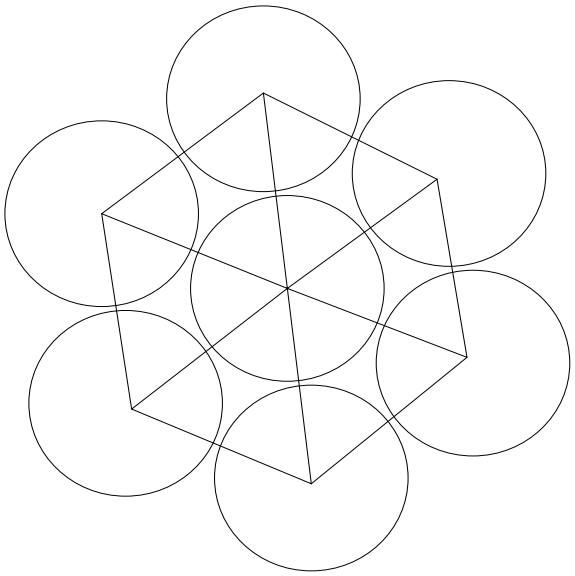

Figure 1.3: Nearest Neighbours in 2D

The n^{th} moment is a tensor of order $n+1$, and we will only be interested in the first few. For example, the second moment is a third order tensor given by

$$Q^2_{klj} = -\int_{S_\alpha} (y_k - x^\alpha_k)(y_l - x^\alpha_l) f_j(\mathbf{y}) \mathrm{d}S_y. \tag{1.33}$$

The zeroth moment, a tensor of order one (i.e. a vector), is the total force density

$$Q^0_i = -F^\alpha_i = -\int_{S_\alpha} f_i(\mathbf{y}) \mathrm{d}S_y, \tag{1.34}$$

the hydrodynamic force exerted by the fluid on particle α, that is, (-1) time the force exerted by the particle on the fluid. The antisymmetric part of the first moment is the torque exerted by the particle on the fluid:

$$\epsilon_{ijk} Q^1_{jk} = L^\alpha_i = -\int_{S_\alpha} \epsilon_{ijk}(y_j - x^\alpha_j) f_k(\mathbf{y}) \mathrm{d}S_y, \tag{1.35}$$

and its symmetric, deviatoric part is the stresslet:

$$\begin{aligned} &\frac{1}{2}(Q^1_{ij} + Q^1_{ji} - \frac{2}{3}\delta_{ij} Q^1_{kk}) = S^\alpha_{ij} = \\ &\quad -\frac{1}{2}\int_{S_\alpha} (y_i - x^\alpha_i) f_j(\mathbf{y}) + (y_j - x^\alpha_j) f_i(\mathbf{y}) - \frac{2}{3}\delta_{ij}(y_k - x^\alpha_k) f_k(\mathbf{y}) \mathrm{d}S_y. \end{aligned} \tag{1.36}$$

The trace of the first moment is a pressure contribution:

$$Q^1_{ii} = 3P^\alpha = -\int_{S_\alpha} (y_i - x_i^\alpha) f_i(\mathbf{y}) \mathrm{d}S_y, \tag{1.37}$$

so that

$$Q^1_{ij} = -\int_{S_\alpha} (y_i - x_i^\alpha) f_j(\mathbf{y}) \mathrm{d}S_y = P^\alpha \delta_{ij} + S^\alpha_{ij} + \frac{1}{2}\epsilon_{ijk} L^\alpha_k. \tag{1.38}$$

We define the stresslet to have no trace, and will not calculate the quantity P^α; the trace results in a particle contribution to the pressure which we shall neglect as it has no effect on the flow of a homogeneous suspension, although it would have importance if there were a concentration gradient. This is a common convention which we shall follow.

The best way to demonstrate the force distribution corresponding to the force, torque and stresslet is through figure 1.4. The arrows represent how the point

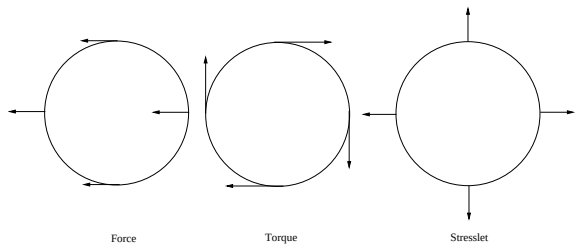

Figure 1.4: Force distributions corresponding to force, torque and stresslet on a sphere

forces are acting on the particle. The hydrodynamic force and torque will be zero for a particle with no external effects acting on it; the stresslet, on the other hand, results from particle rigidity and is likely to be non-zero in most flows.

Explicit expansion of the Oseen tensor

Equation (1.29) contains the quantity $J_{ij}(\mathbf{x} - \mathbf{y})$ in an integral (with respect to $\mathbf{y}$) over the surface of a sphere whose centre is instantaneously at $\mathbf{x}^\alpha$. We

expand this in a Taylor series about the point $\mathbf{y} = \mathbf{x}^\alpha$:

$$\begin{aligned} J_{ij}(\mathbf{x}-\mathbf{y}) &= J_{ij}(\mathbf{x}-\mathbf{x}^\alpha+\mathbf{x}^\alpha-\mathbf{y}) \\ &= J_{ij}(\mathbf{x}-\mathbf{x}^\alpha) + (\mathbf{x}^\alpha-\mathbf{y})\cdot\nabla[J_{ij}]\mid_{(\mathbf{x}-\mathbf{x}^\alpha)} \\ &+ \frac{1}{2}(\mathbf{x}^\alpha-\mathbf{y})(\mathbf{x}^\alpha-\mathbf{y}):\nabla\nabla[J_{ij}]\mid_{(\mathbf{x}-\mathbf{x}_\alpha)} \\ &+ \frac{1}{6}(\mathbf{x}^\alpha-\mathbf{y})(\mathbf{x}^\alpha-\mathbf{y})(\mathbf{x}^\alpha-\mathbf{y})\vdots\nabla\nabla\nabla[J_{ij}]\mid_{(\mathbf{x}-\mathbf{x}_\alpha)}+\cdots \end{aligned} \tag{1.39}$$

Substituting this into the integral equation (1.29) and using the moments expansion introduced above,

$$\begin{aligned} u_i(\mathbf{x}) = u_i^\infty(\mathbf{x}) - \frac{1}{8\pi\mu}\sum_\alpha \big[& J_{ij}(\mathbf{x}-\mathbf{x}^\alpha)Q_j^0 \\ & + \nabla_k J_{ij}(\mathbf{x}-\mathbf{x}^\alpha)Q_{kj}^1 \\ & + \frac{1}{2}\nabla_k\nabla_l J_{ij}(\mathbf{x}-\mathbf{x}_\alpha)Q_{klj}^2 \\ & + \frac{1}{6}\nabla_k\nabla_l\nabla_m J_{ij}(\mathbf{x}-\mathbf{x}_\alpha)Q_{klmj}^3 \\ & + \cdots\big] \end{aligned} \tag{1.40}$$

in which $f_j(\mathbf{r})$ is the force distribution on the surface of the sphere.

The moment Q_j^0 is order $O(f)$; Q_{kj}^1 is of order $O(a\nabla f)$ where a is the radius of the particle. Q_{klj}^2 is order $O(a^2\nabla^2 f)$ when $k \neq l$ and $O(f)$ when $k = l$, and Q_{klmj}^3 is order $O(a^3\nabla^3 f)$ when all of k, l, m are different and $O(a^2\nabla^2 f)$ when any two of them match. In fact, we can write

$$Q_{klj}^2 = \frac{1}{3}a^2\delta_{kl}Q_j^0 + O(a^2\nabla^2 f), \tag{1.41}$$

$$Q_{klmj}^3 = \frac{1}{10}a^2\left[\delta_{kl}Q_{mj}^1 + \delta_{km}Q_{lj}^1 + \delta_{lm}Q_{kj}^1\right] + O(a^3\nabla^3 f). \tag{1.42}$$

We truncate our expansion at order $O(a\nabla f)$, the truncated expansion becomes:

$$\begin{aligned} u_i(\mathbf{x}) = u_i^\infty(\mathbf{x}) - \frac{1}{8\pi\mu}\sum_\alpha \big[& J_{ij}(\mathbf{x}-\mathbf{x}^\alpha)Q_j^0 \\ & + \nabla_k J_{ij}(\mathbf{x}-\mathbf{x}^\alpha)Q_{kj}^1 \\ & + \frac{1}{6}a^2\nabla^2 J_{ij}(\mathbf{x}-\mathbf{x}_\alpha)Q_j^0 \\ & + \frac{1}{10}a^2\nabla^2\left[\nabla_m J_{ij}Q_{mj}^1 + \nabla_l J_{ij}Q_{lj}^1 + \nabla_k J_{ij}Q_{kj}^1\right]\big] \end{aligned} \tag{1.43}$$

Using the forms of the moment given in equations (1.34), (1.35) and (1.36) we may re-write (1.43):

$$\begin{aligned} u_i = u_i^{\infty}(\mathbf{x}) - \frac{1}{8\pi\mu}\sum_{\alpha}\Bigg[&- \left\{1 + \frac{1}{6}a^2\nabla^2\right\} J_{ij}(\mathbf{x}-\mathbf{x}^{\alpha})F_j^{\alpha} \\ &+ \frac{1}{2}\epsilon_{jkl}\nabla_k J_{il}(\mathbf{x}-\mathbf{x}^{\alpha})L_j^{\alpha} + \left\{1 + \frac{1}{10}a^2\nabla^2\right\}\nabla_k J_{ij}(\mathbf{x}-\mathbf{x}_{\alpha})S_{jk}^{\alpha}\Bigg]. \end{aligned} \tag{1.44}$$

in which we have used the facts that $\nabla_j J_{ij} = 0$, $\nabla^2(\nabla_k J_{ij} - \nabla_j J_{ik}) = 0$ to discard terms. The velocity is expressed linearly in terms of the forces, torques and stresslets. This procedure will allow us to construct matrices relating flow variables to force variables in section 1.3.9.

Equation (1.44) allows us to find the disturbance velocity caused by all of the particles. The forces torques and stresslets felt by each sphere all depend on every other sphere. The problem is still not solved, however if $n = 1$ equation (1.44) will give the disturbance velocity created by a single particle, as we will illustrate in the next section for one simple case.

1.3.6 Use of the Green's function

We now consider again the situation in which a single sphere of radius a is moving under the action of a force $\mathbf{F}$ in an otherwise quiescent viscous fluid of viscosity μ. We locate the particle instantaneously at the origin. There is no external torque on the sphere, and (for this simple flow) no stresslet. Then the truncated expansion of equation (1.44) gives

$$u_i'(\mathbf{x}) = \frac{1}{8\pi\,\mu}\left(1 + \frac{a^2}{6}\nabla^2\right) J_{ij}(\mathbf{x}-\mathbf{x}^{\alpha})F_j^{\alpha}. \tag{1.45}$$

Let us consider the ∇^2 term in (1.45).

$$\begin{aligned} \nabla_k J_{ij} &= \frac{\partial}{\partial x_k}\left(\frac{\delta_{ij}}{r} + \frac{x_i x_j}{r^3}\right) \\ &= \frac{1}{r^3}\left[\delta_{ik}x_j + \delta_{jk}x_i - \delta_{ij}x_k\right] - \frac{3x_i x_j x_k}{r^5}, \end{aligned} \tag{1.46}$$

leading to

$$\nabla^2 J_{ij} = \frac{2\delta_{ij}}{r^3} - \frac{6x_i x_j}{r^5}, \tag{1.47}$$

and hence

$$\left(1 + \frac{a^2}{6}\nabla^2\right) J_{ij} = \delta_{ij}\left(\frac{1}{r} + \frac{a^2}{3r^3}\right) + x_i x_j \left(\frac{1}{r^3} - \frac{a^2}{r^5}\right). \tag{1.48}$$

Substituting this into (1.45), along with the force $\mathbf{F}^\alpha = -D\mathbf{e}_z$ gives us

$$\begin{aligned} u_i'(\mathbf{x}) &= \frac{-D}{8\pi\,\mu}\left[\delta_{ij}\left(\frac{1}{r} + \frac{a^2}{3r^3}\right) + x_i x_j\left(\frac{1}{r^3} - \frac{a^2}{r^5}\right)\right]\delta_{j3} \\ &= -\frac{D}{8\pi\,\mu}\left[\delta_{i3}\left(\frac{1}{r} + \frac{a^2}{3r^3}\right) + x_i z\left(\frac{1}{r^3} - \frac{a^2}{r^5}\right)\right]. \end{aligned} \tag{1.49}$$

Let us compare this with the two equations (1.22–1.23) (which are in spherical polar coordinates) and calculate u_x, u_y and u_z from them using

$$\mathbf{u}' = u_r\mathbf{e}_r + u_\theta\mathbf{e}_\theta. \tag{1.50}$$

We obtain

$$\begin{aligned} u_z &= u_r\,\cos\theta - u_\theta \sin\theta \\ &= \frac{D}{6\pi\mu}\left\{\frac{-3}{4\,r}\left(1 + \frac{z^2}{r^2}\right) + \frac{a^2}{4\,r^3}\left(-1 + \frac{3\,z^2}{r^2}\right)\right\}, \end{aligned} \tag{1.51}$$

and

$$\begin{aligned} u_x &= (u_r\,\sin\theta + u_\theta\,\cos\theta)\cos\phi \\ &= \frac{D}{6\pi\mu}\left\{\frac{-3}{4r}\frac{xz}{r^2} + \frac{a^2}{4r^3}\frac{3xz}{r^2}\right\}, \end{aligned} \tag{1.52}$$

with u_y the same as u_x (but with each instance of x replaced with y) because of the axisymmetry. Finally after some rearranging

$$u_x = \frac{D}{6\pi\mu}xz\left[\frac{-3}{4r^3} + \frac{3a^2}{4r^5}\right], \tag{1.53a}$$

$$u_y = \frac{D}{6\pi\mu}yz\left[\frac{-3}{4r^3} + \frac{3a^2}{4r^5}\right], \tag{1.53b}$$

$$u_z = \frac{D}{6\pi\mu}\left[z^2\left(\frac{-3}{4r^3} + \frac{3a^2}{4\,r^5}\right) - \frac{3}{4r} - \frac{a^2}{4r^3}\right], \tag{1.53c}$$

which we can write as

$$u_i = \frac{D}{6\pi\mu}\left\{zx_i\left(-\frac{3}{4r^3}+\frac{3a^2}{4r^5}\right)+\delta_{i3}\left(-\frac{3}{4r}-\frac{a^2}{4r^3}\right)\right\}. \tag{1.54}$$

We can see (1.49) is equivalent to (1.54), this is just an example of an exact solution and its equivalence to the well known solution shown in (1.45). Similar expressions can be found for spheres immersed in different linear flows. These simple expressions in terms of the Oseen tensor are the reason why we will consider our particles to be spherical due to the simplifications which it affords us.

1.3.7 Singularity Solution

We have expanded the integral representation for Stokes flow, equation (1.29), using moments of the Green's function J_{ij} about each particle centre $\mathbf{x}_\alpha$.
However, to completely describe the flow field generated by a particle and all inter-particle interactions, all moments of the expansion would be necessary. If we were only considering the far field, we could truncate the expansion early as only the first few terms would be important. For the near field however, all terms are of approximately the same order and it becomes a lot harder to justify truncating the series.
Equally, even for an isolated particle, if the particle is of arbitrary shape then all moment terms can in principle contribute to the flow field. For an isolated sphere, the high degree of symmetry means the expansion terminates after the terms given in equation (1.43): thus, neglecting interparticle interactions, equation (1.44) is exact for a spherical particle.
The terms we have kept are the force (the zeroth moment), the torque and stresslet (the first moment or dipole term) and the dominant parts of the the third and fourth moment, which are known as the irreducible tripole and irreducible quadrupole respectively. The first of these reduces to another contribution involving the force, and the quadrupole term to another contribution using the stresslet.

A relationship of similar form to equation (1.44) appears in the Fáxen relations which we will see later in section 1.3.8. We will then use these relations to formulate mobility and resistance matrices in section 1.3.9. These relations all have a strong analogy with electrostatics (indeed a one-to-one correspondence), which is because the biharmonic equation arises in both fields. We shall use the Faxén Laws to introduce the mobility matrix, and later introduce the lubrication interactions via the resistance matrix.

1.3.8 Faxén Laws

The multipole expansion gives us a method for finding the disturbance flow caused by a set of spheres given the moments of the force distribution on each. Our truncation gives the disturbance flow field from the force, torque and stresslet on each sphere: but how do we find these quantities? This is where the Faxén Laws are used.

The Faxén laws are given in equation (1.55) for well-separated spheres (taken from Batchelor and Green [6]):

$$U_i^\alpha - u_i^\infty(\mathbf{x}^\alpha) = \frac{F_i^\alpha}{6\pi\mu a} + (1 + \frac{1}{6}a^2\nabla^2)u_i'(\mathbf{x}^\alpha), \tag{1.55a}$$

$$\Omega_i^\alpha - \Omega_i^\infty = \frac{L_i^\alpha}{8\pi\mu a^3} + \frac{1}{2}\varepsilon_{ijk}\nabla_j u_k'(\mathbf{x}^\alpha), \tag{1.55b}$$

$$-E_{ij}^\infty = \frac{S_{ij}^\alpha}{20\pi\mu a^3/3} + \left(1 + \frac{a^2}{10}\nabla^2\right) e_{ij}'(\mathbf{x}^\alpha), \tag{1.55c}$$

with u_i' being the induced velocity field from other particles (i.e. everything that is not u_i^∞ or the particle velocity U_i^α), U_i^α is the velocity of particle α, Ω_i^α is the rotational velocity of particle α. F_i^α is the external force imposed on particle α, L_i^α the external torque and S_{ij}^α the stresslet. The perturbation rate-of-strain tensor is

$$e_{ij} = \frac{1}{2}(\nabla_j u_i' + \nabla_i u_j'). \tag{1.56}$$

E_{ij}^∞ is the rate of strain tensor corresponding to the background flow u_i^∞, and Ω_i^∞ is its angular velocity.

The Faxén relations were derived from Lamb's general solution however this is not a pleasant task best left as historical route. Here we derive the force / translational velocity relationship 1.55a as an example.
The occurrence of the $(1 + \frac{a^2}{6}\nabla^2)$ should ring bells from the discussion in section 1.3.5; this is in fact a direct consequence of the Lorentz reciprocal theorem (1.57.)

$$\int_S \mathbf{v}_1.(\sigma_2.\mathbf{n})\mathrm{d}S - \int_V \mathbf{v}_1.(\nabla.\sigma_2)\mathrm{d}V = \int_S \mathbf{v}_2.(\sigma_1.\mathbf{n})\mathrm{d}S - \int_V \mathbf{v}_2.(\nabla.\sigma_1)\mathrm{d}V \quad (1.57)$$

where V is a fluid volume with bounding surface S, and $\mathbf{v}_{1,2}$ are two solutions to the Stokes equations valid throughout V. $\sigma_{1,2}$ are the stresses corresponding to the flows $\mathbf{v}_{1,2}$:

$$\sigma = -p\mathbf{I} + \mu(\nabla\mathbf{v} + \nabla\mathbf{v}^T). \quad (1.58)$$

In our use of this theorem we will take V to be the fluid exterior to a spherical particle of radius a having surface S_p, bounded by a large sphere S_∞. We will choose flows such that all contributions $\mathbf{v}_{1,2}$ and $\sigma_{1,2}$ decay away from the particle such that any contributions from the surface integral on the large sphere vanish as this large sphere tends to infinity. The result of this is that we only consider the contributions from the surface S_p, the surface of the particle. Now equation (1.57) can be rewritten as

$$\int_{S_p} \mathbf{v}_1.(\sigma_2.\mathbf{n})\mathrm{d}S - \int_V \mathbf{v}_1.(\nabla.\sigma_2)\mathrm{d}V = \int_{S_p} \mathbf{v}_2.(\sigma_1.\mathbf{n})\mathrm{d}S - \int_V \mathbf{v}_2.(\nabla.\sigma_1)\mathrm{d}V. \quad (1.59)$$

Now we fix our two solutions to the Stokes equations:

- $\mathbf{v}_1$ is the velocity field generated by a particle translating with velocity $\mathbf{U}$ in a quiescent fluid. This requires an external force $6\pi\mu a\mathbf{U}$ to be imposed on the sphere.

- $\mathbf{v}_2$ is the velocity field generated by a point force $\mathbf{F}$ outside the particle

at a point $\mathbf{y}$, but with the particle held stationary by a force $-\mathbf{F}_2$. This means that the hydrodynamic force acting on the particle is $\mathbf{F}_2$.

The stresses we need for the reciprocal theorem are

$$\begin{aligned} \nabla \cdot \sigma_1 &= 0 \\ \nabla \cdot \sigma_2 &= \mathbf{F}\delta(\mathbf{x}-\mathbf{y}) \end{aligned} \tag{1.60}$$

within the volume V; we also know that $\mathbf{v}_1 = \mathbf{U}$ and $\mathbf{v}_2 = 0$ on the particle surface S_p. The reciprocal theorem becomes

$$\begin{aligned} \int_{S_p} \mathbf{U}.\sigma_2.\mathbf{n}dS - \int_V v_1.\mathbf{F}\delta(\mathbf{x}-\mathbf{y})d\mathbf{V} &= 0 \\ \mathbf{U}.\mathbf{F}_2 - \mathbf{v}_1(\mathbf{y}).\mathbf{F} &= 0. \end{aligned} \tag{1.61}$$

We know, from the singularity solution for a sphere, that

$$(\mathbf{v}_1(y))_j = 6\pi\mu a U_i \left(1 + \frac{a^2}{6}\nabla^2\right) J_{ji}(\mathbf{y}-\mathbf{x}_\alpha)/8\pi\mu \tag{1.62}$$

which allows us to rewrite equation (1.61) as

$$U_i(F_2)_i - \left(\frac{3}{4}\right) a U_i \left(1 + \frac{a^2}{6}\nabla^2\right) J_{ji}(\mathbf{y}-\mathbf{x}_\alpha)F_j = 0. \tag{1.63}$$

Now this relation must be true for all possible velocity vectors $\mathbf{U}$, so we must have

$$(F_2)_i = \left(\frac{3}{4}\right) a(1 + \frac{a^2}{6}\nabla^2)J_{ji}(\mathbf{y}-\mathbf{x}_\alpha)F_j = \left(\frac{3}{4}\right) a \left(1 + \frac{a^2}{6}\nabla^2\right) J_{ij}\left(\mathbf{x}_\alpha - \mathbf{y}\right) F_j \tag{1.64}$$

using the symmetries of the Oseen tensor. This (or rather (-1) times it) gives us the force required to hold the particle fixed at $\mathbf{x}_\alpha$ in the presence of a point force $\mathbf{F}$ located at position $\mathbf{y}$ in a quiescent fluid.

Now we note that in the absence of the particle, the velocity field at a point ξ due to that point force would have been (from the Green's function solution)

$$v_i'(\xi) = J_{ij}(\xi - \mathbf{y})F_j/8\pi\mu \tag{1.65}$$

so in the presence of a velocity field $\mathbf{v}'(\xi)$ caused by a point force, the force required on our particle to hold it fixed would be

$$-(F_2)_i = -6\pi\mu a(1 + a^2/6\nabla^2)v_i'(\mathbf{x}_\alpha). \tag{1.66}$$

The linearity of Stokes flow then allows us to deduce the same result for any flow field $\mathbf{v}'$ created by a collection of point forces: in particular, for the flow field $\mathbf{u}'$ caused by the point forces on the surfaces of all the other particles in the ensemble. Thus, in the absence of any background flow, we have shown that if the external force acting on our particle is

$$F_i = -6\pi\mu a \left(1 + \frac{a^2}{6}\nabla^2\right) u_i'(\mathbf{x}_\alpha) \tag{1.67}$$

then $U_i^\alpha = 0$.

Now let us move to the situation we need. To this result, using again the linearity of the Stokes equations, we add the following known solutions to the Stokes equations:

- A background flow u_i^∞, with which a force-free sphere will advect with velocity $U_i^\alpha = u_i^\infty(\mathbf{x}_\alpha)$
- A particle velocity V_i^α, caused by an external force $6\pi\mu a V_i^\alpha$

We now have a particle moving under the influence of a background flow $\mathbf{u}^\infty$, a fluid velocity $\mathbf{u}'$ caused by the presence of the other particles, and a total force $6\pi\mu a V_i^\alpha - 6\pi\mu a(1 + \frac{a^2}{6}\nabla^2)u_i'(\mathbf{x}_\alpha)$, which moves with velocity $\mathbf{U}^\alpha = \mathbf{u}^\infty(\mathbf{x}_\alpha) + \mathbf{V}^\alpha$. Thus:

$$U_i^\alpha = u_i^\infty \mathbf{x}_(\alpha) + V_i^\alpha \tag{1.68}$$

$$F_i = 6\pi\mu a \left[V_i^\alpha - \left(1 + \frac{a^2}{6}\nabla^2\right) u_i'(\mathbf{x}_\alpha)\right] \tag{1.69}$$

and eliminating V^α between the two equations gives the required form, 1.55a:

$$U_i^\alpha - u_i^\infty(\mathbf{x}_\alpha) = \frac{F_i}{6\pi\mu a} + \left(1 + \frac{a^2}{6}\nabla^2\right) u_i'(\mathbf{x}_\alpha). \tag{1.70}$$

1.3.9 Mobility and Resistance Matrices

There is one final step in our model, this pulls together all of the previous work into a more usable form. We can now calculate:

- The velocity field generated by a single particle using singularity solutions.
- The force felt by a particle for a given induced velocity field as calculated above via the Faxén law.

We have two more hurdles to over come.

1. Inclusion of lubrication interactions.
2. Organising relations of the Faxén relations and the singularity solutions.

Both of these problems are solved via formulation of the resistance and mobility tensors. By the linearity of Stokes flow we know that the true extra velocity field $\mathbf{u}'$ must depend linearly on the forces, torques and stresslets applied to all spheres. Combining this observation with the Faxén relation of equation (1.55), we can deduce the the existence of a matrix called the grand mobility matrix $\mathcal{M}$ which relates the particle velocities and stresslets to the forces and torques applied to them and the background flow. In its full form the grand mobility matrix $\mathcal{M}$ is defined by

$$\begin{pmatrix} \mathbf{U} - \mathbf{u}^{\infty} \\ -\mathbf{E}^{\infty} \end{pmatrix} = \mathcal{M} \cdot \begin{pmatrix} \mathbf{F} \\ \mathbf{S} \end{pmatrix}. \tag{1.71}$$

Where vector $\mathbf{U}$ contains both the translational and rotational velocities of the particles and hence has dimension $6n$ (where n is the number of particles), and similarly $\mathbf{F}$ is the force / torque vector exerted by the particles on the fluid and also has dimension $6n$. We can think of the grand mobility matrix as

$$\mathcal{M} = \begin{pmatrix} \mathbf{M}_{UF} & \mathbf{M}_{US} \\ \mathbf{M}_{EF} & \mathbf{M}_{ES} \end{pmatrix}. \tag{1.72}$$

Where for example, we can form $\mathbf{M}_{UF}$, the small mobility matrix such that in the absence of stresslets,

$$\mathbf{U} - \mathbf{u}^{\infty} = \mathbf{M}_{UF} \cdot \mathbf{F}, \tag{1.73}$$

and its reverse $\mathbf{R}_{FU}$

$$\mathbf{F} = \mathbf{R}_{FU} \cdot (\mathbf{U} - \mathbf{u}^{\infty}), \tag{1.74}$$

where $\mathbf{R}_{FU}$ is the resistance matrix. Our discussion in section 1.3.5 relate the force, torque and stresslets to $\mathbf{u}'$ through equation (1.44), which is a truncated expansion for many particles) only accurate for well spaced particles. Combining this with the Faxén relations (1.55) we can calculate a far-field approximation to the grand mobility matrix, which we denote as $\mathcal{M}^{\infty}$. This is a far-field approximation to the true grand mobility matrix because of the truncation of equation (1.44) at $O(r^{-5})$, but it does include the irreducible quadrupole term (which can be expressed in terms of $\mathbf{S}$).

Method of Reflections

The mobility or resistance relations can be calculated in two ways,

1. from a combination of the singularity solutions and the Faxén laws, as above but if the singularity solutions are truncated the relations are only valid for well spaced particles.

2. using the method of reflections.

We will outline the method of reflections to show why we cannot solely consider well spaced spheres. We shall then continue to show the equivalence of inverting the mobility relations and the method of reflections.
To introduce the method of reflections two particles are considered and their effect on each other is reflected backwards and forwards resulting in the various relations in figure 1.5.
Consider two particles centred at $\mathbf{x}_1$ and $\mathbf{x}_2$ respectively. We define the background velocity as $\mathbf{u}_{\infty}$, the velocity induced by particle 1 as $\mathbf{u}_1$ and similarly the velocity induced by particle 2 as $\mathbf{u}_2$. Now consider the velocities on the particle surfaces S_1 and S_2. In order for each particle to be in solid body

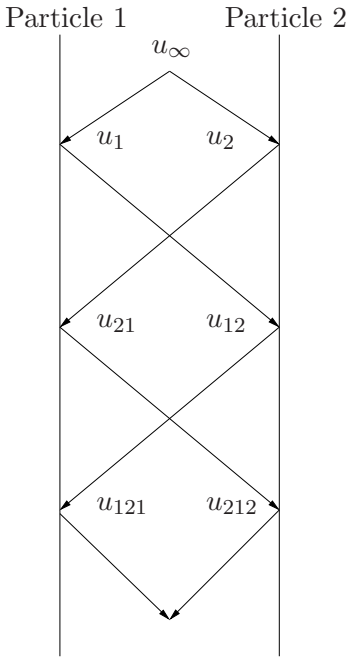

Figure 1.5: A pictorial representation of the method of reflections

motion, on S_1 we must have an induced velocity $\mathbf{u}_1$:

$$\mathbf{u}_1 = \mathbf{U}_1 + \omega_1 \times (\mathbf{x} - \mathbf{x}_1) - \mathbf{u}^\infty \tag{1.75a}$$

and on S_2,

$$\mathbf{u}_2 = \mathbf{U}_2 + \omega_2 \times (\mathbf{x} - \mathbf{x}_2) - \mathbf{u}^\infty \tag{1.75b}$$

with $\mathbf{U}_n$ and ω_n being the particle velocity and angular velocity respectively. However the fluid velocity depends on the the background flow $\mathbf{U}^\infty$ and the disturbance velocity of the two spheres,

$$\mathbf{u} = \mathbf{u}^\infty + \mathbf{u}_1 + \mathbf{u}_2. \tag{1.76}$$

Looking at this overall velocity, it is clear that there is a error in (1.75) on particle 1 from $\mathbf{u}_2$ and vice versa. The next reflection correction to adjust the boundary condition, i.e

$$\mathbf{u}_{12} = -\mathbf{u}_1 \quad \text{on } S_2 \tag{1.77a}$$

$$\mathbf{u}_{21} = -\mathbf{u}_2 \quad \text{on } S_1. \tag{1.77b}$$

As ever a picture paints a thousand words and the idea is presented in figure 1.5. In general these corrections continue indefinitely; however just as with the singularity solutions and multi-pole solutions due to the fact that we are dealing with spheres, for the two body problem we are able to derive an analytical form. The method of reflections can be applied to multiple particles, but it becomes much more demanding, requiring $n^2 - n$ velocity fields at each reflection step.

1.3.10 Equivalence of Inverting the Mobility Matrix and Summing Reflections

When we considered the multi-pole expansion we decided on an order to truncate the expansion; in an ideal world we would include all moments as this would include the lubrication interactions. Similarly when we are considering the method of reflections we also have to consider a point at which we should truncate our expansion. We wish to include all of the many body interactions and include all of the screening effects created by having the large number of particles, but we can not have an indefinite function considering all reflections. This equivalence is also shown in [21] from where the inspiration for this explanation was taken.

We wish to calculate the forces acting on the particles for a given flow for which we require the resistance matrix. We shall show that calculating the mobility matrix and inverting is equivalent to summing all of the reflected interactions. To achieve this, for simplicity instead of considering the singularity solutions as our mobility relations for a sphere, we shall consider the problem as point forces; the results still hold but it makes the algebra easier.

Consider two spheres 1 and 2 with sphere 2 moving towards number 1. We wish to calculate the force required to keep sphere 1 still. The disturbance velocity created by sphere 2 is

$$u_i = \frac{3}{4} J_{ij}(\mathbf{x} - \mathbf{x}_2) U_j^2. \tag{1.78}$$

The force felt by sphere 1 is

$$F_i^1 = -\frac{3}{4}J_{ij}(\mathbf{x}_1 - \mathbf{x}_2)U_j^2, \tag{1.79}$$

which is then itself reflected back through the fluid (as sphere 1 is fixed) producing the velocity field

$$u_i = \frac{3}{4}J_{ij}(\mathbf{x} - \mathbf{x}_{!2})F_j^1 = -\frac{3}{4}J_{ij}(\mathbf{x} - \mathbf{x}_{\mathbf{1}2})\frac{3}{4}J_{jk}(\mathbf{x}_1 - \mathbf{x}_2)U_k^2. \tag{1.80}$$

sphere 2 then exerts an extra force on the fluid due to the fluid velocity from sphere 1:

$$F_i^2 = \frac{3}{4}J_{ij}(\mathbf{x}_2 - \mathbf{x}_1)J_{jk}(\mathbf{x}_1 - \mathbf{x}_2)U_k^2 \tag{1.81}$$

causing the next disturbance flow

$$U_i = \frac{3}{4}J_{ij}(\mathbf{x} - \mathbf{x}_2)\frac{3}{4}J_{ij}(\mathbf{x}_2 - \mathbf{x}_1)J_{jk}(\mathbf{x}_1 - \mathbf{x}_2)U_k^2 \tag{1.82}$$

such that the force required on sphere 1, including both the first two reflections, is

$$F_i^1 = -\frac{3}{4}J_{ij}(\mathbf{x}_1 - \mathbf{x}_2)U_j^2 - \frac{3}{4}J_{ij}(\mathbf{x}_1 - \mathbf{x}_2)\frac{3}{4}J_{jk}(\mathbf{x}_2 - \mathbf{x}_1)\frac{3}{4}J_{kl}(\mathbf{x}_1 - \mathbf{x}_2)U_l^2 - ... \tag{1.83}$$

If we align our particle centres along an axis $J_{ij}(\mathbf{x}_1 - \mathbf{x}_2)$ simplifies to $\frac{2}{r}$, meaning that as we repeat the process we have a geometric series. Denoting the resistance function for sphere 1 to sphere 2 as X_{12}^A with a_{12}^2 being the corresponding mobility relation, we have

$$F^1 = X_{12}^A U^2 \tag{1.84}$$

and

$$\begin{aligned} X_{12}^A &= -\sum_{n=1}^{\infty}\left(\frac{3}{2r}\right)^{2n-1} \\ &= -\frac{\frac{3}{2r}}{\left(1-\left(\frac{3}{2r}\right)^2\right)} \\ &= -\frac{8r^2}{8r^2-9} \end{aligned} \tag{1.85}$$

Taking the singularity mobility functions from [21], namely $x^a_{11} = x^a_{22}$ and $x^a_{12} = x^a_{21} = \frac{3}{2r}$ and using the relationship shown in [34]

$$\begin{pmatrix} X^A_{11} & X^A_{12} \\ X^A_{21} & X^A_{22} \end{pmatrix} = \begin{pmatrix} x^A_{11} & x^A_{12} \\ x^A_{21} & x^A_{22} \end{pmatrix} \tag{1.86}$$

we have

$$\begin{pmatrix} 1 & 3/2r \\ 3/2r & 1 \end{pmatrix}^{-1} = \frac{r}{8r^2 - 9} \begin{pmatrix} 8r & -6 \\ -6 & 4r \end{pmatrix}. \tag{1.87}$$

So despite the fact that our mobility relations are calculated via the well spaced singularity solutions the inversion of the mobilities is equivalent to the summation of the infinite series of reflection.

1.3.11 Formulation of Stokesian Dynamics

When we use our far-field grand mobility matrix to simulate real flows, we will invert the matrix to form a far-field approximation to the grand resistance matrix, $\mathcal{R}^\infty$. Because $\mathcal{M}^\infty$ is approximate, lubrication interactions will not appear in $\mathcal{R}^\infty$. The lubrication interactions would only be included if all terms of the multipole expansion were included in $\mathcal{M}^\infty$. We shall explain how the lubrication interactions are included by considering the simpler model of equation (1.73) which does not include stresslets, then show how in the full model the stresslets are calculated in terms of given forces and imposed flow. The simpler method of equation (1.73) only considers the forces and torques, and is only valid in the absence of any imposed flow. The first step to include lubrication interactions is to invert $\mathbf{M}^\infty_{UF}$, the far-field approximation to $\mathbf{M}_{UF}$, the matrix which contains all force-velocity interactions. We invert the matrix $\mathbf{M}^\infty_{UF}$ to form a far-field approximation to the resistance matrix $\mathbf{R}_{FU}$, which we denote $\mathbf{R}^\infty_{FU}$. We now have an approximation to many-body interactions. In particular, the "screening" effects of large numbers of particles, to hide one another's effects, are well captured by this new resistance matrix. This

inversion is equivalent to the summing of all of the reflected interactions, as demonstrated in section 1.3.10.

To include the lubrication interactions, we add on the known two sphere resistance interactions $\mathbf{R}_{2B}$ to the far-field resistance matrix $\mathbf{R}_{FU}^{\infty}$. It is effectively the sum of several sparse matrices, each describing the interaction between one pair of spheres. The far field part of the two body resistance matrix has already been included into the inversion of $\mathbf{M}_{UF}^{\infty}$, so we must subtract these interactions to avoid counting them twice. This is simply done by creating several sparse two body mobility matrices to the same order as $\mathbf{M}_{UF}^{\infty}$. Inverting these matrices individually and summing them forms $\mathbf{R}_{2B}^{\infty}$. The composition of our resistance matrix for the forces and torques model is shown in equation (1.88):

$$\mathbf{R}_{FU} = (\mathbf{M}_{UF}^{\infty})^{-1} + \mathbf{R}_{2B} - \mathbf{R}_{2B}^{\infty}. \tag{1.88}$$

The same method is used for the complete model which includes stresslets. The full resistance matrix $\mathcal{R}$ is again simply the inverse of the grand mobility matrix $\mathcal{M}$ defined in equation (1.71), and this is shown in equation (1.89).

$$\begin{pmatrix} \mathbf{F} \\ \mathbf{S} \end{pmatrix} = \mathcal{R} \cdot \begin{pmatrix} \mathbf{U} - \mathbf{U}^{\infty} \\ -\mathbf{E}^{\infty} \end{pmatrix}, \tag{1.89}$$

with

$$\mathcal{R} = \begin{pmatrix} \mathbf{R}_{FU} & \mathbf{R}_{FE} \\ \mathbf{R}_{SU} & \mathbf{R}_{SE} \end{pmatrix}. \tag{1.90}$$

The construction of $\mathcal{R}$ is done in just the same way as in (1.88):

$$\mathcal{R} = (\mathcal{M}^{\infty})^{-1} + \mathcal{R}_{2B} - \mathcal{R}_{2B}^{\infty}. \tag{1.91}$$

Here $\mathcal{M}^{\infty}$ is the approximation of the grand mobility matrix truncated at $O(r^{-5})$ as constructed in equation (1.71). The second and third terms add the lubrication interactions to $\mathcal{R}$. The second term $\mathcal{R}_{2B}$ contains the known exact interactions between any two spheres, while the third term is present only to avoid double-counting.

In a simulation, typically the stresslets $\mathbf{S}$ and particle velocities $\mathbf{U}$ are unknown, while the external forces $\mathbf{F}$ and background flow field $\mathbf{E}^\infty$ are known. Having constructed $\mathcal{R}$, we can then express the velocities in terms of the known forces, torques and imposed linear flow field (by manipulation of the top row of equation (1.89)):

$$\mathbf{U} - \mathbf{U}^\infty = \mathbf{R}_{FU}^{-1} \cdot \left[\mathbf{F} + \mathbf{R}_{FE} : \mathbf{E}^\infty\right], \tag{1.92}$$

This in turn allows us to express the stresslets in terms of the given forces and torques and the imposed flow (using the bottom row of equation (1.89)):

$$\mathbf{S} = \mathbf{R}_{SU} \cdot \mathbf{R}_{FU}^{-1} \cdot \mathbf{F} + \left[\mathbf{R}_{SU} \cdot \mathbf{R}_{FU}^{-1} \cdot \mathbf{R}_{FE} - \mathbf{R}_{SE}\right] : \mathbf{E}^\infty. \tag{1.93}$$

The Stokesian Dynamics algorithm is, in basic terms:

1. Construct the far-field approximation $\mathcal{M}^\infty$ to the mobility matrix from equation (1.55).

2. Invert $\mathcal{M}^\infty$ and construct $\mathcal{R}^\infty$ and hence $\mathcal{R}$ as in equation (1.91).

3. Find $\mathbf{U} - \mathbf{U}^\infty$ from equation (1.92) and the stresslets $\mathbf{S}$ from equation (1.93).

4. Move all of the particles according to our new $\mathbf{U}$; compute the total fluid stress (if needed) from $\mathbf{S}$.

Ideally we should reconstruct and invert $\mathcal{M}^\infty$ after each time step as the particles will have moved. This matrix inversion, however, is one of the most computationally expensive steps of the whole process and to do it every step is not necessary for accuracy. Instead a condition may be set such that, as soon as a particle has moved out of its shadow, the mobility matrix is recalculated, or recalculated every m time steps.

This model now includes the many body interactions and lubrication interactions without having to resort to an infinite series. We have used the properties of a sphere to produce a singularity solution, the Faxén Laws, and finally the

known interbody interactions in a two body resistance matrix to construct the model that we shall be using for the rest of our work.

As with any model there are various assumptions. We are assuming that the domain is infinite, the fluid is incompressible and that the inertia is negligible and hence that every particle reacts instantly to the actions of the others. The instant reaction to any change in conditions is clearly unphysical but is probably not an issue. We are assuming that our particles are perfectly spherical, of equal radius, and of course non-deformable. As a consequence of the Stokes equations the particles are never allowed to touch (under the action of finite forces) due to the lubrication force which exists when the distance between any two approaching particles is very small. We will neglect gravity in our computations (though this is not a limitation of Stokesian Dynamics itself) so that we may study the effect of the particles alone on the flow and stresses. We are also, as previously stated, ignoring any particle contributions to the pressure.

1.3.12 Validation of Stokesian Dynamics

The validation of Stokesian Dynamics in Dratler's 1996 paper [20] compares with established experimental data, and the results are deemed to be within accepted limits of error. However the paper does warn of the problem of overlapping particles when simulating densely packed systems on models without stochastic or repulsive forces, i.e. purely hydrodynamic models, with no Brownian motion. It is possible to overcome this problem by reducing the timestep, but this becomes too computationally expensive to be realistic. The solution to this problem is suggested in [9]. It involves calculating the interactions as if the distances between the particles are small when overlapping of particle boundaries occurs, this is the solution we use when implementing SD.

1.3.13 Ewald Summation

Stokesian Dynamics works well and captures the key rheological features; however, it does not cope with an infinite population of particles (as we would need for an infinite suspension) without modification. Brady and coworkers [13] extended Stokesian Dynamics to infinite suspensions, further extending the work of O'Brien [47] using a periodic lattice and Ewald sums. Ewald summation is widely used in systems with periodic boundary conditions. The trick in any system which flows is to find a lattice which is self-replicating in time under the transform of the imposed flow. We will return to that issue in chapter 2. The aim of our work there is to develop a self-replicating lattice for all two-dimensional linear flow fields. The essence is to find a periodic lattice which will repeat under a general linear flow, one which contains a combination of shear, strain, and rotation. This covers all linear two-dimensional flows. In three dimensions a periodic lattice cannot be found for all flows: for example a self-replicating lattice under uniaxial strain does not exist; this is proved by Sami in his MSc thesis [50].

The Ewald summation technique works by using a box with a limited number of particles within it. The box is tessellated over the entire domain to create a lattice. The effects of the periodic lattice are summed to imitate the effect of a much larger domain. Ewald summation then allows this lattice summation to be done efficiently over an infinite domain. The summation is split into near field and far field parts, the near field being summed in real space and the far-field being summed in a reciprocal space; the space after a Fourier transform. This allows the summation in both spaces to be truncated as they both work "from opposite ends" of the space and converge quickly in their respective domains. An Ewald sum for the Stokes Oseen tensor J_{ij} was first carried out by Beenakker [7], who refers to it as the Rotne-Prager tensor. This carries roughly the same computational cost as doing the contour integral 1.29 over all particles within the periodic box.

1.3.14 Two-dimensional systems

In this thesis we consider a variety of linear flows which have never been studied before for suspensions, ranging from planar straining flow, through shear flow to pure solid-body rotation. Of course, each of these examples is well-known; but the intermediate cases are new. To investigate the dynamics of the suspension under the action of these two-dimensional flows, we know that the interesting behaviour will occur within the plane of the flow, so we can save computational expense by simulating a monolayer of particles. These are, nonetheless, spherical particles in a three-dimensional domain of fluid.

Monolayers are also used as a testing ground for for new numerical regimes before time-consuming fully three-dimensional calculations are commenced. Monolayers were considered by Wilson and Davis [64] where they consider the shear stress in a monolayer of rough spheres, both considering dilute concentrations analytically and using Stokesian Dynamics for higher concentrations. Another motivation for considering systems which are periodic in only two dimensions is when considering suspensions in a confined geometry (for instance, to study jamming phenomena). In such a geometry it does not make sense to tessellate space isotropically in all three dimensions. Rather, we need to be able to use a simulation cell which replicates periodically in two dimensions but not in the third (in which it is bounded by, for instance, solid walls or a free surface). For this reason, in Appendix A of this thesis we will develop the theory of Ewald summation applied to hydrodynamic mobility functions, but in this case working in only two spatial dimensions rather than the three dimensions of Brady [13].

1.3.15 Latest developments in Stokesian Dynamics

The latest extension to Stokesian Dynamics is by Brady [52], where he puts forward the idea of a fast Fourier transform method. This method, known as Accelerated Stokesian Dynamics (ASD) is a fast method with calculations of

the order $0(N(N))$ (where N is the number of particles in the periodic box). The downside is a small loss in accuracy. ASD is very powerful but has only been implemented for shear flows.

The computationally costly part of Stokesian dynamics is the construction and inversion of the far field mobility matrix. ASD works by considering the Ewald sum for the far-field many body interactions. The difference here is that the Ewald sum is discretised. It uses a summing method described by Darden in [16] which is based on particle mesh Ewald (PME) as outlined by Hockney in [32]. There is some loss of accuracy by using the PME but it is acceptable given the speed increase. ASD may initially seem unnecessary as a self replicating basis can surely just be reduced in size such that a given concentration can be achieved by having a sufficiently small size of the lattice. However some phenomena cannot be observed using a periodic cell with too few particles, so efficient computation with large numbers of particles is still important. For example, in three dimensions volume fractions above 0.49 cause crystallisation and glassing, and with a simulation box which is too small, crystals can easily span the periodic box. Due to the fact that we are dealing with a two dimensional flow however, crystallisation occurs at higher area concentrations than the critical volume fractions in three dimensions. Problems containing fibre suspensions (which can be imitated with chains of spheres) also require large lattices due to the length of fibres.

Blanc, Peters and Lemaire [8] conducted experiments on the shear viscosity of a concentrated non-Brownian suspension. The shear flow is created by means of two concentric cylinders once stationary and one rotating. They consider a shear flow which is then reverse and this effect of shear viscosity. This results an initial drop in viscosity followed by a rise to a plateaux. Higher concentrations resulted in a more pronounced step between low viscosity value and high plateaux. It is hypothesised that at the viscosity minimum the suspension is isotropic and anisotropic upon reaching it's viscosity plateaux. Results are considered to be in agreement with stokesian dynamics experiments.

1.3.16 Latest developments in suspension mechanics

In some of the most recent numerical work on suspensions, Sandeep [39] considers the particle volume fractions around which crystallisation and glassing occur in shear flow. They then seek to determine whether ordering and other responses are a feature of near hard sphere dispersions, by using Accelerated Stokesian Dynamics with the addition of Brownian motion.

Ahamadi in [45] uses a finite element method and a self replicating lattice with shear flow and planar extension with no Brownian motion, for a suspension in which the particles are deformable and the surrounding fluid viscoelastic. The complication of the viscoelastic fluid, in particular, means that methods such as SD and ASD which exploit the properties of Stokes flow cannot be used. The particles contribute to the elastic-like non-Newtonian aspect of the rate of strain tensor.

1.4 Brady Team's latest developments

Brady and co-workers have extended the method of Stokesian Dynamics in several different directions away from the original simulation of force-free identical spheres in shear flow with Ewald summation for the far-field terms. We give a brief section over to Brady's team latest developments in the area of suspension dynamics due to his positions in the field. In more recent years the Brady team have considered some different problems in the area of suspensions.

Brady in 2006 [55] considered the case of a compressible flow and developed a new resistance function for two rigid spheres in a low-Reynolds-number flow. This was done using the method of reflections and also considered different sized spheres.

In [35] Brady considers a model with Brownian motion. Two particles are considered to be moving through a colloidal dispersion one behind another.

He found that fore-aft symmetry was broken at a sufficiently small separation when $Pe > 1$, (i.e. advection > diffusion), and observed a bulldozer effect, where the first particle clears a path for the second particle, when separation is larger. For large $Pe \gg 1$ the entropic (thermal) force disappears on then on trailing probe.

In 2007 [55] an expansion is considered to be the driving force with retarded by the thermal motion of the particles. This is done by considering the suspension to be macroscopically compressible. Bulk viscosity is the calculated quantity and G. I Taylor's results for expanding bubbles are shown to be recovered. A dissipation of energy in the fluid occurs due to differing expansion rates between fluid and particles resulting in a higher bulk viscosity. A hard sphere inter-particle interaction is considered and is shown to reduce bulk viscosity consistent with the findings for sheet viscosity of many papers on rough spheres. The study was for small Pe number (our study is in the limit as Pe $\to \infty$) the authors mention the possibility that a high Pe bulk viscosity may not exist.

1.5 Content of this thesis

The aim of this thesis is to study the response of hard-sphere suspensions to a variety of linear flows in two dimensions.

Chapter 2 begins by introducing the concept of a self-replicating lattice. The concept of a minimal basis is introduced, and illustration is made with the simple example of a repeating box for a shear flow and the more complicated known repeating box for a plane strain flow. We then derive a self-replicating basis for a mixed flow between strain and shear, and secondly for a mixed flow between shear and rotation. Finally, proof is given that the velocity gradient tensors we have considered cover all two-dimensional linear flows.

The following chapter, chapter 3 shows results from Stokesian Dynamics simulations of the mixed shear / strain / rotation flows for various particle concen-

trations and flow combinations. Initial results are shown for the instantaneous viscosity of a random configuration of particles, with further results from dynamic runs to ascertain the long-time dependence and transient behaviour of the viscosity and normal stress on flow type and particle concentration.

Chapter 4 considers rough spheres and the effect of surface roughness on suspension rheology. Two models for surface roughness are considered, a hard contact model and a soft contact model.

Finally, chapter 5 recaps on the results of the thesis and also considers what future research may be undertaken.

Appendix A introduces Ewald summation and attempts to derive a two-dimensional form of the Ewald sums. The modified real space mobility relations are derived and listed to allow the modelling of a infinite two dimensional system and the difficulties of deriving the reciprocal space summations are discussed.

Chapter 2

Periodic Basis for Linear Flows

When considering a large domain, the computational cost of simulating a system clearly becomes larger as the number of bodies being simulated increases. If it is possible to replace a large, roughly homogeneous system with a smaller cell repeated periodically throughout space, the computational cost can be greatly reduced. We are considering a situation where the flow is spatially homogeneous, which naturally lends itself to this sort of treatment. We need to find a lattice of cells for each flow, which can be repeated throughout space, and where the basis is temporally periodic: that is, after some time T the lattice points (though not necessarily the cells themselves) have moved so that each of the original lattice points now lies on a lattice point again. We can then use the lattice to create a tessellated structure throughout space; each particle is then repeated within every cell, keeping the same relative position within each cell.

The problem to be considered in this chapter is that of implementing such a self-replicating periodic box within a flow. This will allow us to consider an infinite domain by only modelling one box or cell within a lattice. This has been shown to work for a shear flow by Adler and Brenner [3]. This work

was extended and shown to work for plane strain flow in an M.Sc. thesis by Sami [50]. In the same work it was also shown that there is no self-replicating lattice for either a uniaxial or biaxial straining flow. In this section we shall extend this method to work for a two dimensional linear flow which linearly combines shear, rotation and plane strain flow. Much of the general setup of the problem is based on the M.Sc. work of Sami in [50].

2.1 Lattice and its Basis

We consider a linear flow of the form

$$\mathbf{U}(\mathbf{x}) = \mathbf{G} \cdot \mathbf{x}, \tag{2.1}$$

where $\mathbf{G}$ is traceless for an incompressible flow, and we will consider the motion of the lattice points

$$\mathbf{x} = \mathbf{B} \cdot \mathbf{Z}, \quad \mathbf{Z} \in \mathbb{Z}^n. \tag{2.2}$$

Here $\mathbf{U}$ is the flow velocity vector, $\mathbf{G}$ is the rate of strain tensor and $\mathbf{x}$ is the position vector in Cartesian coordinates. $\mathbf{B}$ is a basis spanning $\mathbb{R}^n$, $n \in \{2, 3\}$, written as a matrix of column vectors. The vector $\mathbf{Z}$ has integer components so equation (2.2) defines a lattice; an example of this is shown in figure 2.1 with a strain flow imposed. A basis for a given lattice is any set of spanning vectors $\mathbf{b}_1$, $\mathbf{b}_2$ ($\mathbf{b}_3$ in three dimensions) such that every lattice point can be expressed as a linear integer combination of $\mathbf{b}_i$, i.e. $\sum_{i=1}^{n} \alpha_i \mathbf{b}_i$ where $\alpha_i \in \mathbb{Z}$. For a given set of lattice points, however, the spanning basis is not unique, we shall consider a linear combinations of elements within $\mathbf{B}$ with the aim of creating a minimal basis.

2.1.1 Properties of a minimal basis

A minimal set of basis vectors is the set of basis vectors $\mathbf{b}_i$ that satisfy equation (2.2) for each lattice point such that the quantity

$$\Sigma_i \left|\mathbf{b}_i\right|, \tag{2.3}$$

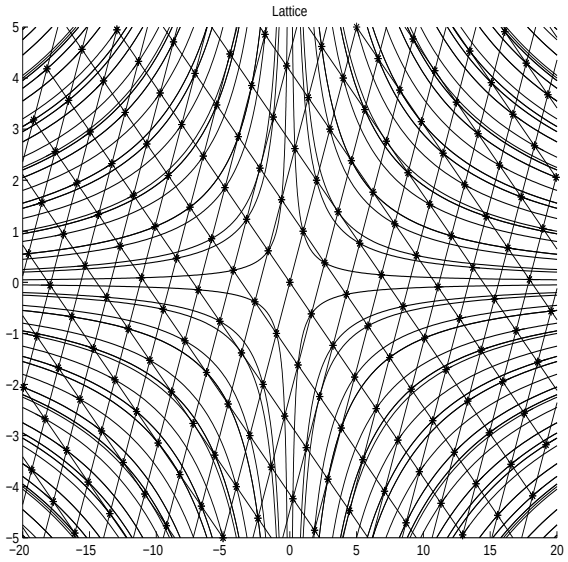

Figure 2.1: Example of a lattice with strain flow

is minimised over all possible bases satisfying (2.2).

The concept of a minimal basis is slightly confusing as if we imagine a lattice of nodes and choose a combination of basis vectors to span the lattice our natural inclination will be to create a minimal basis. Intuitively the minimal basis is the "best" basis, most "natural" basis as it were.

In chapter five of his M.Sc. thesis [50], Sami states that the conditions for a basis to be minimal are

$$|\cos\theta_{ij}| \leq \frac{1}{2}\min\left(\frac{|\mathbf{b}_j|}{|\mathbf{b}_i|}, \frac{|\mathbf{b}_i|}{|\mathbf{b}_j|}\right) \tag{2.4}$$

where θ_{ij} is the angle between the basis vectors $\mathbf{b}_i$ and $\mathbf{b}_j$, for each pair of basis vectors. However while condition (2.4) is sufficient in two dimensions it proves to be insufficient in three dimensions. This can be proved by counterexample.

Consider the three-dimensional basis:

$$\begin{aligned} \mathbf{B} &= \begin{pmatrix} 1 & -1/2 & -1/2 \\ 0 & \sqrt{3}/2 & -\sqrt{3}/2 \\ \varepsilon & \varepsilon & \varepsilon \end{pmatrix} \\ \mathbf{b}_1 = \begin{pmatrix} 1 \\ 0 \\ \varepsilon \end{pmatrix} \quad \mathbf{b}_2 &= \begin{pmatrix} -1/2 \\ \sqrt{3}/2 \\ \varepsilon \end{pmatrix} \quad \mathbf{b}_3 = \begin{pmatrix} -1/2 \\ -\sqrt{3}/2 \\ \varepsilon \end{pmatrix} \end{aligned} \tag{2.5}$$

where $\varepsilon \ll 1$ is a real non zero parameter. This example basis satisfies the minimal condition given by equation (2.4) but there exists a linear combination which is shorter than any of the basis lengths, namely

$$\mathbf{b}_1 + \mathbf{b}_2 + \mathbf{b}_3 = \begin{pmatrix} 0 \\ 0 \\ 3\varepsilon \end{pmatrix}, \tag{2.6}$$

which is obviously a linear combination of the original basis vectors whose length can be made smaller than any of $|\mathbf{b}_i|$ by setting $\varepsilon < \frac{1}{3}$. The new basis

$$\mathbf{B}' = \{\mathbf{b}_1, \mathbf{b}_2, \mathbf{b}_1 + \mathbf{b}_2 + \mathbf{b}_3\} \tag{2.7}$$

has a lower total length than our original basis $\mathbf{B}$ and spans the same lattice. For a minimal constraint that is valid in three dimensions it is necessary to check for a shorter vector that could replace one of vectors: that is, seek $\mathbf{b}'_i$ such that

$$|\mathbf{b}'_i| < |\mathbf{b}_i| \tag{2.8}$$

with

$$\mathbf{b}'_i = \mathbf{b}_i + m\mathbf{b}_j + n\mathbf{b}_k, \tag{2.9}$$

for some integers m and n. If the basis is minimal, no such vector exists, and instead

$$\left|\mathbf{b}'_i\right| \geq |\mathbf{b}_i|\,, \tag{2.10}$$

for all m, n. We can easily construct such a condition if we restrict ourselves to the case where all of the original basis vectors are the same length, and consider only the cases $m = \pm 1$, $n = \pm 1$. Consider

$$|\mathbf{b}_i'|^2 = |\mathbf{b}_i|^2 + |\mathbf{b}_j|^2 + |\mathbf{b}_k|^2 \pm 2\mathbf{b}_i \cdot \mathbf{b}_j \pm 2\mathbf{b}_i \cdot \mathbf{b}_k \pm 2\mathbf{b}_j \cdot \mathbf{b}_k. \tag{2.11}$$

We are looking for

$$\begin{aligned} &|\mathbf{b}_i'| < |\mathbf{b}_i| \\ &\Rightarrow 0 < b_j^2 + b_k^2 \pm 2\mathbf{b}_i \cdot \mathbf{b}_k \pm 2\mathbf{b}_i \cdot \mathbf{b}_j \pm 2\mathbf{b}_j \cdot \mathbf{b}_k. \end{aligned} \tag{2.12}$$

Assuming all of the vectors are the same length, this yields

$$\begin{aligned} &0 < b^2 + b^2 \pm 2b^2 \cos\theta_{13} \pm 2b^2 \cos\theta_{12} \pm 2b^2 \cos\theta_{23} \\ &\Rightarrow \sum_{i=1}^{3} |\cos\theta_i| < 1. \end{aligned} \tag{2.13}$$

The case where all of the vectors are the same length is very specialised and needs to be generalised.

The condition (2.13) is necessary but perhaps not sufficient in cases where the basis lengths are not equal. This represents the same idea as condition (2.4) but taken between each pair of bases rather than each pair of vectors. However our bases will all be two dimensional in this thesis and therefore this condition is superfluous to our needs but useful to help with understanding of the model.

2.2 The Flow

Returning to equation (2.1) we seek the appropriate repeating basis for a flow. If we solve equation (2.1) for lattice points advecting with the flow (for which $\dot{\mathbf{x}} = \mathbf{U}(\mathbf{x})$) we get

$$\mathbf{x}(t) = \exp(\mathbf{G}t) \cdot \mathbf{x}(0). \tag{2.14}$$

$\mathbf{G}$ is traceless due to incompressibility and the trace is an invariant so $\exp(\mathbf{G}t)$ is also traceless. If our lattice is self replicating the vertices of the lattice must

all map onto vertices for some time T (discussed in sections 2.3.2 and 2.2.2). The consequence of this is that if we consider a vertex of the lattice it must be mapped in time T onto a linear integer combination of the basis vectors:

$$\exp(\mathbf{G}T)\,\mathbf{B} = \mathbf{B}\,\mathbf{M}, \qquad \mathbf{M} \in \mathbb{Z}^n \times \mathbb{Z}^n. \tag{2.15}$$

We consider $\mathbf{G}$ to only have real eigenvalues values for now. We shall restrict ourselves to matrices which we are diagonalisable (and revisit this assumption in section 2.3.1). We will return to the case with complex eigenvalues in section 2.3.4. We take

$$\mathbf{G} = \mathbf{V}\,\mathbf{\Lambda}\,\mathbf{V}^{-1}, \tag{2.16}$$

so by standard diagonalisation methods columns of $\mathbf{V}$ are right eigenvectors of $\mathbf{G}$ and $\mathbf{\Lambda}$ is a diagonal matrix with the corresponding eigenvalues of $\mathbf{G}$. As $\mathbf{G}$ is traceless and the trace is invariant we can say,

$$\mathbf{\Lambda} = \begin{pmatrix} \lambda_1 & 0 & 0 \\ 0 & \lambda_2 & 0 \\ 0 & 0 & -\lambda_1 - \lambda_2 \end{pmatrix}. \tag{2.17}$$

We shall ignore the case $\lambda_1 = \lambda_2$, as this corresponds to uniaxial and biaxial strain, and it is proven in [50] that uniaxial and biaxial strain do not have a self replicating basis. We have also eliminated the case of shear flow, in which $\mathbf{G}$ does not diagonalise. As we shall see later in section 2.3.1, shear flow has a very simple basis and so this analysis is not needed in that particular case. We order the three eigenvalues so that $\lambda_1 > \lambda_2 > -(\lambda_1 + \lambda_2)$ and thus $\lambda_1 > 0$. From equation (2.14)

$$\exp(\mathbf{G}T) = \mathbf{V}\,\exp(\mathbf{\Lambda}T)\,\mathbf{V}^{-1}, \tag{2.18}$$

and also

$$\begin{aligned}\exp(\mathbf{\Lambda} T) &= \begin{pmatrix} e^{\lambda_1 T} & 0 & 0 \\ 0 & e^{\lambda_2 T} & 0 \\ 0 & 0 & e^{-(\lambda_1+\lambda_2)T} \end{pmatrix} \\ &= \begin{pmatrix} S & 0 & 0 \\ 0 & S^{\nu} & 0 \\ 0 & 0 & S^{-(1+\nu)} \end{pmatrix} = \mathbf{S},\end{aligned}$$

with $S = \exp(\lambda_1 T) > 1$ and $\nu = \lambda_2/\lambda_1 \in (-1/2, 1)$. Now using this information we can use equation (2.15) to state that finding the basis is equivalent to solving

$$\begin{pmatrix} S & 0 & 0 \\ 0 & S^{\nu} & 0 \\ 0 & 0 & S^{-(1+\nu)} \end{pmatrix} \mathbf{B} = \mathbf{B}\,\mathbf{M}. \tag{2.19}$$

Due to the fact that $\exp(\mathbf{\Lambda} T)$ is diagonal, the eigenvalues of $\mathbf{M}$ are $\mu_i = \exp(\lambda_i T)$ and the the rows of $\mathbf{B}$ are the left eigenvectors of $\mathbf{M}$.

2.2.1 Example: Basis Vectors for Plane Strain

If we consider a plane strain flow, i.e. $\nu = 0$, our problem is

$$\begin{pmatrix} e^{\lambda T} & 0 & 0 \\ 0 & 0 & 0 \\ 0 & 0 & e^{-\lambda T} \end{pmatrix} \mathbf{B} = \mathbf{B}\,\mathbf{M}. \tag{2.20}$$

This can easily be reduced to

$$\begin{pmatrix} S & 0 \\ 0 & S^{-1} \end{pmatrix} \mathbf{B} = \mathbf{B}\,\mathbf{M}, \tag{2.21}$$

by neglecting the third dimension, in which nothing moves, and this is equivalent to the strain flow,

$$\mathbf{U} = \begin{pmatrix} \lambda & 0 \\ 0 & -\lambda \end{pmatrix} \cdot \mathbf{x}. \tag{2.22}$$

There are two invariants between $\mathbf{S}$ and $\mathbf{M}$:

1. $\mathrm{Tr}(\mathbf{M}) = \mathrm{Tr}(\mathbf{S})$,

2. $\det(\mathbf{M}) = \det(\mathbf{S}) = 1$.

Since $\mathrm{Tr}(\mathbf{S}) = S + S^{-1}$ and $S \geq 1$ we have $\mathrm{Tr}(\mathbf{S}) \geq 2$, but if $\mathrm{Tr}(\mathbf{S}) = 2$ then $S = 1$ which represents no motion, so we can say $\mathrm{Tr}(\mathbf{S}) > 2$. Then $\mathrm{Tr}(\mathbf{M}) > 2$ and as $M_{ij} \in \mathbb{Z}$, we can say $\mathrm{Tr}(\mathbf{M}) \geq 3$.

Without loss of generality, let

$$\mathbf{B} = \begin{pmatrix} A\cos\theta_1 & \cos\theta_2 \\ A\sin\theta_1 & \sin\theta_2 \end{pmatrix}. \tag{2.23}$$

If we substitute this into equation (2.21) we can show that

$$\frac{\cos\theta_1}{\cos\theta_2} = \frac{S - M_{22}}{AM_{12}} = \frac{M_{21}}{A(S - M_{11})}, \tag{2.24}$$

and

$$\frac{\sin\theta_1}{\sin\theta_2} = \frac{S^{-1} - M_{22}}{AM_{12}} = \frac{M_{21}}{A(S^{-1} - M_{11})}. \tag{2.25}$$

Using the trace invariant, we can write $S^{-1} = \mathrm{Tr} - S = M_{11} + M_{22} - S$, giving:

$$\frac{\sin\theta_1}{\sin\theta_2} = \frac{M_{11} - S}{AM_{12}} = \frac{M_{21}}{A(M_{22} - S)}. \tag{2.26}$$

There are many possible solutions; however any self replicating lattice in two dimensions will have orthogonal basis vectors at some point during its period of repetition so for convenience we choose $\theta_1 = \theta_2 + (\pi/2)$ to obtain

$$\tan\theta_1 = \frac{AM_{12}}{S - M_{22}} = \frac{A(S - M_{11})}{M_{21}} = \frac{S - M_{11}}{AM_{12}} = \frac{M_{21}}{A(S - M_{22})}. \tag{2.27}$$

This gives $M_{21} = A^2 M_{12}$ and

$$\tan\theta_1 = \frac{AM_{12}}{S - M_{22}} = \frac{S - M_{11}}{AM_{12}}. \tag{2.28}$$

If we additionally take $A = 1$ and hence $M_{12} = M_{21}$ we obtain

$$\tan\theta_1 = \frac{M_{12}}{S - M_{22}} = \frac{S - M_{11}}{M_{12}}, \tag{2.29}$$

and using the trace invariant, we obtain

$$M_{11}M_{22} - 1 = M_{12}^2. \tag{2.30}$$

If we choose $M_{12} = 0$ this would give the solution of $S = 1$, i.e. stationary flow, which is of no interest to us. So we take $M_{11} = M_{12} = M_{21} = 1$ and $M_{22} = 2$. Substituting into equation (2.29) gives us $S = (3 \pm \sqrt{5})/2$ (or, since we specified $S > 1$, in fact $S = (3 + \sqrt{5})/2$) and hence the basis

$$\mathbf{B} = k \begin{pmatrix} 1 & (1+\sqrt{5})/2 \\ (1+\sqrt{5})/2 & -1 \end{pmatrix}, \tag{2.31}$$

where k is just a normalising constant.

The self-replication time is given by

$$S = \frac{3+\sqrt{5}}{2} = e^{\lambda_1 T}, \tag{2.32}$$

$$T = \frac{1}{\lambda_1} \ln\left(\frac{3+\sqrt{5}}{2}\right). \tag{2.33}$$

We could find other bases which would repeat in the same repeat time T and with the same matrix $\mathbf{M}$, simply by removing the restriction $\theta_1 = \theta_2 + (\pi/2)$. One example is the basis derived in [50] for plane strain flow:

$$\mathbf{B} = \begin{pmatrix} 1 & (1+\sqrt{5})/2 \\ 1 & (1-\sqrt{5})/2 \end{pmatrix}, \tag{2.34}$$

which it is straightforward to show also satisfies equation (2.21), $\mathbf{S}\,\mathbf{B} = \mathbf{B}\,\mathbf{M}$:

$$\mathbf{S}\,\mathbf{B} = \begin{pmatrix} \frac{3+\sqrt{5}}{2} & 0 \\ 0 & \frac{3-\sqrt{5}}{2} \end{pmatrix} \begin{pmatrix} 1 & \frac{1+\sqrt{5}}{2} \\ 1 & \frac{1-\sqrt{5}}{2} \end{pmatrix} = \begin{pmatrix} \frac{3+\sqrt{5}}{2} & 2+\sqrt{5} \\ \frac{3-\sqrt{5}}{2} & 2-\sqrt{5} \end{pmatrix};$$

$$\mathbf{B}\,\mathbf{M} = \begin{pmatrix} 1 & \frac{1+\sqrt{5}}{2} \\ 1 & \frac{1-\sqrt{5}}{2} \end{pmatrix} \begin{pmatrix} 1 & 1 \\ 1 & 2 \end{pmatrix} = \begin{pmatrix} \frac{3+\sqrt{5}}{2} & 2+\sqrt{5} \\ \frac{3-\sqrt{5}}{2} & 2-\sqrt{5} \end{pmatrix}.$$

2.2.2 Independence of Relative Particle Velocity on Box Choice

This is the underlying concept on which the idea of a self replicating basis rests: the fact that the evolution of the position of a given point relative to its lattice box is independent of which lattice box it is in. If we consider a

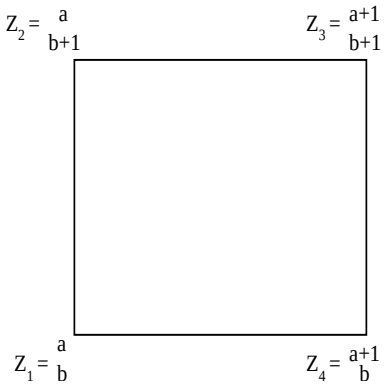

Figure 2.2: A generic box

generic lattice box we can show that the evolution of the relative position of a test point is independent of the choice of box.

We shall consider one box from our lattice, shown in figure 2.2. Any box in the lattice is created by the basis matrix $\mathbf{B}$. We shall label the corners of our box $\mathbf{x}_r$, $r = 1$–4 in a clockwise direction, generated by

$$\mathbf{x}_r = \mathbf{B} \cdot \mathbf{Z}_r, \qquad r = 1 \ldots 4, \tag{2.35}$$

where the integer vectors $\mathbf{Z}_r$ are shown on figure 2.2. For instance, the position of the corner shown at bottom left is

$$\mathbf{x}_1 = \mathbf{B} \cdot \mathbf{Z}_1 = \mathbf{B} \cdot \begin{pmatrix} a \\ b \end{pmatrix} = a\,\mathbf{b}_1 + b\,\mathbf{b}_2.$$

We shall denote the relative position within the box in terms of the basis vectors: i.e. by the local coordinates $x', y' \in [0, 1]$. A particle lying between corners 1 and 4 has $y' = 0$; one lying between corners 1 and 2 would have $x' = 0$. Thus the absolute position of the point would be

$$\mathbf{x} = (a + x')\,\mathbf{b}_1 + (b + y')\,\mathbf{b}_2 = \mathbf{x}_1 + \mathbf{B} \cdot \begin{pmatrix} x' \\ y' \end{pmatrix}. \tag{2.36}$$

The flow is governed by equation (2.14):

$$\begin{pmatrix} x \\ y \end{pmatrix} = \exp(\mathbf{G}t) \cdot \begin{pmatrix} x_0 \\ y_0 \end{pmatrix} \tag{2.37}$$

where $\mathbf{G}$ is the rate of strain tensor.

Consider a point somewhere in a box, whose position vector $\mathbf{x}(t)$ is governed by equation (2.37). The relative position within that box $\mathbf{x}'(t)$ can be expressed in terms of the absolute position by

$$\mathbf{x}'(t) = \begin{pmatrix} x' \\ y' \end{pmatrix} = \mathbf{B}^{-1} \cdot (\mathbf{x}(t) - \mathbf{O}(t)) \,, \tag{2.38}$$

where $\mathbf{O}(t)$ represents the origin of the box at time t, shown in figure 2.2 as $\mathbf{O}(t) = \mathbf{x}_1$.

The evolving basis vectors can be written as $\mathbf{b}_1(t) = \exp(\mathbf{G}t)\,\mathbf{B} \cdot (\mathbf{Z}_4 - \mathbf{Z}_1)$, $\mathbf{b}_2(t) = \exp(\mathbf{G}t)\,\mathbf{B} \cdot (\mathbf{Z}_2 - \mathbf{Z}_1)$. These give

$$\mathbf{b}_1(t) = \exp(\mathbf{G}\,t)\,\mathbf{B} \cdot \begin{pmatrix} 0 \\ 1 \end{pmatrix}$$

$$\mathbf{b}_2(t) = \exp(\mathbf{G}\,t)\,\mathbf{B} \cdot \begin{pmatrix} 1 \\ 0 \end{pmatrix}$$

both of which are obviously independent of the box choice $\{a, b\}$. Hence the definition of relative coordinates given in (2.38) is independent of box choice as $(\mathbf{x}(t) - \mathbf{O}(t))$ is simply a shift of the box origin (or of the choice of box).

2.3 General linear flows

In this section we shall detail the bases for the different types of flows. The basis for shear flow is well known and the basis for two dimensional strain flow, which we have just demonstrated, is detailed in [50]. The basis for combination flow between shear and strain and the combination flow of shear / strain and rotation are new work.

2.3.1 Shear Flow Repeating Basis

Here we shall show the simple case of a repeating basis for a shear flow. This is a simple case which is relatively easy to imagine and quite intuitive, and is

illustrated in figure 2.3.

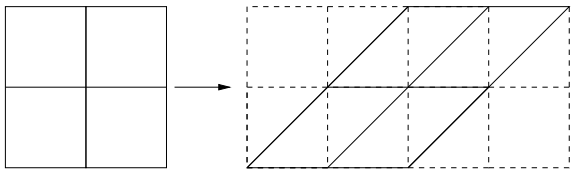

Figure 2.3: Evolution and repetition of box under shear flow

For a shear flow our rate of strain tensor is

$$\mathbf{G} = \begin{pmatrix} 0 & \beta \\ 0 & 0 \end{pmatrix}, \tag{2.39}$$

where β is the shear rate. As previously stated for a basis $\mathbf{B}$ to self-replicate under flow,

$$\mathbf{B} \cdot \mathbf{Z}_1 = \exp[\mathbf{G}T]\, \mathbf{B} \cdot \mathbf{Z}_0, \tag{2.40}$$

where $\mathbf{Z}_i$ are integer vectors at $i = 0$ corresponding to $t = 0$ and $i = 1$ for the value of $\mathbf{Z}$ at a $t = T$. There is an obvious solution to this problem given by

$$\mathbf{B} = \begin{pmatrix} a & 0 \\ 0 & b \end{pmatrix}, \tag{2.41}$$

where $a, b \in \mathbb{R}$. In practice it is more convenient to consider a square lattice

$$\mathbf{B} = \begin{pmatrix} a & 0 \\ 0 & a \end{pmatrix}. \tag{2.42}$$

and the period for self-replication is

$$T = \frac{1}{\beta}, \tag{2.43}$$

so that

$$\begin{aligned} \exp[\mathbf{G}T]\, \mathbf{B} \cdot \mathbf{Z}_0 &= \begin{pmatrix} 1 & \beta T \\ 0 & 1 \end{pmatrix} \begin{pmatrix} a & 0 \\ 0 & a \end{pmatrix} \cdot \mathbf{Z}_0 \\ &= \begin{pmatrix} a & a \\ 0 & a \end{pmatrix} \cdot \mathbf{Z}_0 \\ &= \begin{pmatrix} a & 0 \\ 0 & a \end{pmatrix} \cdot \begin{pmatrix} 1 & 1 \\ 0 & 1 \end{pmatrix} \cdot \mathbf{Z}_0, \end{aligned} \tag{2.44}$$

and

$$\mathbf{Z}_1 = \begin{pmatrix} 1 & 1 \\ 0 & 1 \end{pmatrix} \cdot \mathbf{Z}_0. \tag{2.45}$$

Now that we are equipped with the knowledge that both shear and strain flows have a basis which repeats we can start to consider the possibility of a linear combination of shear and strain flow.

2.3.2 Strain Flow

In this section we give a brief example of how one box evolves under a strain flow and the lattice points repeat, as shown in figure 2.4. In this figure we are using the second basis (and lattice) for plane strain from section 2.2.1:

$$\mathbf{B} = \begin{pmatrix} 1 & (1+\sqrt{5})/2 \\ 1 & (1-\sqrt{5})/2 \end{pmatrix}. \tag{2.46}$$

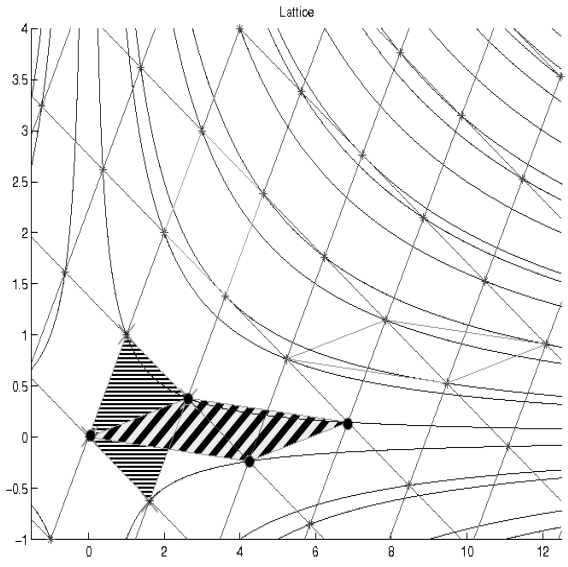

Figure 2.4: Evolution of box and replication of lattice under strain flow

The way in which the lattice repeats itself in this case is less intuitive and certainly hard to imagine without figure 2.4. The curved lines show the evolution of the vertices. The lattice shows the cells or boxes at time $t = 0$. We

are looking at the the box whose left corner is at the origin, filled with narrow horizontal lines, and whose corners are marked by large crosses. The vertices follow the flow lines until they all cross a new set of vertices of the lattice. This is when the basis lattice is said to replicate. The new locations of our four corner vertices are represented by dots, and the stretched box is filled with wide slanted stripes.

Let us label each point of the first basis square 1–4, starting with the corner at the origin and continuing round in a clockwise direction, and follow the path of each vertex. The coordinates of each of these initial points are given by

$$\mathbf{x}_r = \mathbf{B} \cdot \mathbf{Z}_r, \qquad \text{with } r \in \{1, 2, 3, 4\} \tag{2.47}$$

and

$$\mathbf{Z}_1 = \begin{pmatrix} 0 \\ 0 \end{pmatrix} \quad \mathbf{Z}_2 = \begin{pmatrix} 1 \\ 0 \end{pmatrix} \quad \mathbf{Z}_3 = \begin{pmatrix} 1 \\ 1 \end{pmatrix} \quad \mathbf{Z}_4 = \begin{pmatrix} 0 \\ 1 \end{pmatrix} \tag{2.48}$$

From figure 2.4 we can see where our vertices repeat but we do need to confirm that each point repeats in the same time T. The evolution of the points is governed by equation (2.14), $\mathbf{x}(t) = \exp(\mathbf{G}t) \cdot \mathbf{x}(0)$, and hence this is simply a case of solving the four equations ($r = 1 \ldots 4$)

$$\mathbf{B} \cdot \mathbf{Z}'_r = \exp(\mathbf{G}T)\, \mathbf{B} \cdot \mathbf{Z}_r, \tag{2.49}$$

for T, where $\mathbf{Z}'_r$ refers to the repeated integer coordinates (at time T) of the point which originated at $\mathbf{Z}_r$ at time $t = 0$.

If we consider the original box in figure 2.4 and suppose that each of the vertices is transformed to the corresponding corner of the new box in that figure, we are considering

$$\mathbf{Z}'_1 = \begin{pmatrix} 0 \\ 0 \end{pmatrix} \quad \mathbf{Z}'_2 = \begin{pmatrix} 1 \\ 1 \end{pmatrix} \quad \mathbf{Z}'_3 = \begin{pmatrix} 2 \\ 3 \end{pmatrix} \quad \mathbf{Z}'_4 = \begin{pmatrix} 1 \\ 2 \end{pmatrix}. \tag{2.50}$$

These coordinates all agree with the matrix form derived in section 2.2.1:

$$\mathbf{Z}'_r = \mathbf{M} \cdot \mathbf{Z}_r \qquad \text{where} \qquad \mathbf{M} = \begin{pmatrix} 1 & 1 \\ 1 & 2 \end{pmatrix}. \tag{2.51}$$

It only remains to check the four times at which these vertices reach their destination lattice points. Clearly since

$$\mathbf{Z}_1' = \mathbf{Z}_1 = \begin{pmatrix} 0 \\ 0 \end{pmatrix} \tag{2.52}$$

the first point is always at its destination; we only need to check the other three. Indeed, since $\mathbf{Z}_3 = \mathbf{Z}_2 + \mathbf{Z}_4$ and $\mathbf{Z}_3' = \mathbf{Z}_2' + \mathbf{Z}_4'$ and the problem is entirely linear, it is enough to check that vertices 2 and 4 reach their destinations at the same time T.

If we consider the transformation of vertex 2, whose edge from the origin is represented by $\mathbf{b}_1$, then according to equation (2.49) we can arrive at,

$$\mathbf{B} \cdot \begin{pmatrix} 1 \\ 1 \end{pmatrix} = \exp(\mathbf{G}T)\,\mathbf{B} \cdot \begin{pmatrix} 1 \\ 0 \end{pmatrix}, \tag{2.53}$$

and for vertex 4, represented by $\mathbf{b}_2$,

$$\mathbf{B} \cdot \begin{pmatrix} 1 \\ 2 \end{pmatrix} = \exp(\mathbf{G}T)\,\mathbf{B} \cdot \begin{pmatrix} 0 \\ 1 \end{pmatrix}. \tag{2.54}$$

Since

$$\mathbf{G} = \begin{pmatrix} \lambda & 0 \\ 0 & -\lambda \end{pmatrix} \quad \text{and} \quad \exp(\mathbf{G}T) = \begin{pmatrix} e^{\lambda T} & 0 \\ 0 & e^{-\lambda T} \end{pmatrix}, \tag{2.55}$$

for a given basis

$$\mathbf{B} = \begin{pmatrix} b_{1,1} & b_{2,1} \\ b_{1,2} & b_{2,2} \end{pmatrix} \tag{2.56}$$

equations (2.53) and (2.54) give

$$\lambda T = \ln\left(\frac{b_{1,1} + b_{2,1}}{b_{1,1}}\right), \tag{2.57a}$$

$$\lambda T = \ln\left(\frac{b_{1,2}}{b_{1,2} + b_{2,2}}\right), \tag{2.57b}$$

$$\lambda T = \ln\left(\frac{b_{1,1} + 2b_{2,1}}{b_{2,1}}\right), \tag{2.57c}$$

$$\lambda T = \ln\left(\frac{b_{2,2}}{b_{1,2}+2b_{2,2}}\right). \tag{2.57d}$$

So for the box edges to reproduce (i.e the lattice points to map onto new vertices) in the same time, we have the condition

$$\frac{b_{1,1}+b_{2,1}}{b_{1,1}} = \frac{b_{1,2}}{b_{1,2}+b_{2,2}} = \frac{b_{1,1}+2b_{2,1}}{b_{2,1}} = \frac{b_{2,2}}{b_{1,2}+2b_{2,2}} = e^{\lambda T}. \tag{2.58}$$

For our basis

$$\mathbf{B} = \begin{pmatrix} 1 & \frac{1+\sqrt{5}}{2} \\ 1 & \frac{1-\sqrt{5}}{2} \end{pmatrix}, \tag{2.59}$$

this is satisfied with a value of $e^{\lambda T} = \frac{3+\sqrt{5}}{2}$, which was our value of S when we were deriving our basis vectors. This gives us a repeat time of

$$\lambda T = \ln\left(\frac{3+\sqrt{5}}{2}\right) \tag{2.60}$$

as shown in section 2.2.1.

2.3.3 Conditions For a Repeating Basis With a Combination of Shear and Strain Flow

In section 2.2.1 we derived a self-replicating basis for a strain flow. We have also showed the more trivial solution of a repeating basis for a shear flow. Here we will consider the combination of a strain and shear flow.

The method used in section 2.2.1 is repeated to derive the repeating basis. Let us consider the velocity to be given by

$$\mathbf{U} = \mathbf{G} \cdot \mathbf{x}, \tag{2.61}$$

with

$$\mathbf{G} = (1-\gamma)\begin{pmatrix} \alpha & 0 \\ 0 & -\alpha \end{pmatrix} + \gamma\begin{pmatrix} 0 & \beta \\ 0 & 0 \end{pmatrix}, \tag{2.62}$$

with γ, α and β all real variables.

We can set $\alpha = \beta = 1$ without loss of generality, since these two variables only affect the flow strength, not the flow type. Integrating this yields,

$$\mathbf{x} = \exp\left[\begin{pmatrix} (1-\gamma) & \gamma \\ 0 & -(1-\gamma) \end{pmatrix} t\right] \cdot \mathbf{x}_0. \tag{2.63}$$

The exponential above can be calculated: setting

$$\mathbf{G}_1 = \begin{pmatrix} 1 & 0 \\ 0 & -1 \end{pmatrix} \qquad \mathbf{G}_2 = \begin{pmatrix} 0 & 1 \\ 0 & 0 \end{pmatrix} \tag{2.64}$$

we have

$$\mathbf{G} = \begin{pmatrix} (1-\gamma) & \gamma \\ 0 & -(1-\gamma) \end{pmatrix} = (1-\gamma)\mathbf{G}_1 + \gamma\mathbf{G}_2. \tag{2.65}$$

Noting that

$$\mathbf{G}_1^m = \begin{pmatrix} 1 & 0 \\ 0 & (-1)^m \end{pmatrix} \qquad \mathbf{G}_2^2 = \begin{pmatrix} 0 & 0 \\ 0 & 0 \end{pmatrix}, \tag{2.66}$$

we can deduce

$$\begin{aligned} \mathbf{G}^n &= \sum_{j=0}^{n} \binom{n}{j} [(1-\gamma)\mathbf{G}_1]^{n-j} [\gamma\mathbf{G}_2]^j \\ &= (1-\gamma)^n \mathbf{G}_1^n + n(1-\gamma)^{n-1}\mathbf{G}_1^{n-1}\gamma\mathbf{G}_2 \quad \text{for } n \geq 1 \end{aligned} \tag{2.67}$$

$$
\begin{aligned}
\exp\left[\mathbf{G}t\right] &= \sum_{n=0}^{\infty} \frac{\mathbf{G}^n t^n}{n!} \\
&= \mathbf{I} + \sum_{n=1}^{\infty} \frac{[(1-\gamma)^n \mathbf{G}_1^n + n(1-\gamma)^{n-1}\mathbf{G}_1^{n-1}\gamma\mathbf{G}_2]t^n}{n!} \\
&= \sum_{n=0}^{\infty} \frac{(1-\gamma)^n \mathbf{G}_1^n t^n}{n!} + \sum_{n=1}^{\infty} \frac{(1-\gamma)^{n-1}\mathbf{G}_1^{n-1}t^{n-1}}{(n-1)!}\gamma t\mathbf{G}_2 \\
&= \begin{pmatrix} \exp\left[(1-\gamma)t\right] & 0 \\ 0 & \exp\left[-(1-\gamma)t\right] \end{pmatrix} \\
&\quad + \begin{pmatrix} \exp\left[(1-\gamma)t\right] & 0 \\ 0 & \exp\left[-(1-\gamma)t\right] \end{pmatrix} \begin{pmatrix} 0 & \gamma t \\ 0 & 0 \end{pmatrix} \\
&= \begin{pmatrix} \exp\left[(1-\gamma)t\right] & \gamma t \exp\left[(1-\gamma)t\right] \\ 0 & \exp\left[-(1-\gamma)t\right] \end{pmatrix}
\end{aligned}
\tag{2.68}
$$

Then equation (2.63) can be rewritten as

$$
\mathbf{x} = \mathbf{S} \cdot \mathbf{x}_0 = \begin{pmatrix} S & n \\ 0 & S^{-1} \end{pmatrix} \cdot \mathbf{x}_0, \tag{2.69}
$$

with $S = \exp\left[(1-\gamma)t\right]$ and $n = S\gamma t$.

We have to construct a basis such that at some time $t = T$

$$
\mathbf{S}\,\mathbf{B} = \mathbf{B}\,\mathbf{M}, \tag{2.70}
$$

where $\mathbf{M}$ has solely integer components,

which yields:

$$
\begin{pmatrix} S & n \\ 0 & S^{-1} \end{pmatrix} \mathbf{B} = \mathbf{B}\,\mathbf{M}. \tag{2.71}
$$

The basis matrix $\mathbf{B}$ can be written as

$$
\mathbf{B} = \begin{pmatrix} A\cos\theta_1 & \cos\theta_2 \\ A\sin\theta_1 & \sin\theta_2 \end{pmatrix}, \tag{2.72}
$$

and at some point of the evolution of the basis under the flow, the basis vectors will be perpendicular to each other which allows us to say $\theta_1 = \theta_2 + \frac{\pi}{2}$ resulting in the simpler

$$\mathbf{B} = \begin{pmatrix} -A\sin\theta_2 & \cos\theta_2 \\ A\cos\theta_2 & \sin\theta_2 \end{pmatrix} = \begin{pmatrix} -A\,a & b \\ A\,b & a \end{pmatrix}, \tag{2.73}$$

in which we have defined $a = \sin\theta_2$ and $b = \cos\theta_2$ for conciseness. The equality shown in equation (2.71) has two invariants,

1. $\det(\mathbf{M}) = M_{11}\,M_{22} - M_{12}\,M_{21} = \det(\mathbf{S}) = 1$
2. $\mathrm{Tr}(\mathbf{M}) = M_{11} + M_{22} = S + S^{-1} = \mathrm{Tr}(\mathbf{S})$.

The problem of finding a basis has several steps, the first being relating S and n to $\mathbf{M}$ in equation (2.71). Simply multiplying our matrices together gives us

$$\begin{pmatrix} A(nb - Sa) & Sb + na \\ AS^{-1}b & S^{-1}a \end{pmatrix} = \begin{pmatrix} -AaM_{11} + bM_{21} & -AaM_{12} + bM_{22} \\ AbM_{11} + aM_{21} & AbM_{12} + aM_{22} \end{pmatrix}. \tag{2.74}$$

We can easily rearrange the four component equations of (2.74) to give,

$$\frac{a}{b} = \frac{M_{21} - A\,n}{A\,(M_{11} - S)} \qquad \frac{a}{b} = \frac{M_{22} - S}{n + A\,M_{12}} \tag{2.75}$$

$$\frac{a}{b} = \frac{A\,(S^{-1} - M_{11})}{M_{21}} \qquad \frac{a}{b} = \frac{A\,M_{12}}{S^{-1} - M_{22}}. \tag{2.76}$$

If we add the two equations of (2.75) we get

$$2\left(\frac{a}{b}\right) = \frac{(M_{21} - A\,n)(n + A\,M_{12}) + A\,(M_{11} - S)(M_{22} - S)}{A(M_{11} - S)(n + A\,M_{12})}, \tag{2.77}$$

which by use of both invariants gives

$$2\left(\frac{a}{b}\right) = \frac{(M_{21} - A\,n)(n + A\,M_{12}) + A\,M_{12}\,M_{21}}{A(M_{11} - S)(n + A\,M_{12})}. \tag{2.78}$$

Using the same method with the two equations of (2.76) we get

$$2\left(\frac{a}{b}\right) = \frac{A(S^{-1} - M_{11})(S^{-1} - M_{22}) + A\,M_{12}\,M_{21}}{M_{12}(S^{-1} - M_{22})} = \frac{2\,A\,M_{12}}{(M_{11} - S)}. \tag{2.79}$$

Finally, eliminating a/b from equations (2.78) and (2.79) and simplifying gives us

$$-2\,M_{12}^2\,A^3 - 3\,n\,M_{12}\,A^2 + (2\,M_{12}\,M_{21} - n^2)A + n\,M_{21} = 0. \tag{2.80}$$

Solving this equation for A yields the solutions

$$A_1 = -\frac{n}{2\,M_{12}} \qquad\qquad A_{2,3} = \frac{-n \pm \sqrt{4\,M_{12}\,M_{21} + n^2}}{2\,M_{12}}. \tag{2.81}$$

The second invariant (the trace) gives us the quadratic equation $S^2 - (M_{11} + M_{22})\,S + 1 = 0$ resulting in the solution

$$S = \frac{(M_{11} + M_{22}) \pm \sqrt{(M_{11} + M_{22})^2 - 4}}{2}. \tag{2.82}$$

Now that we know A and S, from any one of the equations in equations (2.75) and (2.76) we have an expression for $\tan\theta_2$ and hence can find an expression for $\sin\theta_2$ and $\cos\theta_2$ in terms of M_{ij} and n.

This leaves us only with the problem of finding a matrix $\mathbf{M}$ that satisfies our equations. As long as we can satisfy all four of the equations (2.75)–(2.76), with an A and S that depend on $\mathbf{M}$ and n, we shall have a valid solution. We have already shown that when we calculated a basis for a strain flow the matrix

$$\mathbf{M} = \begin{pmatrix} 1 & 1 \\ 1 & 2 \end{pmatrix} \tag{2.83}$$

was a valid choice: we shall use this again. Substituting these values into equations (2.81) and (2.82) we arrive at the values for S and A being (taking the second solution for A and the positive square root for S)

$$S = \frac{3 + \sqrt{5}}{2}, \tag{2.84}$$

and

$$A = \frac{-n + \sqrt{n^2 + 4}}{2}. \tag{2.85}$$

Equations (2.75)–(2.76) are then satisfied providing

$$\frac{a}{b} = \frac{(1 - \sqrt{5})(-n + \sqrt{n^2 + 4})}{4}. \tag{2.86}$$

This then allows us to find our general basis $\mathbf{B}$ for a combined shear and strain flow:

$$\mathbf{B} = k \begin{pmatrix} (\sqrt{5} - 1)(-n + \sqrt{n^2 + 4}) & -2(n + \sqrt{n^2 + 4}) \\ 4 & 2(1 - \sqrt{5}) \end{pmatrix}, \tag{2.87}$$

for some normalisation constant k (for which any real value is allowed).

We could have chosen any of the solutions of S and A and still had a valid solution but choosing positive results helps to avoid confusion by keeping basis vectors pointing in their expected directions. If we take the example of $n = 1$ this results in $A = \frac{\sqrt{5}-1}{2}$ and a basis

$$\mathbf{B} = 2k \begin{pmatrix} 3 - \sqrt{5} & -(1 + \sqrt{5}) \\ 2 & (1 - \sqrt{5}) \end{pmatrix}. \tag{2.88}$$

This method is valid for a pure strain flow, and any combination of shear and strain flow. However, it is not valid for a shear flow, because in the shear case $\mathbf{G}$ does not diagonalise. In the case of a pure shear flow $n \to \infty$. This in turn implies that

$$[\mathbf{b}_2]_1 = -2k(n + \sqrt{n^2 + 4}) \sim -2k \left[2\,n + \frac{2}{n} + O\left(n^{-3}\right) \right] \to \infty \tag{2.89}$$

and hence our basis no longer consists of finite vectors.

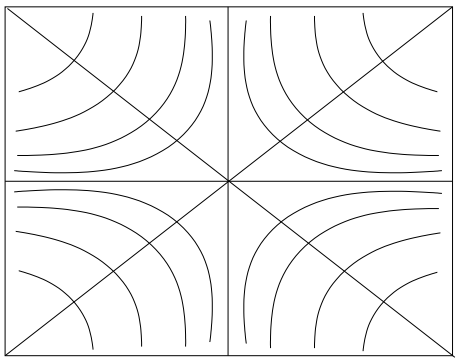

Figure 2.5: Strain flow

2.3.4 A Repeating Basis with a Combination of Strain Flow and Rotation

The addition of rotation to our combination of flows means that we are now considering all possible linear two dimensional flows.

In this next section we will concentrate on finding a basis which is periodic under a flow between strain and rotation. The method used to find this truly general repeating basis can be easily simplified for finding a specific solution such as a pure strain basis.

Any two-dimensional linear flow can be split into a combination of strain and rotation. This is fully explained and proved in section 2.3.5. The matrix which describes this is:

$$\mathbf{G} = \begin{pmatrix} (1-\beta) & \beta \\ -\beta & -(1-\beta) \end{pmatrix}, \tag{2.90}$$

with $\beta \in [0,1]$. A few sample values:

$\beta = 0$	Strain	Figure 2.5
$\beta = \frac{1}{2}$	Shear parallel to the $y = -x$ line	Figure 2.6
$\beta = 1$	Pure rotation.	Figure 2.7.

The problem of finding the repeating basis, as before in equation (2.70), is that of constructing a basis such that

$$\mathbf{S}\,\mathbf{B} = \mathbf{B}\,\mathbf{M}, \tag{2.91}$$

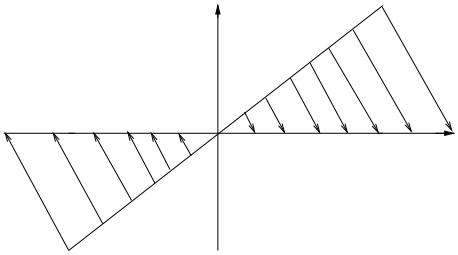

Figure 2.6: Shear flow

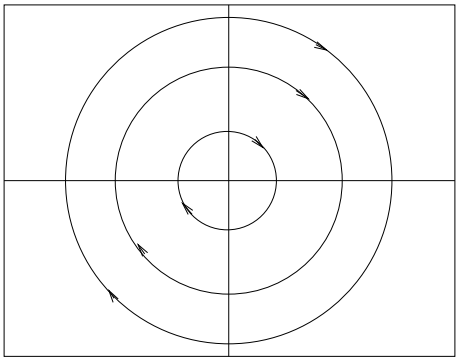

Figure 2.7: Rotation flow

where $\mathbf{M}$ has solely integer components and $\mathbf{B}$ is the basis matrix. The $\mathbf{S}$ matrix is defined as being

$$\mathbf{S} = \exp(\mathbf{G}T) \tag{2.92}$$

where T is the time at which the lattice self-replicates and $\mathbf{G}$ is the rate of strain tensor which causes the background flow

$$\mathbf{U} = \mathbf{G} \cdot \mathbf{x}. \tag{2.93}$$

In section 2.3.5 we will show that this matrix $\mathbf{G}$ is sufficiently general to capture the dynamics of all two-dimensional linear flows that satisfy mass conservation. With previous flow combinations we diagonalised $\mathbf{G}$ by saying

$$\mathbf{G} = \mathbf{V}\,\mathbf{\Lambda}\,\mathbf{V}^{-1}, \tag{2.94}$$

where the columns of $\mathbf{V}$ are the right eigenvectors of $\mathbf{G}$, and effectively rotated

the underlying axes so that we could say

$$\mathbf{S} = \exp\left[\mathbf{\Lambda} T\right]. \tag{2.95}$$

With the addition of rotation the eigenvalues and eigenvectors become complex. This means that we cannot just rotate our axes and remove the $\mathbf{V}$ matrices. Hence our new form of $\mathbf{S}$ becomes

$$\mathbf{S} = \mathbf{V}\, \exp\left[\mathbf{\Lambda} T\right] \mathbf{V}^{-1}. \tag{2.96}$$

The problem of solving equation (2.91) is the same but has increased in complexity because $\mathbf{S}$ is no longer diagonal. We can rearrange the equality to

$$\exp\left[\mathbf{\Lambda} T\right] \left[\mathbf{V}^{-1}\, \mathbf{B}\right] = \left[\mathbf{V}^{-1}\, \mathbf{B}\right] \mathbf{M}, \tag{2.97}$$

with

$$\exp\left[\mathbf{\Lambda} T\right] = \begin{pmatrix} e^{\alpha T} & 0 \\ 0 & e^{-\alpha T} \end{pmatrix}, \tag{2.98}$$

$$\mathbf{V} = \begin{pmatrix} -1+\beta-\alpha & -1+\beta+\alpha \\ \beta & \beta \end{pmatrix}, \tag{2.99}$$

$$\mathbf{V}^{-1} = \frac{-1}{2\alpha\beta} \begin{pmatrix} \beta & 1-\beta-\alpha \\ -\beta & -1+\beta-\alpha \end{pmatrix}, \tag{2.100}$$

and $\alpha = \sqrt{1-2\beta}$, which will be imaginary if $\beta > 1/2$.
In considering the problem of solving

$$\exp[\mathbf{\Lambda} T] \left[\mathbf{V}^{-1}\, \mathbf{B}\right] = \left[\mathbf{V}^{-1}\, \mathbf{B}\right] \mathbf{M}, \tag{2.101}$$

we shall look at each matrix element in turn. Letting

$$\mathbf{W} = \mathbf{V}^{-1}\, \mathbf{B}, \qquad \mathbf{B} = \begin{pmatrix} -As & c \\ Ac & s \end{pmatrix}, \tag{2.102}$$

$s = \sin\theta$ and $c = \cos\theta$ allows our problem to be written

$$\exp\left[\mathbf{\Lambda} T\right] \mathbf{W} = \mathbf{W}\, \mathbf{M} \tag{2.103}$$

with

$$\mathbf{W} = \frac{1}{2\alpha\beta}\begin{pmatrix} A[c(\alpha-1+\beta)+s\beta] & s(\alpha-1+\beta)-c\beta \\ A[c(\alpha+1-\beta)-s\beta] & s(\alpha+1-\beta)+c\beta \end{pmatrix}. \tag{2.104}$$

Substituting into the left hand side of equation (2.103)

$$\exp[\mathbf{\Lambda}T]\,\mathbf{W} = \begin{pmatrix} W_{11}e^{\alpha T} & W_{12}e^{\alpha T} \\ W_{21}e^{-\alpha T} & W_{22}e^{-\alpha T} \end{pmatrix}, \tag{2.105}$$

and right hand side

$$\mathbf{W}\,\mathbf{M} = \begin{pmatrix} W_{11}M_{11}+W_{12}M_{21} & W_{11}M_{12}+W_{12}M_{22} \\ W_{21}M_{11}+W_{22}M_{21} & W_{21}M_{12}+W_{22}M_{22} \end{pmatrix}. \tag{2.106}$$

Now equating components

$$\begin{array}{ll} [11]: & W_{11}(e^{\alpha T}-M_{11}) = W_{12}M_{21} \\ [12]: & W_{12}(e^{\alpha T}-M_{22}) = W_{11}M_{12} \\ [21]: & W_{21}(e^{-\alpha T}-M_{11}) = W_{22}M_{21} \\ [22]: & W_{22}(e^{-\alpha T}-M_{22}) = W_{21}M_{12} \end{array} \tag{2.107}$$

where [11], [12] etc. refer to the matrix components of $\mathbf{W}\,\mathbf{M}$. We find

$$\frac{W_{11}}{W_{12}} = \frac{e^{\alpha T}-M_{22}}{M_{12}} = \frac{M_{21}}{e^{\alpha T}-M_{11}} = K, \tag{2.108}$$

and

$$\frac{W_{21}}{W_{22}} = \frac{e^{-\alpha T}-M_{22}}{M_{12}} = \frac{M_{21}}{e^{-\alpha T}-M_{11}} = K', \tag{2.109}$$

where $K' = \bar{K}$, the complex conjugate of K, if $\beta > 1/2$ so that α is imaginary. Now since $\det(\exp[\mathbf{\Lambda}T]) = 1$, equation (2.103) implies $\det(\mathbf{M}) = 1$. If we substitute $x = e^{\alpha T}$ into either of equations (2.108) or (2.109) and use this fact, we have the quadratic equation

$$x^2 - (M_{11}+M_{22})x + 1 = 0, \tag{2.110}$$

with solution

$$e^{\alpha T} = \frac{(M_{11}+M_{22}) \pm \sqrt{(M_{11}+M_{22})^2-4}}{2}. \tag{2.111}$$

We now specify to the case where $\beta > \frac{1}{2}$ in equation (2.90), in which case α is imaginary. The simplest solution is for $\mathbf{M} = -\mathbf{I}$, giving

$$T = \frac{i\pi}{\alpha}. \tag{2.112}$$

Having an expression for T and a value for $\mathbf{M}$ makes finding the repeating basis a lot easier. For the case where $\frac{1}{2} < \beta \leq 1$, equation (2.103) becomes simply $-\mathbf{W} = -\mathbf{W}$ and our choice of basis is free. We shall therefore choose

$$\mathbf{B} = \mathbf{I}. \tag{2.113}$$

For the case where $0 \leq \beta < \frac{1}{2}$, α is real and the calculation needs to be continued. Substituting the form of $\mathbf{W}$ into the components of equation (2.107):

$$\begin{array}{ll}
[11]: & A[c(\alpha-1+\beta)+s\beta](e^{\alpha T}-M_{11}) = [s(\alpha-1+\beta)-c\beta]M_{21}, \\
[12]: & [s(\alpha-1+\beta)-c\beta](e^{\alpha T}-M_{22}) = A[c(\alpha-1+\beta)+s\beta]M_{12}, \\
[21]: & A[c(\alpha+1-\beta)-s\beta](e^{-\alpha T}-M_{11}) = [s(\alpha+1-\beta)+c\beta]M_{21}, \\
[22]: & [s(\alpha+1-\beta)+c\beta](e^{-\alpha T}-M_{22}) = A[c(\alpha+1-\beta)-s\beta]M_{12}.
\end{array} \tag{2.114}$$

Taking the components of equation (2.114) in turn,

$$\tan\theta = \frac{A(\alpha-1+\beta)(e^{\alpha T}-M_{11})+\beta M_{21}}{-A\beta(e^{\alpha T}-M_{11})+(\alpha-1+\beta)M_{21}}, \tag{2.115}$$

$$\tan\theta = \frac{A(\alpha-1+\beta)M_{12}+\beta(e^{\alpha T}-M_{22})}{(\alpha-1+\beta)(e^{\alpha T}-M_{22})-A\beta M_{12}}, \tag{2.116}$$

$$\tan\theta = \frac{A(\alpha+1-\beta)(e^{-\alpha T}-M_{11})-\beta M_{21}}{A\beta(e^{-\alpha T}-M_{11})+(\alpha+1-\beta)M_{21}}, \tag{2.117}$$

$$\tan\theta = \frac{A(\alpha+1-\beta)M_{12}-\beta(e^{-\alpha T}-M_{22})}{(\alpha+1-\beta)(e^{-\alpha T}-M_{22})+A\beta M_{12}}. \tag{2.118}$$

Using equations (2.108) and (2.109) to re-express $e^{\alpha T}$ and $e^{-\alpha T}$, these four equations become

$$\tan\theta = \frac{A(\alpha-1+\beta)+\beta K}{(\alpha-1+\beta)K-A\beta} = \frac{A(\alpha+1-\beta)-\beta K'}{(\alpha+1-\beta)K'+A\beta}. \tag{2.119}$$

Equation (2.119) results in

$$\alpha A^2 + \beta(K-K')A + \alpha K K' = 0. \tag{2.120}$$

Solving for A gives

$$A = \frac{-\beta(K-K') \pm \sqrt{\beta^2(K-K')^2 - 4\alpha^2 KK'}}{2\alpha}. \tag{2.121}$$

The case $\beta \in [0, \frac{1}{2})$ is equivalent to the one we solved in section 2.3.3, so we can allow $\mathbf{M}$ to be of its previous form

$$\mathbf{M} = \begin{pmatrix} 1 & 1 \\ 1 & 2 \end{pmatrix}. \tag{2.122}$$

Substituting this value of $\mathbf{M}$ into equations (2.108), (2.109) and (2.111) gives

$$e^{\alpha T} = \frac{3+\sqrt{5}}{2}, \qquad e^{-\alpha T} = \frac{3-\sqrt{5}}{2}, \tag{2.123}$$

in which we have taken (conventionally) the positive square root in solving for $e^{\alpha T}$ so that $T > 0$, and

$$K = \frac{\sqrt{5}-1}{2}, \qquad K' = \frac{-\sqrt{5}-1}{2}. \tag{2.124}$$

Substituting these values into equation (2.121),

$$A = \frac{-\sqrt{5}\beta \pm \sqrt{5\beta^2 + 4\alpha^2}}{2\alpha} = \frac{-\sqrt{5}\beta \pm \sqrt{5\beta^2 - 8\beta + 4}}{2\alpha}. \tag{2.125}$$

and, in turn,

$$\tan\theta = \frac{(-\sqrt{5}\beta \pm \sqrt{5\beta^2 - 8\beta + 4})(\alpha - 1 + \beta)(1+\sqrt{5}) + 4\alpha\beta}{-(-\sqrt{5}\beta \pm \sqrt{5\beta^2 - 8\beta + 4})\beta(1+\sqrt{5}) + 4\alpha(\alpha - 1 + \beta)}, \tag{2.126}$$

with $\alpha = \sqrt{1-2\beta}$.

We have found one basis for $0 \le \beta < \frac{1}{2}$ and one for $\frac{1}{2} < \beta \le 1$. The only remaining case is shear flow, $\beta = \frac{1}{2}$, for which a suitable basis is

$$\mathbf{B} = \begin{pmatrix} 1 & 1 \\ 1 & -1 \end{pmatrix}. \tag{2.127}$$

This is equivalent to the basis given in section 2.3.1, with a rotated frame of reference.

In table 2.1 we resent a table of the aspect ratios and repeat time periods of basis for various flows.

β	Aspect ratio	Tepeat time T
0.1	1.13	1.076
0.3	1.66	1.52
0.45	3.47	3.04
0.55	1.0	9.93
0.7	1.0	4.97

Table 2.1: Aspect ratio (at the moment where the basis vectors are at right angles) and repeat time for our basis at different values of β. For $\beta < 0.5$, the resetting matrix is $\mathbf{M} = \begin{pmatrix} 1 & 1 \\ 1 & 2 \end{pmatrix}$; for $\beta > 0.5$, $\mathbf{M} = \mathbf{I}$.

2.3.5 Completeness of Basis for All Flows

In section 2.3.4 it was shown that a basis could be found for any combination of shear, strain and rotation. We claimed that the matrix $\mathbf{G}$ given in equation (2.90) covers all linear incompressible two dimensional flows. In the following section we shall prove that equation (2.90) is indeed sufficient with $\beta \in [0, 1]$. If we consider a completely general incompressible flow we have the velocity gradient matrix

$$\mathbf{G} = \begin{pmatrix} a & b \\ c & -a \end{pmatrix}, \tag{2.128}$$

which has zero trace due to the $\nabla \cdot \mathbf{U} = 0$ mass conservation condition. We shall first show that under a rotation θ of the underlying axes we can produce a matrix of the form,

$$\mathbf{G} = \begin{pmatrix} P & Q \\ -Q & -P \end{pmatrix}, \tag{2.129}$$

and eventually of the form

$$\mathbf{G} = \begin{pmatrix} (1-\beta) & \beta \\ -\beta & -(1-\beta) \end{pmatrix}. \tag{2.130}$$

We will use the rotation matrices

$$\mathbf{R} = \begin{pmatrix} \cos\theta & \sin\theta \\ -\sin\theta & \cos\theta, \end{pmatrix} \tag{2.131}$$

$$\mathbf{R}^{-1} = \begin{pmatrix} \cos\theta & -\sin\theta \\ \sin\theta & \cos\theta. \end{pmatrix}. \tag{2.132}$$

Rotating the underlying axes on which we view the velocity gradient matrix (2.128) by using the rotation matrices (2.131) and (2.132) gives us a new $\mathbf{G}$, given by

$$\begin{aligned} \mathbf{G}_{\text{rotated}} &= \mathbf{R}^{-1}\,\mathbf{G}\,\mathbf{R} \\ &= \begin{pmatrix} a(2C^2-1)-(b+c)SC & (b+c)C^2-c+2aSC \\ (b+c)C^2-b+2aSC & a(1-2C^2)+(b+c)SC \end{pmatrix}, \end{aligned} \tag{2.133}$$

in which we have written $S = \sin\theta$ and $C = \cos\theta$ for conciseness.

The mass conservation condition requires that $\mathbf{G}$ has zero trace; this condition still holds true in equation (2.133) which is a good quick check.

We wish to make $\mathbf{G}_{\text{rotated}}$ antisymmetric to attain the form of equation (2.129), so we set

$$(b+c)C^2 - c + 2aSC = -[(b+c)C^2 - b + 2aSC] \tag{2.134}$$

and solve for θ. This rapidly gives

$$(b+c)(2C^2-1) + 4aSC = 0 \qquad (b+c)\cos 2\theta + 2a\sin 2\theta = 0 \tag{2.135}$$

Solving for θ:

$$\tan 2\theta = -\frac{b+c}{2a}, \tag{2.136}$$

proving that it is possible to take any flow and by a rotation of axes have a flow of the form (2.129):

$$\mathbf{G}_{\text{rotated}} = \begin{pmatrix} P & Q \\ -Q & -P \end{pmatrix}, \tag{2.137}$$

where in this case

$$P = \frac{\cos 2\theta}{4a}(4a^2 + (b+c)^2) \quad \text{and} \quad Q = \frac{1}{2}(b-c). \tag{2.138}$$

Defining $\beta = Q/(P+Q)$, equation (2.129) becomes

$$\mathbf{G} = (P+Q)\begin{pmatrix} 1-\beta & \beta \\ -\beta & -(1-\beta) \end{pmatrix}, \tag{2.139}$$

which is the same as equation (2.90) with a multiplying factor. The multiplying factor does not affect the type of flow but merely its speed. Hence we can say that (2.90) encompasses all linear two dimensional incompressible flows.

Sufficiency of the Case $\beta \in [0,1]$ to Cover All Flows

So far in this section we have shown that equation (2.90) represents all possible linear two dimensional incompressible flows, provided we allow the parameter β to take any value. In section 2.3.3 we showed that a repeating basis exists for any combination of shear, strain and rotation, i.e. any value $\beta \in [0,1]$. The following section shows that when we consider flows where $\beta < 0$ or $\beta > 1$, this is also covered by equation (2.90) with $0 \leq \beta \leq 1$.

Take the flow gradient matrix of equation (2.130):

$$\mathbf{G} = \begin{pmatrix} (1-\beta) & \beta \\ -\beta & -(1-\beta) \end{pmatrix}, \tag{2.140}$$

and the rotation of axes matrix of equation (2.131)

$$\mathbf{R} = \begin{pmatrix} \cos\theta & \sin\theta \\ -\sin\theta & \cos\theta \end{pmatrix}. \tag{2.141}$$

Letting $\theta = -\frac{\pi}{2}$ and rotating the underlying axes,

$$\begin{aligned} \mathbf{G}_{\text{rotated}} &= \mathbf{R}^{-1}\,\mathbf{G}\,\mathbf{R} \\ &= \begin{pmatrix} -(1-\beta) & \beta \\ -\beta & (1-\beta) \end{pmatrix}. \end{aligned} \tag{2.142}$$

Removing a factor of $2\beta - 1$ gives

$$\mathbf{G}_{\text{rotated}} = (2\beta-1)\begin{pmatrix} -(1-\beta)/(2\beta-1) & \beta/(2\beta-1) \\ -\beta/(2\beta-1) & (1-\beta)/(2\beta-1) \end{pmatrix}, \tag{2.143}$$

and letting $\alpha = \beta/(2\beta-1)$,

$$\mathbf{G}_{\text{rotated}} = (2\beta-1)\begin{pmatrix} (1-\alpha) & \alpha \\ -\alpha & -(1-\alpha) \end{pmatrix}. \tag{2.144}$$

This fits the flow we have already studied in equation (2.90), apart from a factor $2\beta - 1$ which merely changes the flow strength, provided $\alpha \in [0, 1]$. If $\beta > 1$ then $\frac{1}{2} < \alpha < 1$, which is between shear and rotation; if $\beta < 0$ then $0 < \alpha < \frac{1}{2}$, lying between strain and shear.

It follows that linear incompressible flows described by equation (2.90) with β outside the range $[0, 1]$ are also described by $\beta \in [0, 1]$ after rotation of the axes and removal of a multiplicative factor $(2\beta - 1)$ which does not affect the type of flow but only its speed. Hence we can say that equation (2.90) with $\beta \in [0, 1]$ encompasses all linear incompressible two-dimensional flows.

Chapter 3

Computational Results for Smooth Spheres

3.1 Introduction

In section 1.3 we introduced the numerical method of Stokesian Dynamics for simulating a system of solid spheres immersed in a viscous Newtonian fluid. In chapter 2 we showed how to implement a self-replicating lattice for any two-dimensional linear flow field. In this chapter we draw the two together, and carry out simulations of a suspension moving under the action of a variety of linear flow fields.

We will restrict our attention to a monolayer of spheres: that is, all the centres of our spheres lie in a single plane, which is the plane of the two-dimensional linear flow field. This simplification greatly reduces the computational cost of the simulations, but since the flow acts within the plane it is not expected to make a big difference to the physics of the flow. Because our spheres are a single layer in an infinite volume of fluid, the total volume concentration is essentially zero; we use instead the area concentration c in the plane of the sphere centres. This should not be confused with a truly two-dimensional simulation of circles in a plane; these are real, physical spheres which just lie

in one plane of our volume of fluid, and their hydrodynamic interactions are those of spheres not cylinders.

When normalising the extra stress caused by the particles to extract the suspension's rheology, again it does not make sense to use the whole volume of space (we would simply regain the viscosity of the suspending fluid). Instead we normalise over a volume consisting of the area within our plane, and a perpendicular distance $2a$ out of plane (where the particles have radius a). This follows the convention used by Brady & Bossis [10], and has the effect that the Einstein viscosity for dilute suspensions becomes $\mu(1 + \frac{5}{3})c$.

We use a lattice of cells, repeated periodically throughout space. For ease of implementation, we do not account properly for all two-body interactions through all of space; instead when consider the interaction between particle α and particle β we look for the image of particle β which is closest to particle α (looking only in the same repeating cell and the eight which surround it) and use all pairwise interactions based on that image. We will return to this simplification in appendix A and discuss how it may be avoided through Ewald summation.

Our lattice is defined using the self-replicating basis we derived for each flow in chapter 2, and we place n identical spherical particles of radius a in each lattice cell. To achieve the desired area concentration, we simply scale up the lengths of the two basis vectors.

Within this chapter, we will first describe the procedure for arranging the particles randomly within the periodic cell (section 3.2). We then discuss how to extract the rheology of the system from the total stress tensor in section 3.3.2, before beginning to report our numerical results.

In the numerical study, we will report first on the short-time rheology of the system; that is, the stress response to an instantaneous imposition of flow, under which the particles have no time to evolve a microstructure. For these runs, which are not computationally intensive, we use $n = 300$ particles. We will show these short-time results in section 3.4. Next, in section 3.5, we show

the evolution of the system rheology as the particles build up microstructure under flow, using a much smaller system of $n = 30$ particles. In section 3.6.1 we study a single set of physical parameters, for various different values of n in order to assess the severity of this reduction of box size.

3.1.1 Validation

There are several levels of validation of the Stokesian Dynamics code. The original code I inherited was tested against Brady's original 1987 paper [21] via replication of figure 5, see figure 3.1.
The core code has been validated however the addition of different background flows can not be validated as it has not been done before. There are however many checks in the code some of which are mentioned in section 3.2.1.

3.2 Random Seeding of Boxes

In order to simulate a disordered suspension, we need to seed the particles randomly within our starting box. Starting with different random initial positions allows several runs to be done, and averaged, to achieve a more representative value of any output quantity. We have at our disposal three methods of randomly filling our boxes, which are valid in different cases depending on the packing density. All methods take as input one random number (the seed), the lengths of the basis vectors, $L_1 = |\mathbf{b}_1|$ and $L_2 = |\mathbf{b}_2|$ and the number of particles n. We make all lengths dimensionless using the particle radius a. The scaling factor to determine the area created by the basis vectors is initially determined to give a desired area concentration with a set number of particles n of unit radius. These methods are,

Zinchenko method. A method that works for all concentrations of particles. The method is to produce a roughly square grid within the cell (whose sides are of length L_1 and L_2). Particles are placed on each node of

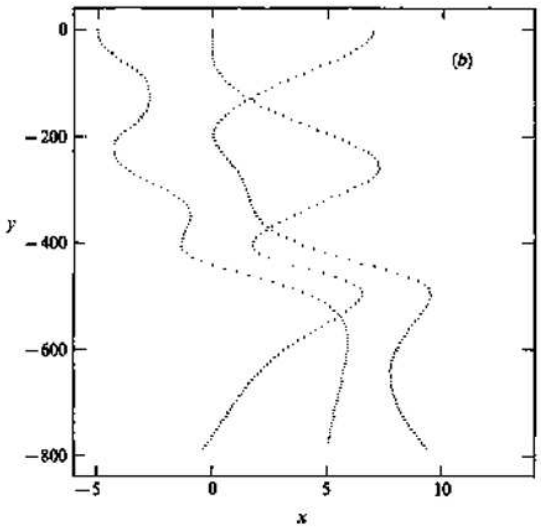

(a) Original plot from [21]

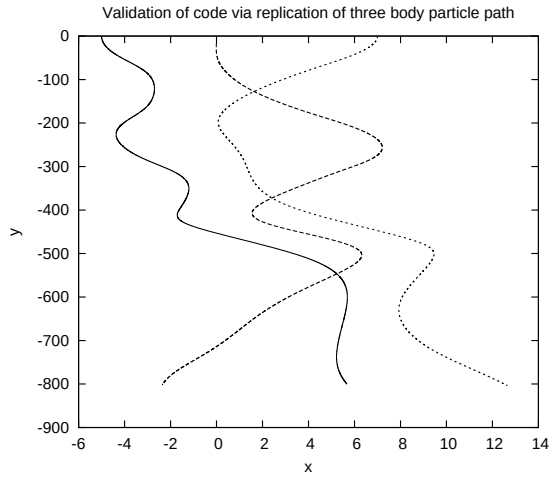

(b) Replicated plot using model

Figure 3.1: Three spheres falling under gravity, validation of core Stokesian Dynamics code comparison to Brady's paper [21]

the grid. Then some particles are removed, at random, until the correct number are present. Finally the particles are then thermally "jiggled" to move them off the grid-like pattern they still hold. For this to work well, the grid should not be full just before the "jiggling" stage: that is, the number of particles $n \neq m \times \text{int}(mL_2/L_1)$ for any integer m, where

n is the number of particles.

Brady low density method. This method is closer to being truly random. The routine randomly places a particle within the box then places another and checks that they do not overlap: if they do, it replaces the particle. This process repeats until sufficient particles have been placed. If, before this happens, a place for a particle cannot be found, the seeding fails. The method works well for low values of c but for high values of c it is more likely to fail. Unfortunately this makes it an unreliable method for all but low concentrations.

Brady high density method. This method is more reliable at high area concentrations than the Brady low density method, as it randomly seeds the box with points to start with and then expands the radius of the particles to the desired size whilst using a thermal jiggling algorithm to nudge particles out of the way if they start to overlap. This routine also informs the user if the concentration is such that crystallization occurs. It does however still have reliability problems, like the Brady low density method. These made it impractical for our purposes.

All three of these routines produce a random set of particle positions in a rectangular box lined up with the Cartesian axes. In order to use these position sets we must re-position the particles in our slanted lattice cell. The easiest way of doing this is to find the relative coordinates of each particle within the rectangular box and then convert those relative coordinates back to Cartesian coordinates using our basis. We must, however, make sure that our box is at the stage in its evolution where the angle between the basis vectors is $\frac{\pi}{2}$.
The method that we have settled on is the Zinchenko method. This because of its reliability and ease of use. We run the simulations for many repetitions (each with a different random seed) meaning that the signal to noise ratio is improved. This makes it easier to pick out general trends in the results.

3.2.1 Programming the Stokesian Dynamics Program and Technical Issues

The program that was used for all of the calculations was an implementation of the Stokesian Dynamics method outlined earlier in this thesis. A basic implementation of this code was inherited from Helen Wilson and extensive alterations, data management and error checking were bolted on. In the next section I will outline the the alterations in a brief manner.

The code was altered to allow the reading in of particle positions which had been calculated by a separate program (discussed in section 3.2). Checks are undertaken during the reading in of the particles to make sure that the same basis and calculations were used.

Implementation of Periodic basis and resetting

This is the very essence of the alterations to the Stokesian Dynamics (SD) program. The **M** matrix is chosen and the basis calculated. Which **M** matrix is chosen depends on various parameters and logical flags. There are also a series of simple routines which find the relative particle positions within a box and the real position given a relative particle position. The simulation starts by calculating the basis at right angles to one another, these are then taken as the positions at time $T/2$, with T being the time to repeat. The basis at time 0 is then calculated. The simulations run with the basis being evolved under the same background flow as the particles.

At the end of each time step the particles are placed back into the box if they have moved outside. This may be needed as during the simulation the flow may cause a particle to move outside of the box we are interested in. In this situation a corresponding particle from a neighbouring box would pop into our central box, i.e. if a particle pops out of the top of the box a particle will pop into our box from the neighbouring bottom box. Considering the box to be like a torus is the easiest way to consider the box. Every time the particles are

moved, we check if a particle has moved outside the box; if it has its relative position is used to place it back in the box.

The mobility relations and data outputs happen not at every time step but at set intervals so as to save on calculation time. The mobility relations rely on the distance between particles. Due to our lattice, each of our n particles has an image in all of the surrounding boxes. Because of the infinitely repeating periodic lattice, this means there is actually an infinite population of particles to consider. One option would be to include all particles within a given large radius. To save on computational time it was decided that for every pair of particle interaction only the closest image pair would be considered. Some accuracy is lost by this approximation, but the lubrication interactions (which are included in full) are expected to dominate over the lost terms. Ewald summation is the primary method for summing the interactions over multiple boxes and is a method we will give further consideration to later. In a very small box for a given concentration the effect of only considering the nearest neighbour may be more significant but our choice of a mid sized box should lessen this problem.

Once the basis vectors reach a repeating point they are double checked against what they should be accounting to the predetermined repeating basis. This check is to make sure no errors have been made in calculating the repeating basis and no errors have been made in the background flow of the particles.

Resetting is the final stage to take place. This is a simple affair but during development took a lot of time to get it to work correctly. The basis is simply reset back to its starting point 0 then the particles are put back into the box via their relative particle position. Before the simulation proceeds the mobility matrix must be recalculated to make sure any moved particles contribute correctly to the mobility relations.

The relative particle positions represent the positions of the particles in terms of a the normalised basis vectors of the lattice. This way if the relative particle position $\mathbf{x}_p \notin [0, 1]$ then we know that the particle has moved outside the box.

At the beginning of the simulation the position of the box at the start and the finish of the simulation is calculated, however the box is evolved with the flow and checked at the point of resetting as a method to confirm that no errors have crept into that part of the code.

Management of Runs and Data

The management of runs and data was arguably at times a bigger task than some of the scientific coding. The management and automation of dealing with multiple runs with multiple combinations is what pulls together all of the individual tasks of the computation, data processing and production of results in terms of graphs. Due to the many parameter combinations plus the multiple runs along with the long run time this was a task that needed to be automated. The static flow results were quick and only required approximately 90 runs. The dynamic results required a little less at approximately 75 runs. However with some parameter combinations taking multiple days to complete and errors, computer crashes, power failures all causing havoc and hence management of runs was key. The rough sphere calculations which we will see in chapter 4 had even greater management requirements which I shall elaborate on later.

To cope with all of these runs and data a series of BASH shell scripts were used. All runs are initially seeded and input files placed into separate directories for each run and parameter combination. Then each simulation is run using the appropriately compiled program with results being placed into named directories. Standard outputs and standard error from each run are diverted to a file and deleted in the event of a successful run, in the event of a failed run the standard output and standard error are renamed and saved to aid debugging. A list of failed and completed runs is also kept so that they both can be quickly found and the outputs examined, errors corrected and the runs resubmitted.

The BASH shell scripts also organise and rename all files during the post run

data processing described in section 3.5.4 and the gnuplots scripts described in section 3.2.1.

Data Processing

Data processing was a relatively quick process which had two main stages. The first was to calculate the Rheology from the data output from each run. This was done via the methods outlined in section 3.3. The second is taking the different runs and averaging the Rheological output over all of these runs. Another data processing task was to calculate lines of best fit on averaged runs so that comparisons could be made between different parameters runs in a quantitative manner.

Gnuplot scripts

The gnuplot scripts produce a series of different plots for all of the different individual and averaged runs. All titles, keys and legends are automatically altered via the BASH scripts in section 3.2.1. This production of a massive amount of plots allows for scanning through results in an more convenient fashion.

Ewald

The Ewald summation was one initial aim of this Thesis, unfortunately an error in the choice of the switching function resulted in the coding not being fully implemented. The code framework however was fully built and only very small alterations are required for completion. For that reason I shall describe the framework.

A logical flag, switched on the Ewald summation rather than using the nearest neighbour image as used in previous runs. Ewald summation consists of a sum in real space and a sum in reciprocal space. To alleviate this problem the Ewald summations would be tabulated. A lattice box was discretised under the relative coordinate allowed by the basis vectors, i.e $(0.5, 0.5)$ would be half

way along each basis vector. The variety of different pairings combinations were calculated with care taken not to duplicate. For example looking at figure (3.2) we can see that the pairing between p_1 and p_2 would be duplicated by p_3 to p_4. For each of these individual possible particle combinations a Ewald summation was calculated.

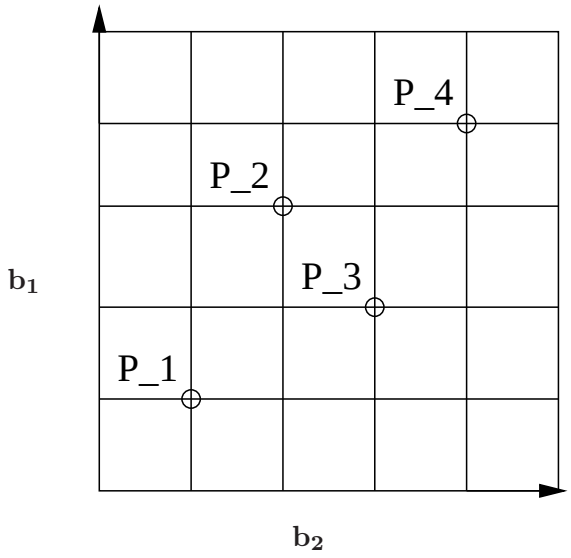

Figure 3.2: Basis vectors and subgrid of Ewald summation tabulation

Both the real and the reciprocal summation is infinite, however they are strongly convergent. Hence during the tabulation, the summation was stopped when the addition of a new round of summation contributed less than 1% to the mobility relation.

This process of special discretisation and tabulation of mobility relations was then repeated for a discrete time ranging from the start of the basis evolution at $-T/2$ to its completion at $T/2$. All of these tabulated mobility relations were then saved to text files.

During runtime, whenever a mobility value is required the nearest tabulated mobility value is used. By nearest in this case we mean that each of the tabulation parameters (simulation time, and the two relative coordinates of the particle-pair's relative position vector) is as close as possible to the actual

point required. Given this information (the three parameter values) it is then possible to choose the correct value of our mobility relationship directly from the tabulated values.

This method relied on a long set up time for any run but once tabulation had occurred, (which was then saved to text files) multiple rounds would have been achieved very quickly. This code is very close to complete and had already experienced a large amount of debugging, so given the correct sigmoidal function that still decays as required in reciprocal space results should be readily achieved.

Use of the Legion cluster

The runs of the dynamic rheology took considerable computational time. The only reason many of the runs were completed was due to generosity of friends who allowed me use of their personal computers for weeks at a time. When computational runs of rough spheres were undertaken it was necessary to acquire some more computational power. This came in the form of the Legion cluster at UCL [1]. Legion is a distributed memory computing cluster, its primary role is to run parallel code but series code can be run on it.

Legion uses MOAB and qsub to manage the submitted jobs. These queuing systems submit jobs according the the time booked to run and the number of cores required. Short serial jobs can be submitted to fill in gaps while the queuing system waits for multiple cores to become available for larger jobs, by splitting the runs up into a series of fifteen minute sections the queue manger will fit the subsections of runs into many of the small gaps created by larger waiting jobs. For any one run, the number of fifteen minute segments needed to be submitted with dependencies and the number of fifteen minute segments needed to be known prior to submissions.

Unfortunately after completion of some test runs the Legion cluster changed to the Sun Grid Engine queuing system. This allows some advantages in terms of the possibility to run array jobs. The advantage of array jobs is that more

runs can be submitted without overloading the queuing node, although placing of dependencies is still necessary.

To achieve the multiple submissions significant changes needed to be made to the code and more BASH scripts developed to submit the code in the correct manner. FORTRAN does not have a wall clock timing mechanism, to measure the running of a program for fifteen minutes, therefore a BASH script was used to keep track of time and send a variable to a .dat file when fifteen minutes had elapsed. The SD program would check this file and stop if the value was 1.

The required changes to the SD program were to make sure all data required at runtime would be output to .dat files and read back in to the SD program as the run was restarted. It was essential that run continued from the same place it had started. Just as with the dynamic rheology of the smooth runs any failed runs were logged and standard output and standard error saved so that problems could be resolved and runs be resubmitted. Initial runs also had to be done so that estimations could be calculated of the run time for each parameter combination before all of the submissions could be made. This was written to be done automatically to streamline the process.

Creating a reliable system for the submission of runs using qsub submission system and modifying the SD program to work within the system was not as simple as it may initially seem and took a considerable amount of time.

Conclusion

Computational aspects of the code contained many parts and managing the combinations of parameters and multiple runs was non-trivial. There were three main sections.

1. Scientific code,
2. Data management,
3. Post-processing.

each one being a significant task in its own right.

In hindsight and with greater programming knowledge, I would do many things differently in this program. Many of the multiple compilations could be avoided by extending the number parameters listed in text files, many of the shell scripts would be improved, tidied and possibly written from scratch. Despite many parameters being input via text files many were left out due to a seemingly ever increasingly complicated organisation system that had expanded far beyond its original intention. A few problems were also caused by the limitations of the FORTRAN language. The lack of proper wall time function, lack of structure e.t.c.

There are many difficulties, the management of the data and runs was a task in itself equal in magnitude to the scientific programming, at times in-fact it was a greater task than the scientific part of the programming. For all its inelegance the program performed well creating a large amount of data in well organised clear directories producing many results and graphics automatically. For the computation of the rough sphere results it also took advantage of the Legions cluster free node time created by parallel programs waiting for tasks. However, there are many points which could be improved upon.

3.3 Calculating Rheology from Stresslets

The Stokesian Dynamics method allows us to calculate the particle velocities and angular velocities, which we then use to move the particles in space under the action of flow; but it also allows us to calculate the stresslet $\mathbf{S}^{\alpha}$ generated by each particle α. These stresslets can be used to determine the total stress in the fluid-particle system, from which we can deduce the effective properties of the whole system. In section 3.3.1 we discuss the extraction of short-time viscosities from the stresslet data; and in section 3.3.2 we will explain how the long-time rheology can be expressed in terms of a viscosity and a normal stress difference.

3.3.1 The Short-Time Viscosity: Analysis of Stresslets in Static Runs

In our static runs, the particles are arranged at random (using the method of Zinchenko described in section 3.2). We measure the system's stress before any particle has the chance to move: so this random arrangement is the only position the particles take. This means that on average the system is isotropic, and has no microstructure.

Because of the reversibility of Stokes flow, and this isotropic underlying structure, the effect of the stress is (on average) purely scalar: that is, we expect the total system stress tensor to be a simple scalar multiple of the background rate-of-strain tensor. However, we will not assume this directly but verify it through our numerical results.

Consider the mixture of shear and strain flow discussed in section 2.3.3. This results in the background flow described by equation (2.61):

$$\mathbf{u}^{\infty} = \mathbf{G} \cdot \mathbf{x}, \qquad \mathbf{G} = \begin{pmatrix} -\gamma & 1-\gamma \\ 0 & \gamma \end{pmatrix}. \tag{3.1}$$

We know from our work in section 2.3.5 that this flow could (by rotation of the underlying axes) be put in the standard form of equation (2.90), but for the purpose of the static simulations (for which there is no motion, so a self-replicating lattice is not important) the above form is more directly useful. The case $\gamma = 0$ is a pure shear flow, while $\gamma = 1$ gives a planar straining flow, also known as extensional flow.

The property of interest to us is that of viscosity. We shall split the viscosity up into what we shall call the effective shear viscosity and the effective strain viscosity. We shall now explain what we mean by these two terms. The local stress at any point in a Newtonian fluid of viscosity μ undergoing our background flow (3.1) is

$$\sigma_{ij} = -p\delta_{ij} + \mu\left(\frac{\partial u_j}{\partial x_i} + \frac{\partial u_i}{\partial x_j}\right) = -p\delta_{ij} + 2\mu E^{\infty}_{ij}, \tag{3.2}$$

in which we have defined

$$E_{ij}^{\infty} = \frac{1}{2}\left(G_{ij} + G_{ji}\right). \tag{3.3}$$

The total stress (per unit monolayer volume) from a Newtonian fluid with suspended particles is

$$\Sigma_{ij} = -p\delta_{ij} + 2\mu E_{ij}^{\infty} + \frac{c}{2\pi a^3 n}\sum_{\alpha} S_{ij}^{\alpha}, \tag{3.4}$$

where S_{ij}^{α} are the stresslets, c is the area concentration and n is the number of particles, each having radius a. A fuller explanation of the derivation of equation (3.4) is given by and Wilson Davis in [64].

We introduce the average of the stresslets over all of the particles:

$$\overline{S}_{ij} = \frac{1}{n}\sum_{\alpha} S_{ij}^{\alpha} \tag{3.5}$$

with which equation (3.4) becomes

$$\Sigma_{ij} = -p\delta_{ij} + 2\mu E_{ij}^{\infty} + \frac{c}{2\pi a^3}\overline{S}_{ij} = \sigma_{ij} + \frac{c}{2\pi a^3}\overline{S}_{ij}. \tag{3.6}$$

Within the code, the stresslets are stored in dimensionless form, and in the form of a vector: in two dimensions this is a two element vector $\mathbf{S} = (S_1, S_2)$ and the true stresslet tensor can then be expressed as

$$\mathbf{S}^{\text{true}} = 6\pi\mu a^3 \begin{pmatrix} \frac{1}{2}S_1 - q & \frac{1}{2}S_2 \\ \frac{1}{2}S_2 & -\frac{1}{2}S_1 - q \end{pmatrix}. \tag{3.7}$$

If we define a dimensionless symmetric traceless tensor $\mathbf{s}$ from our vector via the two equations $S_1 = s_{11} - s_{22}$ and $S_2 = 2s_{12}$, we have

$$\mathbf{S}^{\text{true}} = 6\pi\mu a^3(\mathbf{s} - q\mathbf{I}). \tag{3.8}$$

The q term here comes from the extra contribution to the pressure in the fluid from the particles themselves, whose effects we neglect as it never affects the dynamics of flow if the concentration and flow field are homogeneous. Our total stress per unit monolayer volume is

$$\mathbf{\Sigma} = \sigma + \frac{c}{2\pi a^3}\overline{\mathbf{S}}^{\text{true}} = -[p + 3c\mu\overline{q}]\mathbf{I} + 2\mu\left[\mathbf{E}^{\infty} + \frac{3c}{2}\overline{\mathbf{s}}\right] \tag{3.9}$$

in which we have used the obvious notation $\overline{\mathbf{S}} = (\overline{S}_1, \overline{S}_2)$. The matrix which interests us is the deviatoric stress:

$$\boldsymbol{\Sigma}' = 2\mu \left[\mathbf{E}^{\infty} + \frac{3c}{2}\overline{\mathbf{s}} \right] = \begin{pmatrix} -\mu\gamma + \frac{3}{2}c\mu(\overline{s}_{11} - \overline{s}_{22}) & \frac{1}{2}\mu(1-\gamma) + 3c\mu\overline{s}_{12} \\ \frac{1}{2}\mu(1-\gamma) + 3c\mu\overline{s}_{12} & \mu\gamma - \frac{3}{2}c\mu(\overline{s}_{11} - \overline{s}_{22}) \end{pmatrix}. \tag{3.10}$$

Now, for a Newtonian fluid with no particles in our flow field the deviatoric stress tensor would be

$$\sigma + p\mathbf{I} = \begin{pmatrix} -\mu\gamma & \frac{1}{2}\mu(1-\gamma) \\ \frac{1}{2}\mu(1-\gamma) & \mu\gamma \end{pmatrix}; \tag{3.11}$$

so guided by this we write our deviatoric stress from equation (3.10) as

$$\boldsymbol{\Sigma}' = \begin{pmatrix} -\eta_e\gamma & \frac{1}{2}\eta_s(1-\gamma) \\ \frac{1}{2}\eta_s(1-\gamma) & \eta_e\gamma \end{pmatrix}. \tag{3.12}$$

with

$$\eta_e = \mu\left(1 - \frac{3c}{2\gamma}(\overline{s}_{11} - \overline{s}_{22})\right), \qquad \eta_s = \mu\left(1 + \frac{6c}{1-\gamma}\overline{s}_{12}\right). \tag{3.13}$$

Here η_e is the effective strain (or extensional) viscosity and η_s is the effective shear viscosity. These can be written in terms of the original vector from the code as

$$\eta_e = \mu\left(1 - \frac{3c}{2\gamma}\overline{S}_1\right), \qquad \eta_s = \mu\left(1 + \frac{3c}{1-\gamma}\overline{S}_2\right). \tag{3.14}$$

We calculate these effective shear and strain viscosities after one timestep, just before the particles are moved. For a random suspension, we expect $\eta_e = \eta_s$ and both values to be independent of the flow type parameter γ; we will verify this as a check on our code.

3.3.2 Calculating Viscosity and Normal Stress for Long-Time Simulations

Crossover linear flows between planar strain, simple shear and rotation were first studied experimentally by Giesekus in 1962 [31] and Fuller & Leal almost 20 years later [27, 28] in a four-roll mill apparatus. The earlier paper

was largely concerned with the accurate replication of these flows for a simple Newtonian fluid with tracer particles; the latter two looked at stress birefringence for a polymer solution. In neither case was there any discussion of the form of the resultant two-dimensional stress tensor.

When analysing the output of the short-time simulations of a shear–strain combination flow, as outlined in section 3.3.1 above, we simply split the raw stresslet output into a shear component and a strain component. This was possible because at that point the system is an isotropic system (plus noise), and has had no chance to build up a microstructure. This means we expect the relationship between the total stress and the background rate-of-strain tensor to be a purely scalar response: a single viscosity. The dynamic runs however are different: the motion of the particles means that a microstructure evolves during flow. This microstructure can cause a truly tensorial dependence of the total stress on the background flow rate-of-strain tensor – a non-Newtonian component – which means that we need to analyse the output in a different way.

We write the general linear two dimensional flow for our long-time runs as

$$\mathbf{u}^{\infty} = U^{\infty} \begin{pmatrix} 1-\beta & \beta \\ -\beta & -(1-\beta) \end{pmatrix} \cdot \mathbf{x} \tag{3.15}$$

for $0 \leq \beta \leq 1$. Any linear 2D flow may be written in this form, as we showed in section 2.3.5. The rate-of-strain tensor is

$$\mathbf{E}^{\infty} = U^{\infty} \begin{pmatrix} 1-\beta & 0 \\ 0 & -(1-\beta) \end{pmatrix}. \tag{3.16}$$

The resultant deviatoric stress tensor, being symmetric and traceless, may be written as

$$\mathbf{\Sigma}' = \begin{pmatrix} 2U^{\infty}(1-\beta)K & 2\beta L \\ 2\beta L & -2U^{\infty}(1-\beta)K \end{pmatrix} \tag{3.17}$$

for some constants K and L. Note that this is possible even in the extreme cases $\beta = 0$ (pure strain, in which symmetry arguments can be used to show

that the off-diagonal elements of $\mathbf{\Sigma}'$ must be zero) and $\beta = 1$ (rigid body rotation, in which the total stress is zero). K represents the total Newtonian viscosity of the suspension. L represents a cross-stress difference term: in the case of simple shear, $\beta = 1/2$, the first normal stress difference N_1 is $-L/2$ so for the sake of convention, we will set

$$N_1 = -\beta L = -\Sigma_{12}/2 \tag{3.18}$$

in all flow types, and report our results in terms of viscosity and first normal stress difference, as is conventional for two dimensional simple shear flows.

3.4 Static Simulation Results

The following results show the effective strain and effective shear viscosity as defined in section 3.3.1, calculated after one time step before the particles are moved. 300 particles were randomly seeded into the lattice box by one of the methods described in section 3.2, and a single calculation of Stokesian Dynamics for force-free, torque-free particles was carried out. To do this, all the mobility relations were calculated and summed, the resistance matrices were inverted, and the velocities, angular velocities and stresslets calculated ready to move the particles. Before any particles were moved, the stresslets were output and processed. The shear / strain ratio γ described in section 3.3.1 was varied from pure strain to just off pure shear, and a separate run with the standard pure shear basis was run to include this flow. We expect the only differences between the shear and strain viscosities to be down to statistical noise, as discussed in section 3.3.1.

As more particles are introduced (in the same area), increasing the area fraction c we would expect the viscosity to rise due to the increased contribution from the stresslets, and hence the viscosities will be a function of concentration; however, we do not expect them to depend on flow type. Therefore, where in general we could expect to see $\eta_s(\gamma, c)$ and $\eta_e(\gamma, c)$, for this short-time

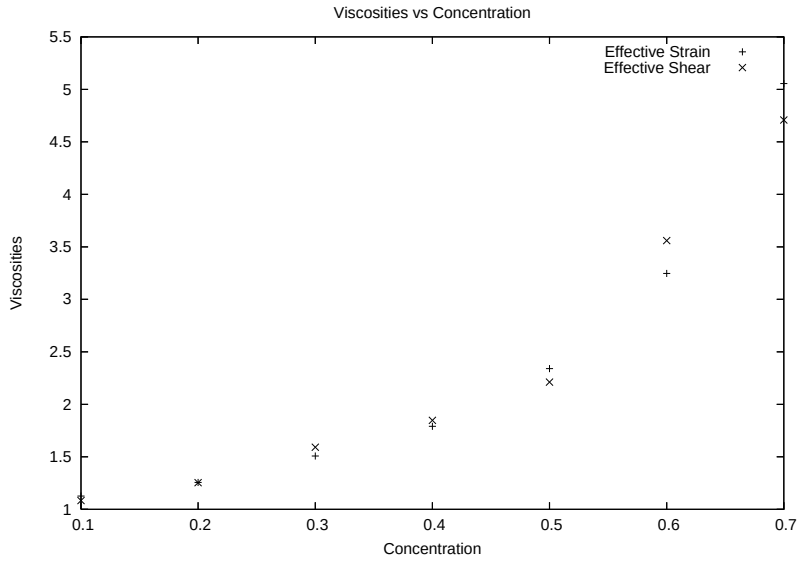

Figure 3.3: Results from Zinchenko's random seeding method.

situation in Stokes flow we expect a single viscosity value $\eta(c)$.

In section 3.2 we discussed the different methods of randomly seeding the particles in our lattice cell. We concluded that Zinchenko's random seeding method is the one that we shall use. To ascertain if there was any difference in the output between the Zinchenko and Brady methods of random seeding, for these static results we have made calculations using both the Zinchenko method and the Brady low concentration method.

In figures 3.3 and 3.4 we present the results from the two random seeding methods, Zinchenko's method and Brady's low density method, respectively. Zinchenko's method works for area concentrations up to 0.7 and Brady's low density method works for area concentrations up to 0.5.

We averaged the stresslets over all 300 particles, before calculating the viscosities as in equation (3.14). We found, as expected, that changing the type of flow had no effect on the viscosity at this stage, and that the two viscosities did not differ significantly. The flow had not yet moved the particles, so there has been no build-up of microstructure and the system acts as a Newtonian fluid with an increased viscosity η.

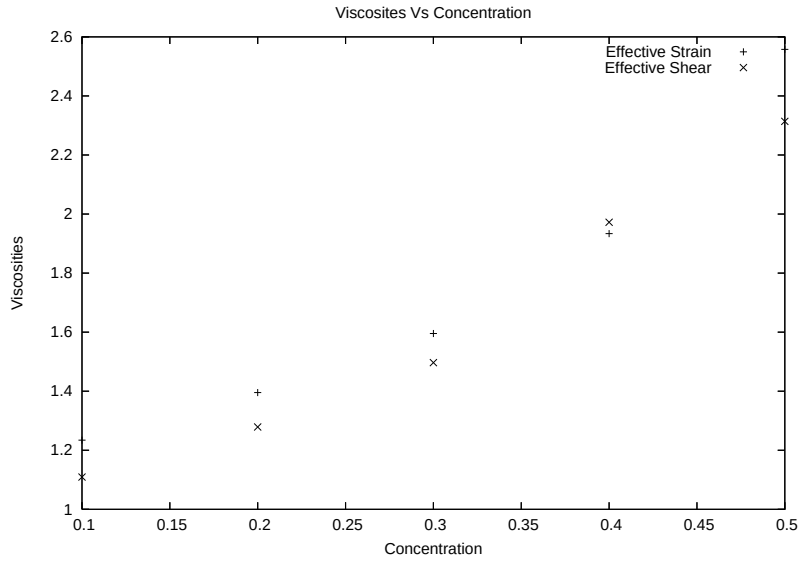

Figure 3.4: Results from Brady's low density random seeding method.

The graphs in figures 3.3 and 3.4 are created by averaging the effective viscosities over the different values of the shear ratio γ; as the effective viscosities for a given concentration did not vary significantly with γ, averaging is appropriate here. As expected, the effective shear and strain viscosities match each other closely, and the viscosities increase with increasing concentration c. Intuitively the viscosity rises with the concentration as the particle interactions operate over a shorter distance. All of the viscosity results lie above the lower limit from Einstein [22] of $\eta = \mu(1 + \frac{5}{3}c)$.

Our results are fully consistent with the hypothesis that viscosity is a function of concentration only and that the viscosity is the same whether effective shear or effective strain viscosity.

The differences between the Zinchenko method and the Brady low density method are not significant. This shows that Zinchenko's method is a valid choice for further computations.

3.5 Dynamic Simulation Results

A series of runs was undertaken at different values of the area concentration c and the flow-type parameter β. We chose representative concentration values of 0.1, 0.3, 0.4, 0.5 and 0.7, and β values of 0.1, 0.2, 0.3, 0.4, 0.45, 0.55, 0.65 and 0.75. These runs each lasted for a time of fifty repetitions of the lattice, with thirty particles within each lattice box. The initial random positioning of the particles within the lattice box was carried out using the Zinchenko method, because of its reliability over a wide range of concentrations. The resultant stresslets are averaged over all particles. This allows us to see how the viscosity and normal stress evolve with time.

The number of runs for each parameter combination ranged from one to three. Where there is more than one run, we have averaged the viscosity and normal stress at each time over the different runs. It would have been preferable to have more runs of each combination, but the total stress is already produced from an averaging of the stresslets over all particles, which does mean that the viscosity and normal stress at each time step is already averaged to some extent. Examples of the effective noise reduction form using multiple runs can be seen in the difference between figure 3.5(a) (the viscosity over time for a single run at $c = 0.4$ and $\beta = 0.1$) and figure 3.5(b) (averages over three runs for the same parameters).

In section 3.5.1 we explain the method used to extract information from the runs, and we then present the results of this analysis in section 3.5.4. The principal quantities we will investigate are the long-term viscosity, shown in tables 3.1 and 3.2 and the long-term first normal stress difference, shown in tables 3.3 and 3.4. However, we will also look at the transient build-up of microstructure (through the lens of the viscosity) and show results on the relevant rate parameter in tables 3.5 and 3.6.

In figure 3.5 we plot the first normal stress difference N_1 against time (averaged over three runs) for a concentration $c = 0.1$ and flow parameter $\beta = 0.1$ (close

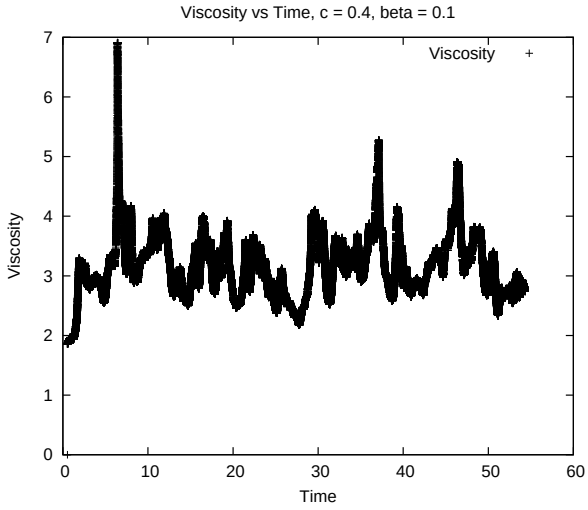

(a) Viscosity, Concentration $c = 0.4$, $\beta = 0.1$. Single run

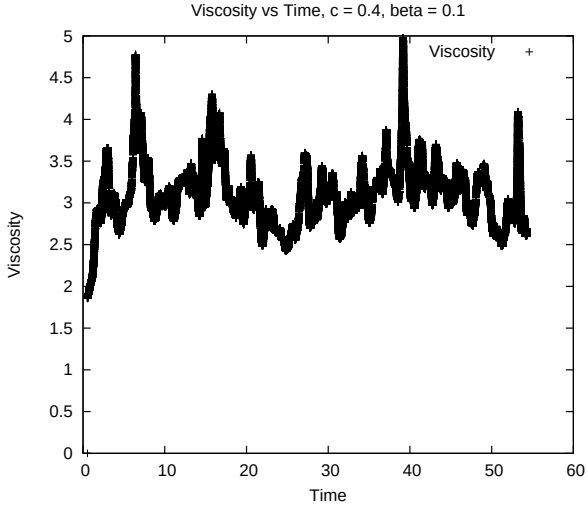

(b) Averaged viscosity $c = 0.4$, $\beta = 0.1$. Averaged over three runs.

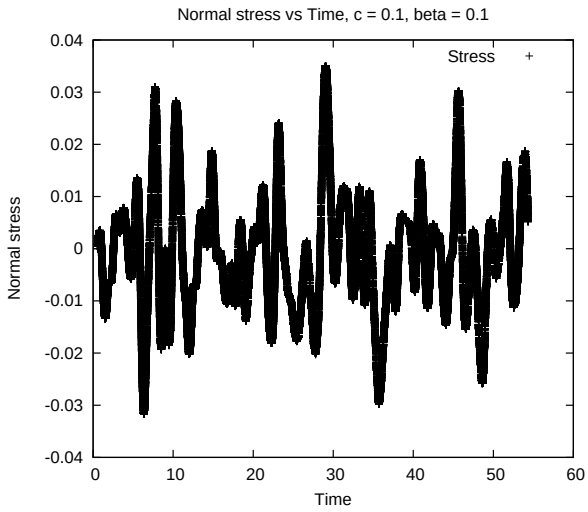

Figure 3.5: Normal stress (averaged over three runs) Concentration $c = 0.1$, $\beta = 0.1$.

to pure strain flow). Comparison with any of our viscosity plots shows that the signal-to-noise ratio is much lower for the normal stress than it is for the viscosity. This is not surprising, particularly at low concentrations, when the extra viscosity due to the particles is $5\mu c/3$ (the Einstein result) and the total viscosity is order 1, whereas the first normal stress difference is entirely caused by the particles and is first seen at order c^2. This is the reason why our transient calculations will be based on the viscosity data, and we use the normal stress data simply to extract long-term average values without assessing transients.

3.5.1 Curve fitting

Data from the dynamic runs is output as two variables, the first normal stress difference and the viscosity, as described in section 3.3.2. As an example, figure 3.6 shows the evolution of the viscosity with time for a concentration of $c = 0.4$ and a flow type parameter of $\beta = 0.1$. The viscosity starts at a low value that corresponds to the random-suspension results of section 3.4, and increases over time to a steady final value (plus noise). We hypothesise an underlying curve of the form

$$V(t) = A(1 - e^{-\alpha t}) + B, \tag{3.19}$$

where t is the time and A, B and α are real parameters. This smooth curve is also shown on figure 3.6.

A short FORTRAN program was written to fit the values of each of the unknown constants in equation (3.19).

The viscosity and normal stress should both follow the same form, and since the rate parameter α actually represents the rate at which a microstructure is built up, it should be common between the two curves for any pair of parameters $\{c, \beta\}$. At low concentrations the particle interactions are relatively weak so the microstructure will be limited, resulting in the trend of equation (3.19) being less obvious. This will be especially true for the normal stress,

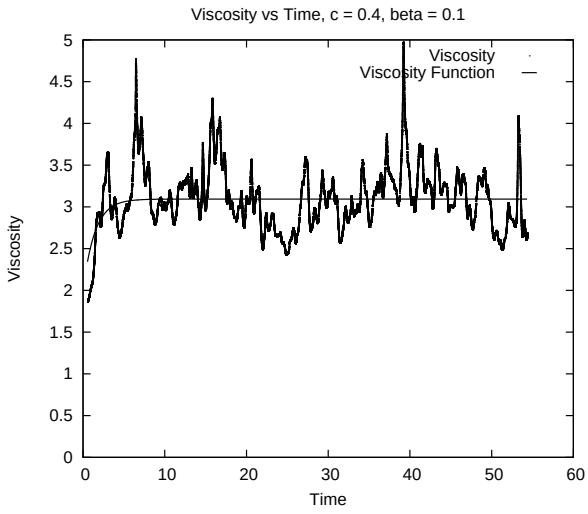

Figure 3.6: Viscosity with curve of best fit. Concentration $c = 0.4$, $\beta = 0.1$.

as discussed above: the viscosity will always be greater than one so due to the range of the graph any noise will seem comparatively less than that on the normal stress, which starts off hovering around zero. Hence in any low concentration graph the form of trend will be less obvious with normal stress due to the lower signal to noise ratio.

The parameter B represents the initial, static viscosity of the system, for which we take the results from our static simulations of figure 3.3 in section 3.4.

It would also be possible to calculate the value of B by considering say the first 5% of values from a run, however this would not be as accurate as taking the values from figure 3.3. This is because the curve which we are fitting here is only averaged over three runs at most, and has only 30 particles per lattice box, whereas the data of figure 3.3 was averaged over at least 10 runs of 300 particles per box. These clearly give a much more robust estimate of the true average value of B over many runs and many particles. Any difference in the graphs between a B value taken from the static results and the initial value in the data we are trying to fit is within the magnitude of the noise on the current data.

The second parameter A can also be easily calculated, as $A + B$ is simply the long-term value about which the viscosity stabilises. This is calculated by averaging the last 25% of values from the viscosity data file. By using the calculated value of $A + B$ and our known B value we can calculate A; in fact the quantity $A + B$, the terminal viscosity, is the one we are interested in and this is the quantity we will present in tables 3.1 and 3.2.

The final parameter α represents the speed at which the microstructure is formed within the fluid. The parameter α is calculated by an iterative method, once A and B have been determined for a given dataset. We start with an initial search interval of $\alpha \in [0, 10]$, and we define α_{min} as the the lower limit of the interval and α_{max} as the upper limit of the interval. The initial interval is established with $\alpha_{min} = 0$ and $\alpha_{max} = 10$. A step size of S is defined:

$$S = \frac{\alpha_{max} - \alpha_{min}}{10}, \tag{3.20}$$

and we iterate through the interval looking at the mean square error. Suppose the value of the viscosity from the data file is η_i at time $t_i = i * timestep$: using the formula from equation (3.19) and the parameters A and B previously calculated, for each α we calculate the error sum

$$\sum_i \left[(\eta_i - V(t_i))^2 \right]. \tag{3.21}$$

The α which gives the minimum sum is selected. If this α is neither α_{min} nor α_{max} then the new interval limits are given by

$$\alpha_{min} = \alpha - \frac{S}{2} \qquad \alpha_{max} = \alpha + \frac{S}{2}. \tag{3.22}$$

If the α was either of the interval limits then the new interval limit is defined as

$$\alpha_{min} = \alpha - S \qquad \alpha_{max} = \alpha, \tag{3.23}$$

if we had the lower limit, $\alpha = \alpha_{min}$, and similarly

$$\alpha_{min} = \alpha \qquad \alpha_{max} = \alpha + S \tag{3.24}$$

if we had the upper limit, $\alpha = \alpha_{max}$. This entire process is repeated for ten iterations, after which α is known to a high accuracy. From the data collected we never see $\alpha > 10$ so the limit on α is of no concern.

In the next sections we show the results of our dynamic runs, both as plots of viscosity (section 3.5.2) and normal stress (section 3.5.3) against time, and through tabulation of the parameters A, B and α extracted from the data as described above, in section 3.5.4.

3.5.2 Plots against time: Viscosity

We begin with plots of individual runs or small averaged sets of runs, which show the curve fitting results in context and from which all our conclusions will follow.

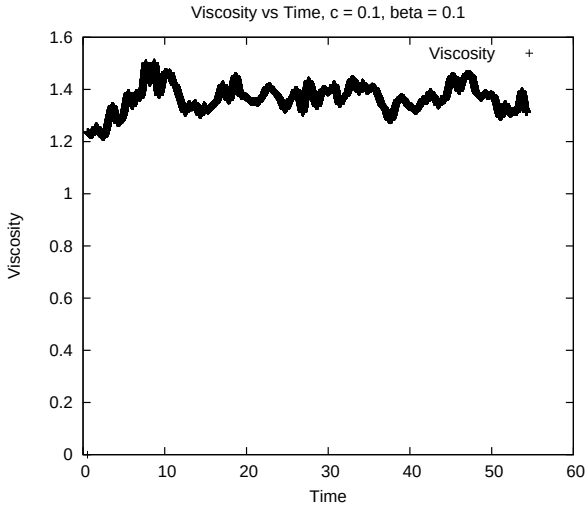

Figure 3.7: Viscosity, against time. Concentration $c = 0.1$, $\beta = 0.1$.

We look first at the viscosity. We have already seen the viscosity as a function of time, averaged over three runs, for $c = 0.4$ and $\beta = 0.1$ in figure 3.5(b). Here we start with the same flow, $\beta = 0.1$, which is close to plane strain flow, and look at the way the viscosity evolves with time at several different concentrations c. The results for $c = 0.1$ are shown in figure 3.7; those for

$c = 0.7$ in figure 3.8.

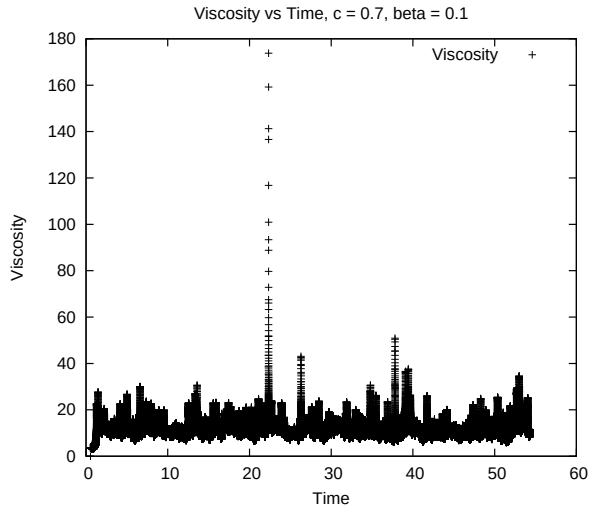

Figure 3.8: Viscosity against time. Concentration $c = 0.7$, $\beta = 0.1$.

The most noticeable feature of figure 3.8 is the spike in effective viscosity at a time of about 22, at which the suspension as a whole seems to have a viscosity over 150 times that of the suspending fluid. This is our first indication that some sort of jamming or crystallisation phenomenon may be occurring. There are no such extreme spikes at $c = 0.1$ (figure 3.7) or $c = 0.4$ (figure 3.5(b)).

We now move on to another representative flow type: in this case $\beta = 0.45$ which is close to shear flow (but just on the strain side rather than the rotation side). Here we plot the viscosity for moderate and high concentrations: figure 3.9 is at $c = 0.4$ and figure 3.10 at $c = 0.7$.

In figure 3.9 we begin to see the viscosity spikes characteristic of crystallisation; comparing with the same concentration at a lower value of β (figure 3.5(b)) we see that the spikes are much stronger at $\beta = 0.45$ than they were at $\beta = 0.1$. This leads us to the tentative idea that changing the flow type from strain towards shear or rotation may enhance crystallisation.

In figure 3.10 we see the same flow type again, $\beta = 0.45$, but at a much higher concentration $c = 0.7$, a concentration at which we would expect to see

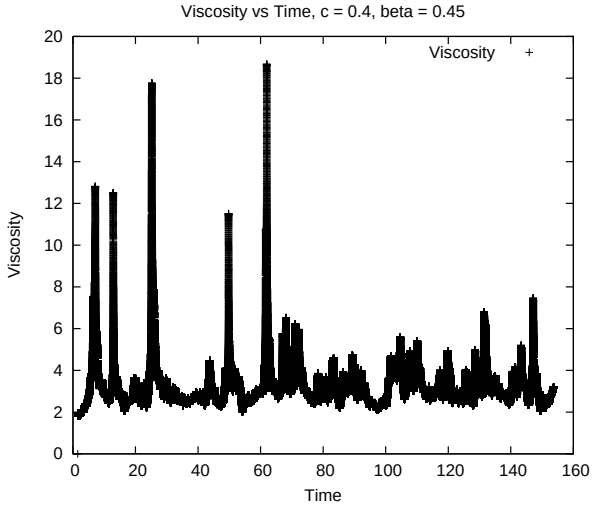

Figure 3.9: Viscosity, averaged over three runs. Concentration $c = 0.4$, $\beta = 0.45$.

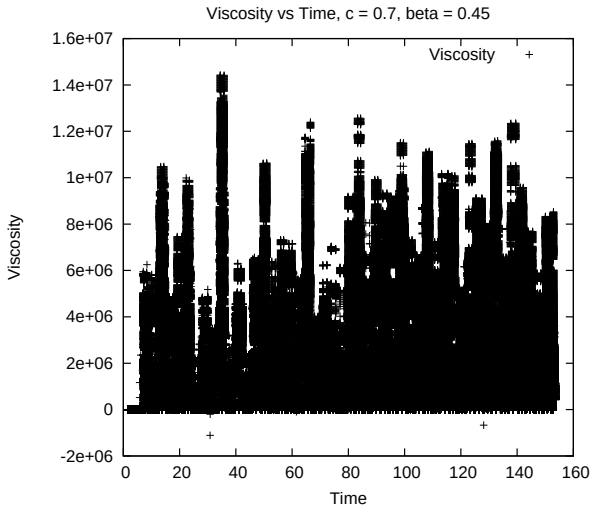

Figure 3.10: Viscosity, averaged over three runs. Concentration $c = 0.7$, $\beta = 0.45$.

some crystallisation in any flow. Again, we see that the viscosity spikes are much larger here than they were for the same concentration at lower β (figure 3.8): at $\beta = 0.1$ the maximum viscosity we saw was around 200μ, whereas at $\beta = 0.45$ we are seeing values up to $1.5 \times 10^7 \mu$.

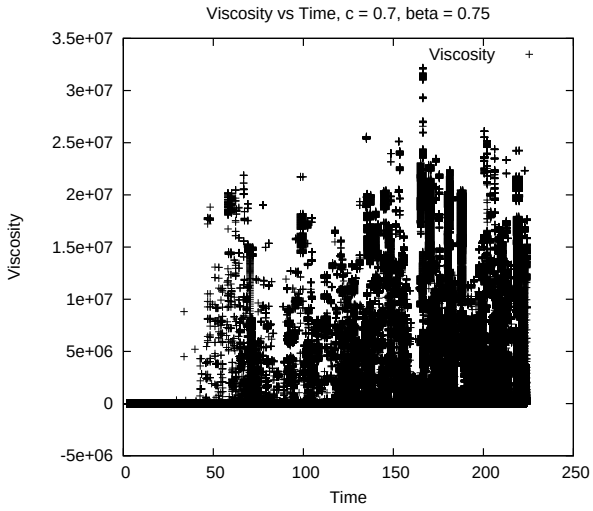

Figure 3.11: Viscosity *vs* time $c = 0.7$, $\beta = 0.75$.

Finally for this section, in figure 3.11 we show one graph for a flow type between shear and rotation: $\beta = 0.75$. Here, again, we are at a very high concentration $c = 0.7$, at which we would expect some crystallisation to occur within the flow.

As expected, we see the characteristic viscosity spikes we associate with jamming or crystallisation: and here, the maximum viscosity is over $3 \times 10^7 \mu$, another factor of 2 larger than that seen at the same concentration for $\beta = 0.45$. This corroborates our idea that changing the flow towards rotation enhances the crystallisation.

3.5.3 Plots against time: Normal stress

Earlier, in figure 3.5 we saw the evolution of normal stress against time for a low concentration $c = 0.1$ and a flow close to strain, $\beta = 0.1$. The noise

had a typical magnitude around 0.03 — not large, but at least an order of magnitude larger than the mean normal stress in this case.

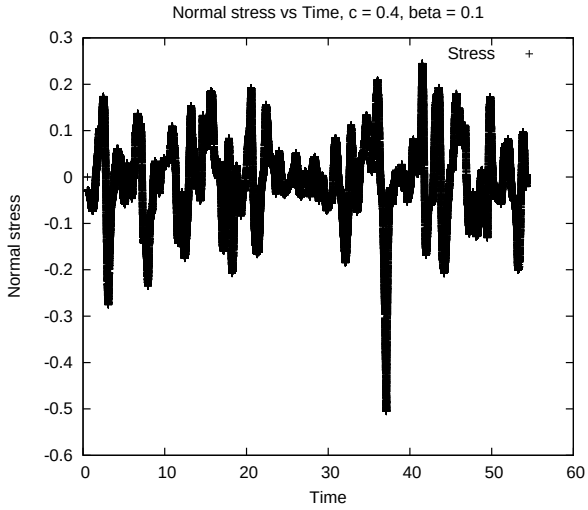

Figure 3.12: Normal stress (averaged over three runs). Concentration $c = 0.4$, $\beta = 0.1$.

In figure 3.12 we show the equivalent plot for a higher concentration $c = 0.4$. We can see that the noise level has increased, whereas the average value of the first normal stress is still so small as to be indistinguishable from zero on the scale of the graph. When we plotted the viscosity at these parameters we did not see the characteristic spikes of jamming or crystallisation; however, the increased inter-particle interactions at the higher concentration are clearly causing some increased noise here.

Because of the magnitude of the noise in these data, we cannot extract transients from our normal stress results. The zero-time results for normal stresses are all zero because of the isotropy of the random system, and so we would be looking for a transient from zero to a very small value through relatively large noise. Instead, we will simply report the average normal stress for each set of parameters, in tables 3.3 and 3.4.

3.5.4 Tabulated Results

In this section we show the results of the curve fitting described in section 3.5.1. For each pair of parameters $\{c, \beta\}$ we have calculated the terminal viscosity (shown in tables 3.1 and 3.2) and the average normal stress (shown in tables 3.3 and 3.4). We have also calculated the rate constant α which governs the evolution of the microstructure build-up, from the viscosity data, and we report these results in tables 3.5 and 3.6. We do not report the short-time viscosities here as these have already been discussed in section 3.4.

c	$\beta = 0.1$	$\beta = 0.2$	$\beta = 0.3$	$\beta = 0.4$
0.1	1.37	1.34	1.41	1.37
0.3	2.46	2.27	2.36	2.27
0.4	3.09	2.9	2.89	3.10
0.5	4.62	4.70	4.89	4.71
0.7	11.01	16.73	2.88×10^5	9.85×10^5

Table 3.1: Terminal viscosity, $\beta = 0.1 - 0.4$.

c	$\beta = 0.45$	$\beta = 0.55$	$\beta = 0.65$	$\beta = 0.75$
0.1	1.35	1.28	1.26	2.97
0.3	2.00	1.915	2.35	1.82
0.4	3.15	3.15	2.86	2.18
0.5	4.41×10^5	7.70×10^5	70.56	4.20
0.7	2.61×10^6	1.18×10^6	7.46×10^5	2.92×10^6

Table 3.2: Terminal viscosity, $\beta = 0.45 - 0.75$.

We begin with the terminal viscosity, shown in tables 3.1 and 3.2. There is a clear and marked increase in viscosity as concentration increases, for any fixed value of β. This is to be expected: a more dense suspension offers higher resistance to flow and so has a higher viscosity. We also saw this phenomenon in the short-time viscosity results of section 3.4.

For moderate concentrations up to $c = 0.4$, there seems to be little dependence of the viscosity on the flow parameter β. As an instance of this, in figure 3.13

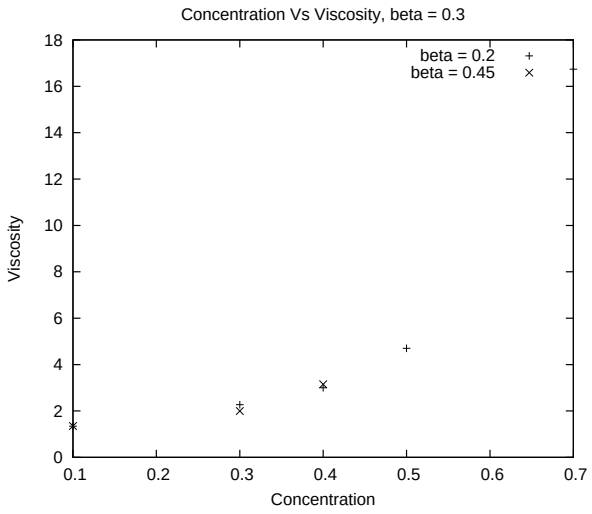

Figure 3.13: Concentration *vs.* viscosity at $\beta = 0.2$ and $\beta = 0.45$.

we show the terminal viscosities at both $\beta = 0.2$ and $\beta = 0.45$, plotted against concentration. The values are virtually indistinguishable.

However, there are some extreme values in tables 3.1 and 3.2, which allow us to see at a glance where our freely-flowing simulation breaks down and crystallisation or jamming occurs. It is clear for example that with a concentration of $c = 0.7$ any $\beta > 0.2$ results in a massive viscosity and breakdown of the model. What is surprising is how low the concentration can be when under some flows crystallisation occurs: for instance at a concentration of $c = 0.5$ and $\beta = 0.45$; for the same concentration, crystallisation ceases as we approach pure rotation. These large viscosity increases coincide with an increase in the noise on our data (which can't be seen in the tables of this section).

We now move on to the normal stress results. Because the initial normal stress is zero and the signal-to-noise ratio so low for these results, we cannot assess transients with them, and instead simply present the average normal stress over the whole run in each case. Table 3.3 shows the results for β up to 0.4, and table 3.4 those for $\beta \geq 0.45$.

For moderate concentrations (c up to around 0.4) the results listed in tables

c	$\beta = 0.1$	$\beta = 0.2$	$\beta = 0.3$	$\beta = 0.4$
0.1	-0.97×10^{-3}	-0.19×10^{-2}	-0.29×10^{-2}	-0.41×10^{-2}
0.3	-0.41×10^{-3}	-0.11×10^{-1}	-0.20×10^{-1}	-0.171×10^{-1}
0.4	-0.70×10^{-2}	-0.86×10^{-2}	-0.35×10^{-1}	-0.36×10^{-1}
0.5	0.22×10^{-1}	-0.19×10^{-1}	-0.23×10^{-1}	-0.30×10^{-1}
0.7	0.25×10^{-1}	0.15×10^{-1}	-0.94×10^{3}	0.17×10^{4}

Table 3.3: Average normal stress, $\beta = 0.1, \ldots, 0.4$.

c	$\beta = 0.45$	$\beta = 0.55$	$\beta = 0.65$	$\beta = 0.75$
0.1	-0.27×10^{-2}	0.52×10^{-5}	0.66×10^{-4}	-0.24×10^{-2}
0.3	-0.17×10^{-1}	-0.63×10^{-3}	-0.21×10^{-3}	-0.13×10^{-4}
0.4	-0.26×10^{-1}	-0.26×10^{-1}	-0.15×10^{-2}	-0.72×10^{-4}
0.5	-0.262×10^{2}	0.37×10^{1}	0.85×10^{-1}	-0.58×10^{-3}
0.7	0.14×10^{4}	0.89×10^{3}	-0.12×10^{2}	0.27×10^{3}

Table 3.4: Average normal stress, $\beta = 0.45, \ldots, 0.75$.

3.3–3.4 are broadly level, showing little effect of either β the flow type, or the concentration c on the normal stress. Indeed, the values are so small that it is not even possible to be certain of the average sign of the normal stress difference.

At higher concentrations there is a marked increase in the magnitude of the normal stress values: but still no consistent trend for the sign of the normal stress. If we return to the raw data we see that this is because the noise has become orders of magnitude larger at these higher concentrations; in all cases the normal stress appears to be oscillating around a small or zero value. Thus all we can say from our normal stress study is that the first normal stress difference is not significant enough to be measured with a small system such as ours, and appears to be largely independent of flow type.

3.5.5 Crystallisation

From our viscosity results we hypothesised that some form of jamming or crystallisation event was taking place during the flow. In this section we look at snapshots of the particle positions to attempt to confirm this theory.

Our idea is that higher concentrations cause crystallisation — which is hardly controversial — but also that flows close to shear, having β close to 0.5, trigger crystallisation at lower concentrations than those close to pure strain or pure rotation.

At high concentrations there is a rapid build up in microstructure, shown by both the increased viscosities and the increased noise level. We believe that the build up of microstructure causes the increase in noise most probably because of crystallisation forming in chunks causing massive viscosity and normal stresses. There will, however, still exist some areas of free flowing particles: but when a formed crystal becomes aligned so that it spans our lattice box, we see a large spike in the total viscosity.

This jamming effect, when a single crystalline structure spans our periodic box, is partly caused by the small number of particles in our simulations (only 30 per box), so we cannot expect to quantitatively predict real suspension viscosities with these simulations; however, the trends for when crystallisation occurs are expected to be robust.

Looking at an instantaneous plot of the particle positions we should be able to see whether or not crystallisation is occurring. In the graphs that follow, each cross represents the centre of a particle of radius 1, and the borders of the periodic lattice box are drawn around our particles. Initially we consider $\beta = 0.1$, a flow close to strain flow, and vary the concentration from $c = 0.1$ in figure 3.14(a) through $c = 0.3$ (figure 3.14(b)) and $c = 0.5$ (figure 3.14(c)) to $c = 0.7$ in figure 3.14(d). Regions of crystallisation have a characteristic regular triangular pattern, with series of particle centres lying in straight lines: we can see that as c increases, more of the particles become part of crystalline

structures until at $c = 0.7$ we almost have a solid mass of particles.

Let us look in more detail at the runs pertaining to $\beta = 0.1$. We have seen from the particle positions that when $c = 0.1$ there are only very isolated regions of crystallinity, whereas with increasing c, even at moderate values $c = 0.3$ and $c = 0.5$ a much higher proportion of the particles are involved in crystal-like regions. When the viscosity and normal stress are averaged over all particles, if the proportion of particles involved in crystals is small, the resultant noise is only moderate, as for instance at $c = 0.1$ in figure 3.7. However, as the proportion of the particles involved in crystallisation increases, the extreme viscosity and normal stress values become more prevalent and do not average out, as at $c = 0.4$ in figure 3.6. This continues to happen as c increases until we are at a point where all the particles are part of a crystalline mass resulting in the extremely noisy data, as at $c = 0.7$ in figure 3.8.

The flow parameter β also has an effect on crystallisation. The mechanism behind this appears to depend on how unidirectional the flow is. We know that the amount of crystallisation increases with the concentration for any given value of β, however the effect on the viscosity and normal stress is not uniform for a given concentration: variation in β affects the viscosity results and the level of noise (indicating jamming events) in both the viscosity and the normal stress.

In figures 3.14(e)–3.14(g) we show snapshots of particle positions for $c = 0.4$ and β varying between $\beta = 0.1$ in figure 3.14(e), close to strain flow, $\beta = 0.45$ in figure 3.14(f), close to shear flow, and finally $\beta = 0.75$ in figure 3.14(g), a rotational flow with an element of shear. Although there are crystalline regions in all three plots, we see a much stronger crystal formation at $\beta = 0.45$.

We can explain this effect in terms of the multi-directional nature of the flow field. At $\beta = 0.1$ (figure 3.14(e)) the flow is very similar to plane strain, which pulls particles apart along the extensional axis while pushing them together on the compressional axis. Crystals are formed by the compression but immediately broken by the extensional flow, allowing particles to pass one

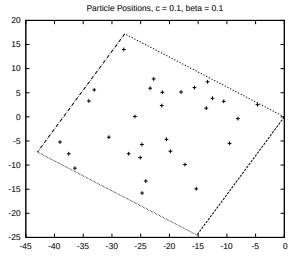

(a) Particle positions. Concentration $c = 0.1$, $\beta = 0.1$.

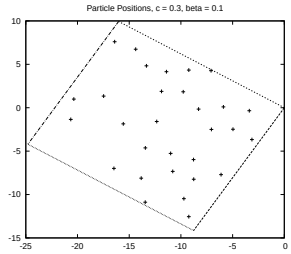

(b) Particle positions. Concentration $c = 0.3$, $\beta = 0.1$.

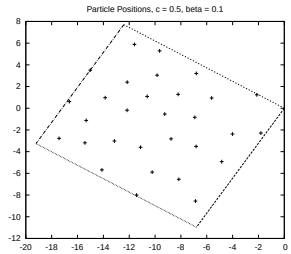

(c) Particle positions. Concentration $c = 0.5$, $\beta = 0.1$.

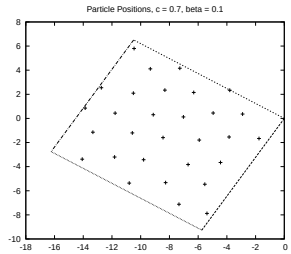

(d) Particle positions, Concentration 0.7, $\beta = 0.1$.

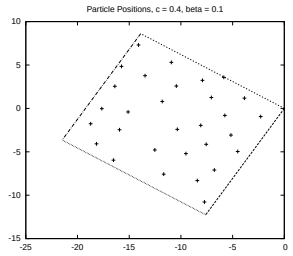

(e) Particle positions. Concentration $c = 0.4$, $\beta = 0.1$.

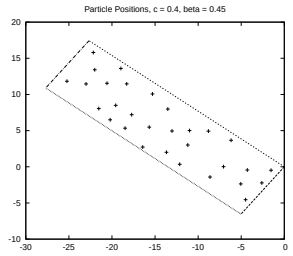

(f) Particle positions. Concentration $c = 0.4$, $\beta = 0.45$.

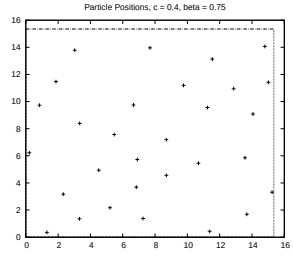

(g) Particle positions. Concentration $c = 0.4$, $\beta = 0.75$.

another unrestricted. For this flow the viscosity noise is reasonable, as shown in figure 3.5(b).

Considering $\beta = 0.45$, with particle positions shown in figure 3.14(f), the flow is very close to a shear flow corresponding to $\beta = \frac{1}{2}$. We can see that the particles are lined up along the line $y = -x$ of the shear flow; the noise in this case is very large for such a moderate concentration, as seen in figure 3.9. Because the flow is almost unidirectional, it is insufficiently violent to break up crystalline regions, resulting in the short-term jamming events and the spikes in the viscosity. These have only a moderate effect on the average viscosity, but are locally very large.

When we approach a more rotational flow such as $\beta = 0.75$ the noise decreases again, and indeed the average viscosity (table 3.2) falls from 3.15μ at $\beta = 0.45$ to 2.18μ at $c = 0.75$. The particle arrangements, shown in figure 3.14(g), are similar to that of $\beta = 0.1$.

This effect, as with any jamming phenomenon, is more prevalent at higher concentrations as it does require some initial crystallisation to start off with. Finally, in figure 3.14 we show the particle positions for our most crystalline system: $c = 0.7$, an area concentration at which we expect high levels of crystallisation regardless of the flow, and for one of the most unidirectional flows, $\beta = 0.45$. We can see that all the particles seem to be involved in a single large crystal structure: all the centres lie on straight lines. It is no surprise that this is the pair of parameters $\{c, \beta\}$ at which our viscosity peaks: we calculate a viscosity value of $0.26 \times 10^7 \mu$ for this suspension.

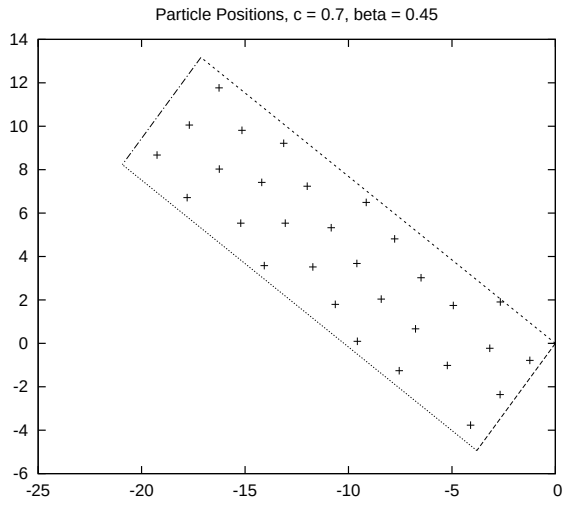

Figure 3.14: Particle positions. Concentration $c = 0.7$, $\beta = 0.45$.

3.5.6 Rate of Build-up of Microstructure

We described in section 3.5.1 the procedure for fitting a decaying exponential transient to our viscosity results. Since both the normal stress and the viscosity are functions of the microstructure built up within the flow, we expect them to have transients with the same rate constant α; however, the normal stress data are too noisy for this to be confirmed.

By this fitting process, we have determined a rate constant for the evolution of the microstructure within the flow, at each set of flow conditions $\{c, \beta\}$. These results are given in tables 3.5 and 3.6.

β Concentration	0.1	0.2	0.3	0.4
0.1	0.33	0.49	0.058	0.20
0.3	0.53	0.99	0.26	0.32
0.4	0.70	0.50	0.57	0.46
0.5	0.84	0.66	0.31	0.53
0.7	1.0	2.85	0.073	0.063

Table 3.5: Rate constant α for viscosity evolution, $\beta = 0.1, \ldots, 0.4$.

β Concentration	0.45	0.55	0.65	0.75
0.1	0.30	1.00×10^{-2}	2.56×10^{-2}	0.61
0.3	0.32	0.44	7.28×10^{-3}	9.13×10^{-3}
0.4	0.47	0.47	8.39×10^{-3}	4.69×10^{-2}
0.5	1.15×10^{-2}	4.37×10^{-3}	2.84×10^{-3}	2.48×10^{-2}
0.7	2.48×10^{-2}	5.34×10^{-2}	4.91×10^{-3}	5.68×10^{-3}

Table 3.6: Rate constant α for viscosity evolution, $\beta = 0.45, \ldots, 0.75$.

We might expect the rate at which the microstructure forms increases with concentration, due to particle interactions become more frequent as the concentration increases, allowing the system to reach its equilibrium microstructure faster. At low concentrations, particles rarely interact so the microstructure takes longer to form. However, this trend is not a clear trend in the tables, this could potentially be because the rates at the higher concentrations

are not reliable due to the viscosity spikes resulting in whole curve not fitting well by our transient exponential.

The flow parameter β seems to have little effect on the rate of evolution of the microstructure. In a sense, this is also unsurprising: the rate of particle interactions depends on the flow strength rather than the flow type, and so we do not necessarily expect the flow type to affect the rate of microstructure build-up.

3.5.7 Conclusions

We have been unable to draw conclusions about the behaviour of the normal stresses from our small runs with only 30 particles; to fully investigate the non-Newtonian behaviour of such a suspension would require larger simulations.

The viscosity results, on the other hand, have been very informative. Moving from static to dynamic runs made little difference to the overall picture regarding the dependence of viscosity on concentration, c: as expected, the viscosity increases with increasing concentration, as does the rate of build-up of viscosity (and of the underlying microstructure).

However the dynamic runs do allow us to see when crystallisation occurs, and how serious it is. There is, of course, a dependence of crystallisation on concentration; but crystallisation also depends on β, the flow parameter. Crystallisation occurs most seriously at flows closest to shear flow $\beta = \frac{1}{2}$. This appears to be because the flow is approximately unidirectional for these flows and so flow has no mechanism to pull apart incipient crystals.

Our results are inevitably limited by the number of particles in our simulations (only 30 in each repeating box) which means a spanning crystal may form earlier in our work than a true jamming structure would in practice. However we expect our conclusions about the effect of flow type on jamming to be robust. It is also possible that these jamming results may be less pronounced with the addition of Brownian motion to the system, as the small random

motions may allow the particle to move past each other more easily.

3.6 Effect of Number of Particles

The high viscosity spikes we have seen occurring in the simulations of section 3.5 are believed to be because of the onset of crystallization. The surprising result is the early onset of crystallization. This early crystallization onset could be due to clusters of particles forming that span our tessellated box, which in turn due to its torus nature would result in an infinite band of crystallization. To investigate this possibility two extra scenarios were run.

1. A series of extended larger box runs.

2. A extend larger box run.

We chose two set of parameters where we see viscosity spikes, and carried out a series of simulations with different numbers of particles.
The extended run uses a series of concentrations and flows to compare the viscosity results to those given in 3.5. The difference from our earlier work is that in each box there are 300 particles rather than 30 so for each concentration the box is appropriately scaled.
The runs where the numbers of particles is varied with consistent flow to see the effect of the box size across one flow which is know to cause viscosity spikes. Wilson Davis 2001 [64] used 25 particle in their simulations so our choice of 30 is also consistent with others in the literature.

3.6.1 Varying n

The variation of N was done for a flow of $\beta = 0.45$ and concentration 0.4 and 0.7. The number of particles varied from $n = 10$, 30, 100, 300 and 1000. The flow of $\beta = 0.45$, a shear flow with some strain was chosen because it is a flow which causes crystallisation to occur.

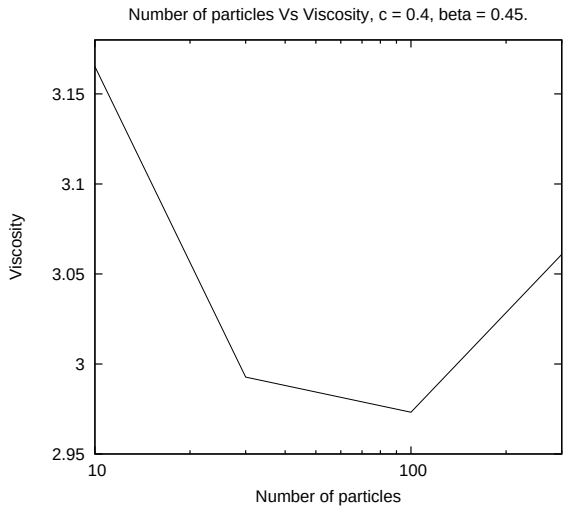

Figure 3.15: Viscosity *vs* number of particles. $c = 0.4$,$\beta = 0.45$.

Unfortunately after doing an initial trial run for $n = 1000$ the estimations were coming through that it would take something of the order of 400 days worth of computation for 1 run. Figure 3.15 shows that the number of particles is shown to have little effect on the viscosity. There apart to be a slightly higher viscosity for the very small n example of $n = 10$ but by $n = 30$ the viscosity has levelled off. This also supports our choice of 30 particles per box used in the runs.

3.6.2 Extended run

The parameter combinations for the extended runs are shown in table 3.7. Three runs of each combination were done with $n = 300$ particles in a box for 30 repetitions of the box.

Figure (3.16) is a good example of the close matching of viscosities of a lattice with 300 particles per box *vs* 30 particles per box. The larger number of particles shows much the same viscosities with only a slightly higher viscosity reading at high concentrations. This is consistent with the data found in the previous section with a varying number of particles n. Similar results can be

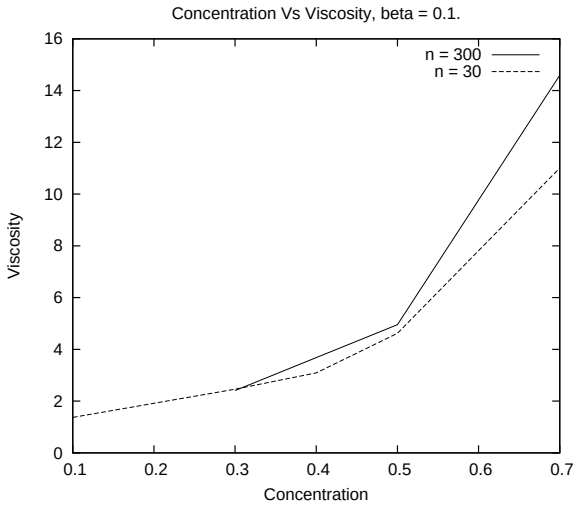

Figure 3.16: Viscosity for $n = 300$, $\beta = 0.1$.

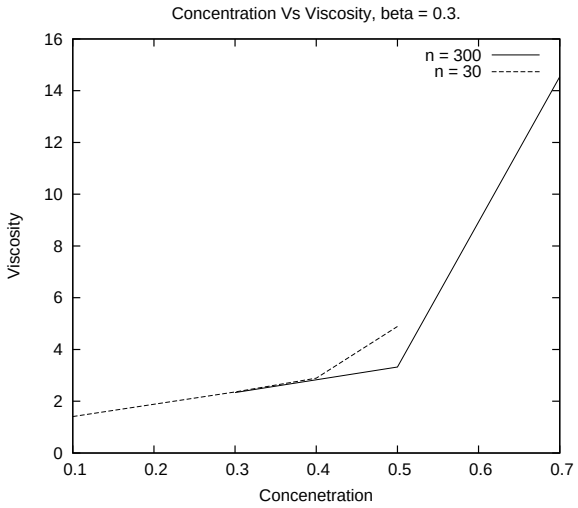

Figure 3.17: Viscosity for $n = 300$, $\beta = 0.3$.

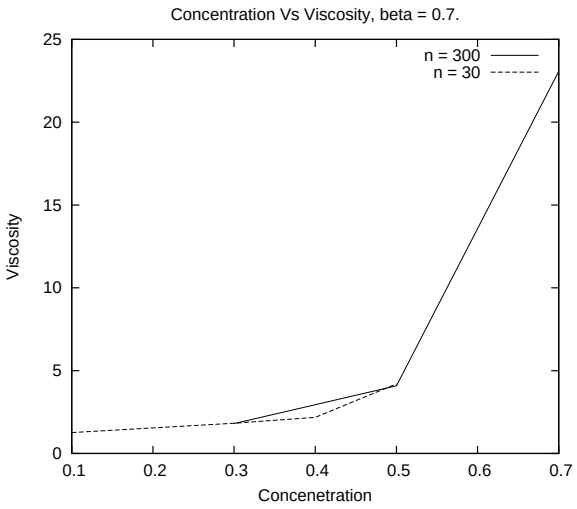

Figure 3.18: Viscosity for $n = 300$, $\beta = 0.7$.

seen in figures (3.17) and (3.18) where we have fully completed runs. This gives further confidence in the opinion that a lattice with $n = 300$ particles per box offers little advantage over a lattice with $n = 30$ particles per box. The only significant difference occurs at high concentrations such as $c = 0.7$. At these very high concentrations there does appear to be a lower although still high viscosity in the runs with 300 particles. This is no doubt due to clusters of particles forming that span the box at $n = 30$ but not at $n = 300$. The computational time over head however for running boxed with 300 particles is too great for the extra information gained. It is clear that at higher concentrations large clustering does form however this information does places question on how large these clusters are and if the result in full crystallization of the domain.

Parameter	Values		
Concentration	0.3	0.5	0.7
Shear ratio β	0.1	0.3	0.7

Table 3.7: Combinations of extended smooth runs

Chapter 4

Rough Spheres

In the following section we will consider the effect of small irregularities or roughness on the surface of the particles. The issue of surface roughness was first considered to explain experimental observations in which particle trajectories were not reversible, as would be expected for Stokes flow.

4.1 Literature Review

4.1.1 Experimental Studies

Lubrication theory predicts that two perfectly smooth particles in a viscous fluid will never actually touch under the action of finite forces due to lubrication resistance. Also, as a consequence of the reversibility of Stokes flow, there are many theoretical symmetries in the flow of two spheres. For example, two particles passing each other as shown in figure 4.1 should follow a path which has reflective up-down symmetry.

However, there is a lot of experimental evidence to suggest that real particles do come into contact in flow, due to the presence of surface roughness. This is typically observed by the breaking of some expected symmetry of Stokes flow. Probably the first such observation was by Arp & Mason in 1977 [4],

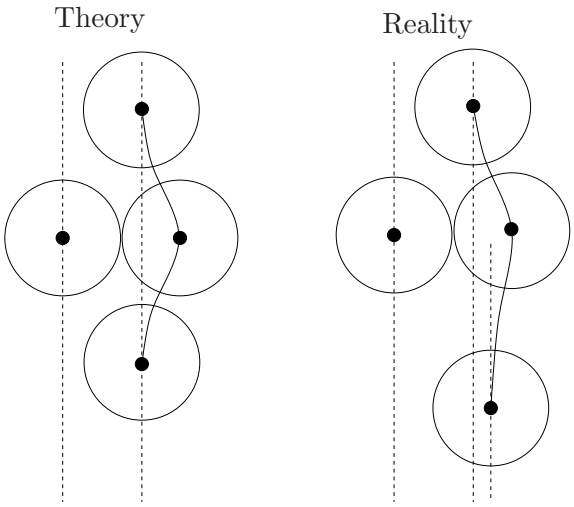

Figure 4.1: A heavy particle falling past a neutrally-buoyant or fixed particle in Stokes flow. On the left: theory predicts that the initial horizontal offset between the particles is the same as the final horizontal offset. On the right: experiments sometimes show a different result, that the final offset is larger than the initial offset.

who carried out experiments on two spheres close together in a shearing flow. They observed, using rough particles with very small surface roughness, that two particles close together in a shearing slow rotated as a pair when in contact, and then separated, which broke the closed orbits predicted for smooth particles at low Reynolds number. Contact between the particles due to the surface roughness was suggested as a mechanism to explain this phenomenon. Smart 1989 [54] performed experiments to determine the roughness heights of microscopically rough particles. This was done by allowing a sphere to settle for a long time on a smooth horizontal surface, then inverting the container and measuring the time taken for a sphere to fall one particle diameter away from the surface. The known lubrication interactions between a smooth sphere and a plane wall were then used to deduce the height at which the sphere had halted above the plane. This nominal surface roughness was of the order $10^{-2} - 10^{-3}$. Measurements of the particle surface roughness were also taken by electron microscope and shown to be in quantitative agreement.

Tabatabaian and Cox (1991) [56] undertook experiments with real particles

and showed that the symmetry required by the reversibility of a Stokes flow was broken in shear flow and also in sedimentation. Smooth and rough sphere models were compared. Contact via surface roughness was shown to predict the same breakdown in reversibility.

Smart et al 1993 [53] measured the translational and rotational velocity of a rough sphere falling down an inclined plane using digitized video. Rolling and slipping were both observed. A model was proposed which allowed contact between the surface roughness (small half spheres) and the plane taking into account both roll and slip.

Galvin (2001) [29] extended the work Smart [53] and previous work of by including two roughness scales on the same sphere and considering the sphere falling down a plane with different levels of inclination. We will refer back to some of the data from this paper later.

Zhao, Galvin and Davis 2002 [69] considered a sphere rolling down a plane but considered the roughness to be on the plane. Two roughness heights were placed on the plane resulting in the sphere only coming into contact with large asperities at higher angles of inclination.

Yang et al 2006 [66] conducted experiments of smooth and rough heavy spheres in a rotating cylinder. Contact with the cylinder wall only occurred with artificially roughened spheres. They postulated that cavitation in the lubrication boundary layer breaks the symmetry of the flow.

4.1.2 Contact Models and The Effects of Contact

Davis 1992 [17] proposes both a stick rotate and a slip rotate model. The paper considers a heavy sphere falling though a field of smaller neutrally buoyant spheres, Brownian motion is ignored. Results concluded that the roll slip model gave better agreement to experimental data than roll stick. Zeng et al. (1996) [68] conducted some experiments with a heavy sphere falling past a neutrally buoyant sphere of the same size. The results verified the roll slip

model of Davis [17]. This showed the breaking of symmetry caused by surface roughness.

Rampall, Smart and Leighton 1993 [49] carried out experiments in which a dilute suspension of identical spheres was sheared and the pair distribution function in the plane of shear measured as directly as possible by optical means. They observed that the distribution function is modified in the downstream (extensional) quadrant behind a sphere centred at the origin, with closed orbits being eliminated in the plane of shear, and an exclusion zone behind the particle, and they were able to reproduce this behaviour using a very simple contact force law (hard-sphere repulsion). They did discuss, however, the fact that the pair distribution function is likely to be a rather insensitive function of the roughness interaction: any contact law that breaks the closed orbits and forces particles apart is expected to produce a qualitatively similar PDF.

Davis and Hill 1992 [18] consider a heavy sphere falling though a field of smaller neutrally buoyant spheres. A high Pe number was considered so that hydrodynamic diffusivity could be considered rather than thermal diffusivity. Diffusivity was shown to increase dramatically as the size ratio is increased. For large size ratios lubrication forces are dominant resulting in a high sensitivity to transverse movement; because of this Davis and Hill hypothesise that surface roughness or weak Brownian motion may be a very important feature and its effect on breaking of symmetry is discussed.

Da Cunha and Hinch 1996 [15] consider the effect of surface roughness on diffusivity following on from Davis and Hill [18]. The model used considers no effect of the roughness on tangential motion or rotational motion. Larger asperities are shown to produce more diffusion.

Dratler and Schowalter 1996 [20] implemented non-Brownian Stokesian Dynamics in a monolayer under a simple shear flow. Smooth and rough spheres were considered and short range repulsive forces are concluded to be essential to produce realistic micro-structures and to reduce the particle overlap which can result from numerical errors.

Brady and Morris [12] 1997 consider the symmetry of flows around spheres. Low and high Pe numbers are considered. A simple hard contact model is used to introduce macroscopic stress to the system. The model is a very simple Heaviside step function which applies a force related to the hydrodynamic force which the sphere feels, i.e. $6\pi\mu a\mathbf{U}$. The initial model derivation considers a general linear flow, but detailed analysis was only carried out on simple shear and planar two dimensional extensional flow but the conclusions for other flows were expected to be the same. Among their many conclusions, high Pe numbers experience shear thickening, this was increased with inter-particle forces but the magnitude created with particle pair interactions may not be enough to explain the levels seen experimentally.

Ekiel-Jeżewska 1999 [23] considers rough spheres and introduces, another hard contact model which includes roll and roll slip with good agreement to experimental data. This works on the same idea as Davis & Hill 1992 [18] but for the different system of two spheres of equal radii rather than differing radii and weights. The contact model is more complicated than any that precede it. The model uses two different friction coefficients so that it satisfies Amontonss law.

Galvin (2001) [29] created a model for a sphere with two different roughness heights falling down an inclined plane. Three scenarios were considered: contact with large asperities, contact with small asperities and no contact (particle falling freely after a large asperity). Experimental and theoretical predictions showed good agreement. Galvin concludes that the angle of inclination of the plane affects the level of hydrodynamic roughness felt by the particles. Low angles resulted in the particles falling towards the plane and the small asperities contacting the plane whereas higher angles of inclination resulted in the large asperities being the dominant roughness height.

Zhao, Galvin, Davis 2002 [69] considered a sphere rolling down a plane but considered the roughness to be on the plane rather than on the sphere as in Galvin (2001) [29]. Rotational velocity was roughly constant with varied

separation but the translational velocity decreased weakly as the particle fell towards the plane. It was shown that separation is affected by the size of the asperities on the spheres and a coefficient of friction. A roll-slip model was show to be more accurate than other hypotheses, in agreement with Zeng et al. (1996) [68]. Experimental and theoretical results showed good agreement.
Wilson and Davis, 2000 [63], consider a dilute solution of equally sized spheres. Shearing and straining motions are considered. They use the roll slip model introduced by Davis in [17], and Brownian motion is neglected. They calculated the pair distribution function. In axisymmetric straining flows, surface roughness and increasing the coefficient of friction between particle are both show to decrease viscosity (although the latter result is an error, corrected in [64]). It was found that larger roughness heights caused a decrease in viscosity in dilute suspensions, this is thought to be because the spheres can't get arbitrarily close together, limiting any lubrication stresses. In shear flow the two normal stress differences are considered and nonzero values of both may be caused by particle contact.
Wilson and Davis, 2002 [64], consider a shear flow in a monolayer and the effect of particle roughness on stress. The same model roll slip model was used as in [63]. For non dilute systems viscosity was shown to be dependent on the frictional coefficient. Viscosity was shown to decrease with increasing roughness height, results which are consistent with 3D dilute calculations in [63]. Frictional coefficients was found to have a limited effect on viscosity but a small increase was shown at higher concentration due to particles being in contact with more than one other particle at any time. The first normal stress difference N_1 was shown not to be dependent on frictional coefficient but was dependant on roughness, becoming more negative with increased roughness height. The trend was reversed for more concentrated systems.
Wilson 2003 [62] considers the effect of rough spheres on pair distribution functions in a dilute suspension undergoing a plane strain flow. Viscosity is shown to decrease with roughness height as found in previous calculations

[63],[64]. The observation of a more negative normal stress with increased roughness height was also consistent for a dilute system. The effect of small Brownian motion is also considered giving agreement with Brady and Morris [12].

A review of work by Davis, Galvin, Zhao and Wilson was undertaken in 2005 [19] summarising the results.

4.2 Hard Contact Model

In our work, two models are considered for interparticle contact. One is a soft contact model whereby we imagine the spheres being covered in squishy asperities, discussed in section 4.3; in the other, hard contact model, the surface has hard asperities: see figure 4.2. In each case the asperities are considered sufficiently sparse as not to affect the hydrodynamic interaction between the spheres.

The different existing models of contact, which all use some form of hard contact, are discussed by Davis [17] and da Cunha [15]: pure hard sphere repulsion, roll-slip, and stick-rotate. As mentioned in the literature survey, Zeng et al. [68] found roll-slip to be a more realistic model than stick-rotate. The model we will use is the pure hard-sphere repulsion, which is a special case of the roll-slip model with no friction coefficient. The contacts produce only a force normal to the particle surfaces. In shear flow Wilson and Davis [63] and Davis, Zhao and Wilson [19] predicted that the details of the normal force have a more dramatic effect on rheology than the tangential friction force, when in a hydrodynamically driven flow.

We are neglecting tangential forces, which means neglecting any torque exerted by the contact forces. This clearly reduces complexity from a computational point of view; physically, little is lost in terms of accuracy. Figure 4 on page 353 of Wilson and Davis 2000 [63] shows the effect of including torques into one contact model: it makes little difference to the suspension rheology. Although

the model used in that paper is for hard contact we shall also only use a line of centres force for soft contact too. This allows us to compare the two models in a clearer fashion as well as test the soft contact model as it is a newer model.

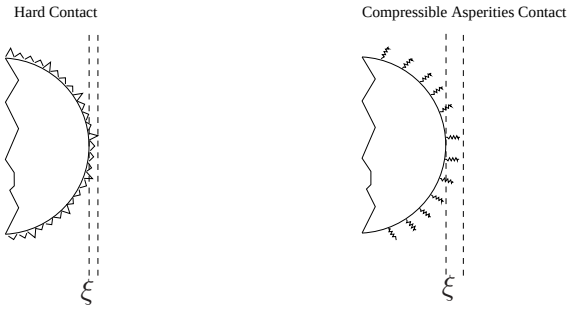

Figure 4.2: Hard and soft contact with ξ roughness height

4.3 Compressible Asperities

4.3.1 Background Theory

In 1989, Smart [54] introduced a new experiment to determine the separation between a sphere and a horizontal plane by measuring the time taken for the sphere to leave the plane when the container is inverted. Galvin et al [29] adapted this technique in 2001 to study a sphere travelling down an inclined plane. They observed a larger effective roughness height when the plane was inclined further from the horizontal, and use a model of differing length asperities to explain this phenomenon.

Galvin's model was that of a sphere with two sets of different length asperities, small and large. The larger asperities were widely spaced such that on an inclined plane, the sphere could rest solely on the small asperities but would then roll onto the larger asperities. Tangential friction was also included in their model. The steeper the plane, the less normal force was created, but the larger the effect of tangential friction. They compared their model with

experiments, and extracted fit values for four parameters: the two roughness heights, the separation between large asperities, and the friction coefficient. During a conference in Warsaw in 2004 [65] Wilson proposed an alternative mechanism to describe this behaviour. Instead of relying on contact with different length asperities it was proposed that the surface asperities might be considered as small springs. We extend that work here.

4.3.2 Force Law

We describe the contact model in terms of a nominal surface roughness height ξ and the particle surface separation ζ. The roughness height acts such that the first contact of a particle surface with a roughness asperity is when $\zeta = \xi$. Thus if $\zeta > \xi$ no contact force acts.

Wilson [65] used the data from figures 10 and 11 of Galvin et al [29], which plot measured average separation between the sphere and the plane, ζ, against the inclination angle, θ, and attempted to fit them with a nonlinear spring law $F(\zeta)$ for the force exerted by the compressible asperities. This can be seen in figure 4.3. The data are reformulated as $F = m^* g \cos\theta$, the effective normal force acting on the sphere (where m^* is the particle's mass adjusted for buoyancy). Since $F = 0$ at $\theta = \pi/2$, a fit to the data is expected to yield a value $\zeta = \xi$ at which $F = 0$, giving the length of asperities or roughness height.

The presentation in Warsaw suggested a simple Hooke's law, but this was found to be too weak at close separations. In more recent work (unpublished), Wilson found that a cubic function produced the best fit:

$$G(F) = \log(\zeta) = aF^3 + bF^2 + cF + d. \tag{4.1}$$

where ζ is the separation. Since we need the repulsive spring force to be a monotonic decreasing function of separation for $\zeta \leq \xi$, we have the requirement

$$G'(F) < 0, \qquad \forall\, F > 0, \tag{4.2}$$

This quadratic condition ($3aF^2 + 2bF + c < 0$ in $F > 0$) implies

$$a < 0 \quad \text{and either} \quad \{b < 0 \text{ and } c < 0\} \quad \text{or} \quad \left\{b > 0 \text{ and } c < b^2/(3a)\right\}. \tag{4.3}$$

This is a spring law but obviously more complicated than the simple Hooke's law proposed in Warsaw [65] . An optimisation routine was used to ascertain the parameter values. This three step process involved:

1. First optimise without constraint.
2. If any of the constraints is violated, Lagrange's method is used to solve for equality on that constraint.
3. Re-check that the other constraints are still satisfied and repeat if necessary.

Optimising without constraint works well with the data from figure 11 of Galvin et al [29], giving the following parameters:

$$a = -0.556, \quad b = 0.594, \quad c = -0.678, \quad d = -5.672. \tag{4.4}$$

A naive optimisation using the data from figure 10, however, produces coefficients with $b > 0$ which violate the constraint $c < b^2/3a$.
To illustrate the method we will do an example of the Lagrange's multiplier method for the constraint $c < b^2/(3a)$ for $b > 0$. We aim to minimise

$$f(a, b, c, d) = \sum_i^n \left(aF^3 + bF^2 + cF + d - \log\left[\zeta(F)\right]\right)^2, \tag{4.5}$$

the sum is over all of the data points of ζ and the square is to make all differences positive. The relevant constraint is rewritten

$$g(a, b, c, d) = b^2 - 3ac \leq 0 \tag{4.6}$$

Taking gradients of each function in the vector space of coefficient sets (a, b, c, d), we set

$$\nabla f = \lambda \nabla g \text{ and } g = 0, \tag{4.7}$$

resulting in the system

$$\begin{aligned}
&\sum_i^n 2\left(aF^3 + bF^2 + cF + d - \log\zeta(F)\right)F^3 = -3\lambda c \\
&\sum_i^n 2\left(aF^3 + bF^2 + cF + d - \log\zeta(F)\right)F^2 = 2\lambda b \\
&\sum_i^n 2\left(aF^3 + bF^2 + cF + d - \log\zeta(F)\right)F = -3\lambda a \\
&\sum_i^n 2\left(aF^3 + bF^2 + cF + d - \log\zeta(F)\right) = 0 \\
&b^2 - 3ac = 0.
\end{aligned} \tag{4.8}$$

Letting

$$l_j = \sum_i^n F^j \log\xi(F) \tag{4.9}$$

and

$$m_j = \sum_i^n F^j, \tag{4.10}$$

then we can write

$$\begin{aligned}
&am_6 + bm_5 + cm_4 + dm_3 - l_3 = -3\lambda c/2 \\
&am_5 + bm_4 + cm_3 + dm_2 - l_2 = \lambda b \\
&am_4 + bm_3 + cm_2 + dm_1 - l_1 = -3\lambda a/2 \\
&am_3 + bm_2 + cm_1 + dm_0 - l_0 = 0 \\
&b^2 - 3ac = 0.
\end{aligned} \tag{4.11}$$

Then using the data we can solve for a, b, c and d. For figure 10 of Galvin [29], this results in

$$a = -12.754, \quad b = 14.909, \quad c = -5.809, \quad d = -5.419. \tag{4.12}$$

The form of the function that has been calculated is

$$G(F) = \log \zeta = aF^3 + bF^2 + cF + d \tag{4.13}$$

which requires inverting to obtain the quantity we want of the retardation force. This is done simply by using the cubic formula and choosing the real solution. There is only one real solution due to the parameter choices of $b > 0, b^2 - 3ac \leq 0$. These results are show in (4.12) and (4.4). The d parameter is related to the roughness height we are modelling: when the particles are just touching due to surface roughness, at $\zeta = \xi$, the force $F = 0$, so at that point we have

$$\log(\xi) = d \qquad \xi = e^d \tag{4.14}$$

which gives us roughness height $\xi_r = 0.0044$ for figure 10 of Galvin [29] and $\xi_r = 0.0034$ for figure 11. These roughness heights do not match Galvin's fits exactly; they are however of the correct order of magnitude.

Force Factor

The force law outlined in section 4.3.2 gives as a function for the force which matches Galvin's force data in terms of the angle of inclination of the plane. The angle can be converted into a force via

$$F = mg \cos \theta \tag{4.15}$$

where m is the difference in mass between the fluid and particle of the same volume. If we look at the fit of the force law using the results calculated in section 4.3.2 shown in table 4.1 we can see that the fit for figures 10 and 11 4.3 of Galvin's data is very good.

The results compare well with Galvin's own fit shown in figure 4.3 but they were constrained by their assumptions about the physics such as the different length asperities.

However these results are a real, fully dimensioned quantity. Our model is non-dimensionalised using the fluid viscosity μ, the particle radius a, and a

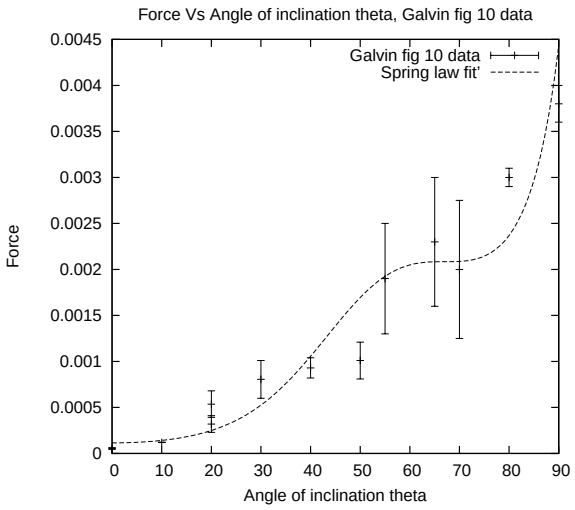

(a) Fit of spring law on Galvin's fig 10 data

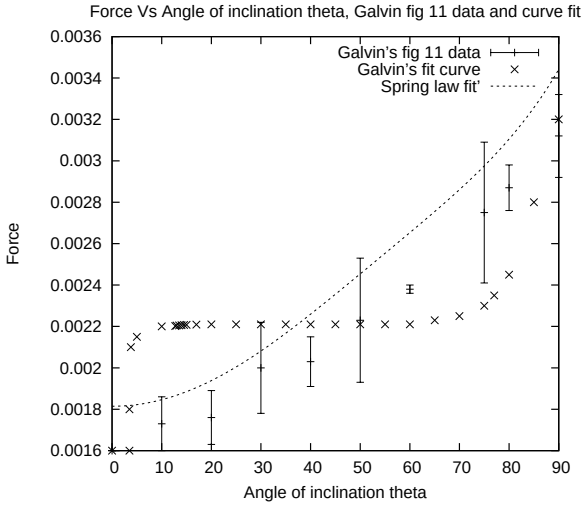

(b) Spring law curve fit, Galvin's fig 11 with fit

Figure 4.3: Fit of spring law on Galvin's fig 10 & 11 data

typical rate of strain $\dot{\gamma}$. Thus a dimensionless force F is given by

$$F = \frac{m^* g}{\mu \dot{\gamma} a^2} C \equiv ff C \tag{4.16}$$

where ff is a dimensionless variable, the force factor and C is $\cos\theta$. Small values of ff are applicable to strong flows or weak interparticle forces: thus, using small values allows us to look at situations where the particles are close to smooth.

Considering three different ff values our spring law graphs appear as in figure 4.4.

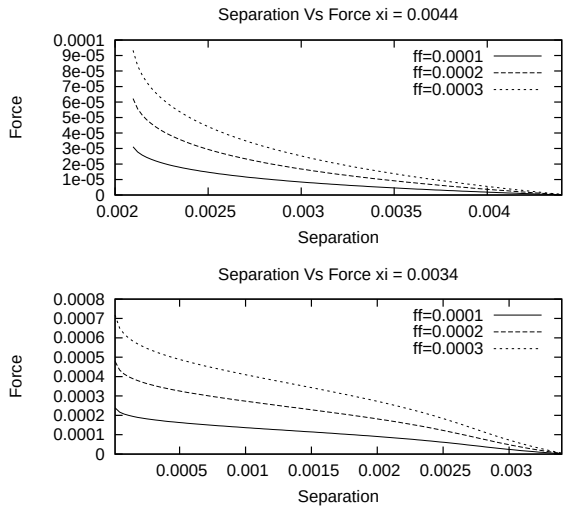

Figure 4.4: Graph of force function for two different asperity heights. Top $\xi = 0.0034$, (Galvin figure 11), bottom graph $\xi = 0.0044$, (Galvin figure 10).

In figure 4.4 we show the spring law graphs (force plotted against surface separation) for three different values of ff. The two graphs are from the

parameters we derived above, to match the data from figures 10 (with $\zeta = 0.0044$) and 11 (with $\zeta = 0.0034$) of [29]. The full list of parameters is shown in table 4.1. In each case the graph is monotonic decreasing from an asymptote at small separations (given by $F \sim (\log \zeta/a)^{1/3}$) to zero at the nominal surface roughness height $\zeta = \xi = e^d$. For most separations the effect of changing ff is more dramatic than changing the particle separation.

Parameter	Values matching figure 10	Values matching figure 11
a	-12.754	-0.556
b	14.909	0.594
c	-5.809	-0.678
d	-5.419	-5.672
$\xi = e^d$	0.0044	0.0034

Table 4.1: Parameter values for compressible asperities model matching Galvin [29] figure 10 and 11 found via Lagrange's Method

4.4 Rough Sphere Programming Alterations

The alterations for rough spheres were relatively minor. The main contribution was to a force vector.

Soft contact simply involved a small subroutine which calculated the force vector from the separation. Hard contact was a little more complicated. This required on setting the force vector but also tracking particles when nearly touching. The vector is non-zero only when particles would move towards each other under purely hydrodynamic forces, and the force would depend on this approach velocity. The hard contact model implemented in this simulation was a fuller model with contact force depending on the relative approach vectors, this was the same as being used in and Wilson Davis [63],[64], rather than being a simple step function as used in Brady Morris [12] (which also includes Brownian motion).

During the simulation a simple contact algorithm could be

if particles are just touching **then**

contact force is applied

end if

move particles according to all hydrodynamic and contact forces.

Ideally the contact force will result in a zero normal velocity, however due to the discrete nature of a computer program the normal approach velocity is never quite exactly zero at contact. If the normal velocity is slightly positive the particles will still stay in contact but overlap slightly and their position will be corrected at the next time step. If the velocity is slightly negative, though, the particles will drift apart, no longer being in contact at the next time step. The following time step will see them move closer again due to the fluid flow that previously pushed the two particles into contact. The result will be a particle that keeps on 'bumping' in and out of contacts only due to numerical noise rather than a mathematical reason. Instead a more complex algorithm is used.

if (separation $<$ 1.01 roughness height) && (normal approach velocity is $>$ 0) **then**

contact force is applied

end if

move particles according to all hydrodynamic and contact forces.

set positions so that distance between particle = 1 roughness height.

This numerical fudge helps ensure that the false separation and 'bouncing' does not occur.

4.5 Rough sphere parameter values

The concentration values were $c = 0.1$, 0.3, 0.5, 0.6 and 0.7 and the flow parameters, $\beta = 0.1$, 0.3, 0.45, 0.55 and 0.7. For hard contact we used roughness heights $\xi = 10^{-2}$ and 10^{-3}; for soft contact we used the parameters we extracted in section 4.3.2, which are shown in table 4.1.

4.6 Hard Contact

We first look at the hard contact model. We seeded with $n = 30$ particles and ran for 30 repetitions of the periodic box in each case.

4.6.1 Validation

There have been two main groups who have run hard contact simulation models. Brady and Morris [12] used a hard contact model but also included Brownian motion in their system. The hard contact model utilized by their simulation was a simple Heaviside step function of constant magnitude. The magnitude of the contact force on our model is related to the approaching velocity vector between the two particles. Validation of our implementation of the hard contact model comes via reproducing figure 4(a) on page 438 of Wilson and Davis 2002 [64], which is shown in figure 4.5. Their computations are carried out in shear flow, which would be represented by $\beta = 0.5$ in our formulation, however our basis fails at this point so we have done a flow very close to this with a hint of strain with $\beta = 0.55$.

Comparing figure 4.5 to fig 4 in Wilson 2001 [64] we can see a relatively good agreement in our results. There is some deviation at the higher concentration of $c = 0.6$ where higher viscosities are found with the small addition of the rotation accounting for the slightly larger viscosity.

We can also validate against our own earlier work for smooth spheres by a direct comparison of the results at $\beta = 0.55$, as shown in figure 4.6. For high

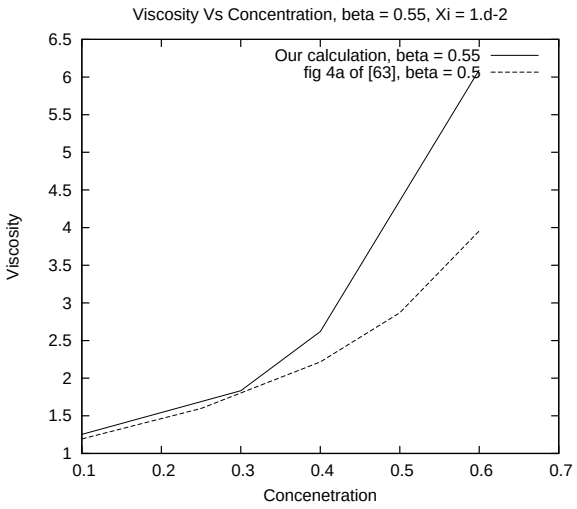

Figure 4.5: Viscosity *vs* Concentration, $\beta = 0.55$, $\xi = 10^{-2}$

concentrations the smooth sphere runs experienced crystallisation problems, so we plot those results for concentrations up to 0.4 only. We see that, at low concentrations, the roughness (with a roughness height of $\xi = 10^{-2}$) has a very weak effect on the overall viscosity, but it does lower the viscosity (as predicted in Wilson and Davis, 2000 [63] and others). At a crossover concentration of 0.4 the roughness appears to slightly increase the viscosity, also in agreement with the literature.

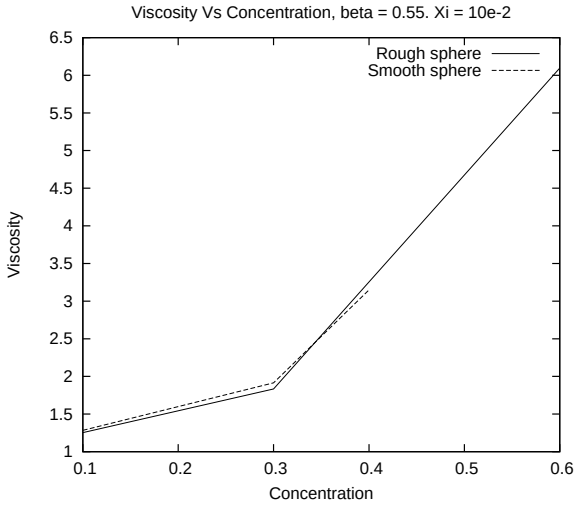

Figure 4.6: Viscosity *vs* Concentration, $\beta = 0.55$, $\xi = 10^{-2}$ and smooth spheres comparison

4.6.2 Runtime issues

A series of runs for hard contact were undertaken at various concentrations and for various flows. Unfortunately the vast majority of these runs failed in part of the code that takes care of the bouncing of the spheres. This could possibly be solved with a smaller time step although it may also just result in the same jamming but at a later date. The code fails to complete because it gets stuck in a particle position correction routine called correct_particles.

The problem arise when the particles positions are adjusted. The positions are adjusted on a pair wise method iterating between every pair combination

repeating until there are no overlaps. This works well at low concentrations but if particles cluster due to either the flow or just high concentrations then the algorithm gets stuck in an infinite loop.

During many of the runs we experienced freezing of the code where corrections to any overlapping particle could not be achieved. We will now consider what cases failed and what cases ran to completion. Following on from this we shall consider draw conclusions from the completed runs as to the nature of the numerical fail and comment on any possible micro structure which have formed. There tended to be more completed from the smaller roughness

Concentration	
$c = 0.1$	All runs completed
$c = 0.3$	$\beta = 0.1$ and $\beta > 0.5$ completed.
$c = 0.5$	$\beta = 0.7$ completed.

Table 4.2: Completed hard contact runs, $\xi = 10^{-3}$

Concentration	
$c = 0.1$	All runs completed
$c = 0.3$	$\beta < 0.5$ failed. $\beta > 0.5$ completed.
$c = 0.5$	$\beta = 0.7$ completed.

Table 4.3: Completed hard contact runs, $\xi = 10^{-2}$

height $\xi = 10^{-3}$ too, is probably due to the reduced size felt by the fluid and hence a smaller effective concentration.

4.6.3 Discussion of Results

Low Concentrations

The smooth sphere results detailed in chapter 3 showed an exponential type relationship between concentration and viscosity. Crystallization and the resultant velocity spikes occurred at higher concentrations. This phenomenon

was more noticeable at flows approaching shear, $\beta = 0.5$, with strain and rotational flows showing a lower viscosity for the same concentration.

Recalling that $\beta = 0$ strain flow, $\beta = 1$ solid body, rotation it is clear that the hard contact code does not like flows with a strain component, this is somewhat different than the case for smooth spheres. This could be because fluid exerting a force pushing the particle together rather than just sliding past each other in bands or rotating in some sort of near solid body rotation. We can not use the parameter values for the best fit to analyse the data as we have done in the smooth sphere case as the form of the results is not the same.

This can be seen by looking at 4.7 where we can see that the viscosity does not begin to converge within 30 box repetitions which is at stark contrast to smooth results which centred around a level value.

In figure 4.7(b) we see the transient viscosity for hard spheres with a roughness height of 10^{-2} at a concentration of 0.1 and in a flow close to strain at $\beta = 0.1$. The viscosity rises throughout the plot, reaching a value of around 2.1 at time 30. By contrast, in figure 4.8, which is for the same parameters as figure 4.7(b) except for the roughness height of 10^{-3}, the viscosity rises more slowly and reaches only 1.7 in the same time. If we view figure (the same parameters, but for smooth spheres, where the viscosity rises only briefly and stabilises around 1.3) as the extension of these results to zero roughness height, we are extrapolating a trend of increasing roughness height causing an increase in viscosity. This is in contrast to Wilson and Davis [63], who showed a reduction in viscosity due to surface roughness at low concentrations.

Looking at flows closer to shear, $\beta = 0.45$ the viscosity take on a more normal shape, figures 4.9 and 4.10. The larger asperities here giving rise to a slightly lower viscosity but not significantly. A terminal viscosity of 1.37 for $\xi = 10^{-2}$ with a standard deviation of 0.79 and 1.39 with a standard deviation of 0.80 for $\xi = 10^{-3}$ was recorded. This result is slightly higher than that recorded for smooth spheres, 1.35. Considering a fluid flow closer to rotation, $\beta = 0.7$ for

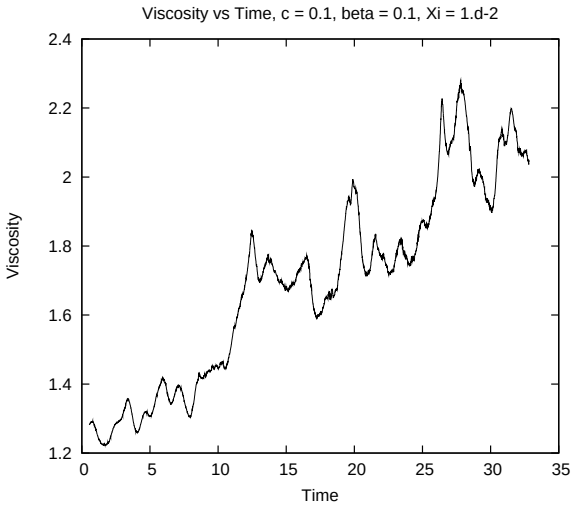

(a) Rough Spheres

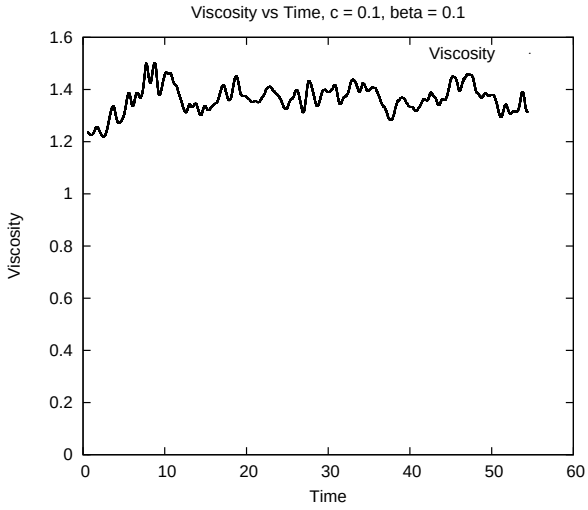

(b) Smooth Spheres

Figure 4.7: Viscosity $c = 0.1$, $\beta = 0.1$, $\xi = 10^{-2}$

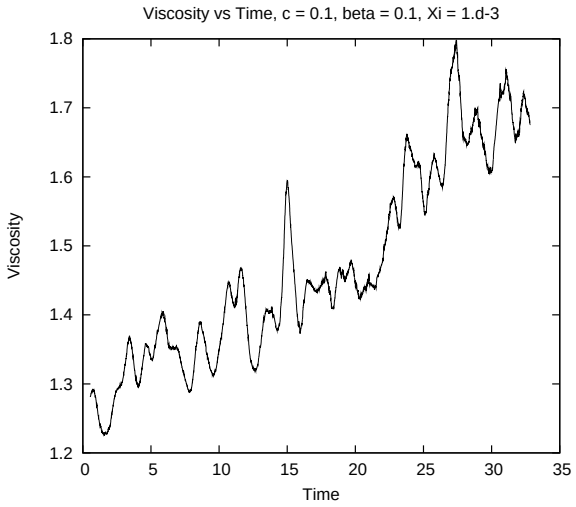

Figure 4.8: Viscosity $c = 0.1$, $\beta = 0.1$, $\xi = 10^{-3}$

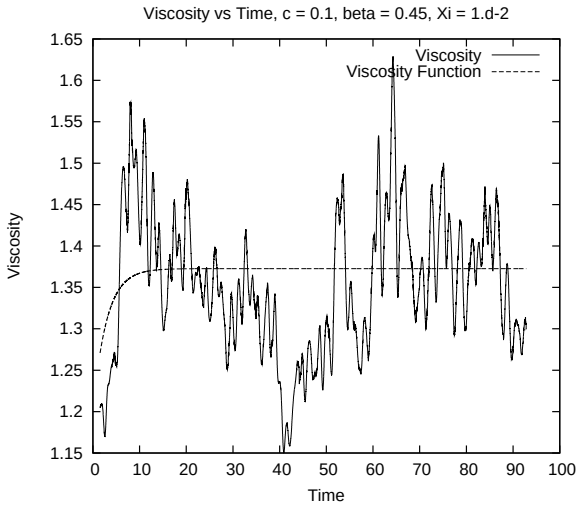

Figure 4.9: Viscosity $c = 0.1$, $\beta = 0.45$, $\xi = 10^{-2}$

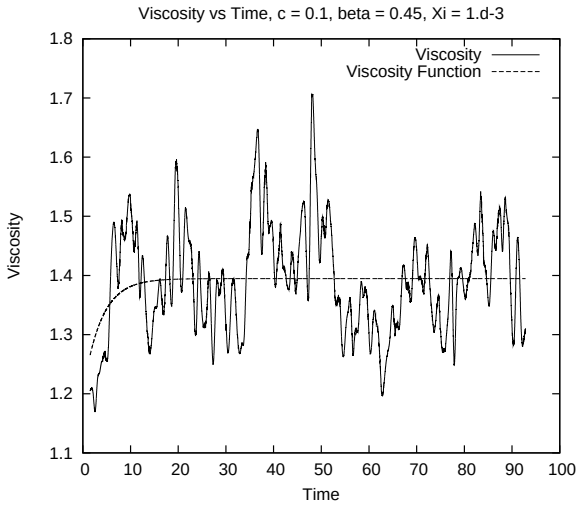

Figure 4.10: Viscosity $c = 0.1$, $\beta = 0.45$, $\xi = 10^{-3}$

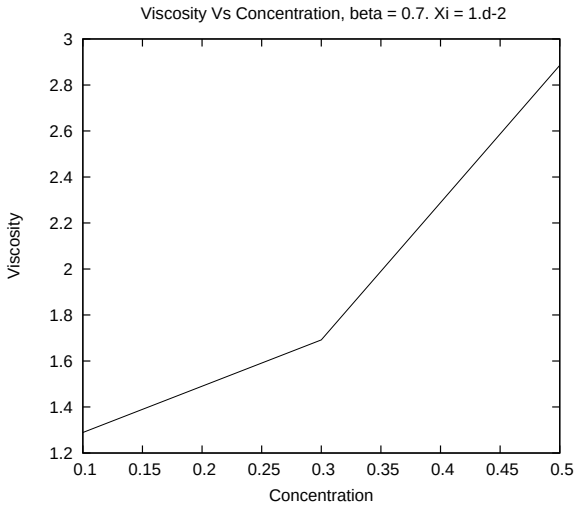

Figure 4.11: Viscosity *vs* Concentration $\beta = 0.7$, $\xi = 10^{-2}$

$\xi = 10^{-3}$ gave a terminal viscosity of 1.33 with a standard deviation of 0.77. Comparing to the static results we have $\beta = 0.65$ gave a terminal viscosity of 1.26 and for $\beta = 0.75$ gave a terminal viscosity of 2.97; interpolating these results gives us a viscosity of 2.115 for $\beta = 0.7$. This lower viscosity in comparison to the smooth particles as lower concentration is in agreement with the literature. This lower viscosity exists in a flow approaching solid body rotation due to the lesser amount of movement of adjacent particle within the fluid and consistant with our earlier results. The effect of concentration can be seen in figure 4.11.

High Concentrations

Considering higher concentrations we are more restricted due to the failings of many of the simulations outlined in table 4.2. It is clear from table 4.2 that the simulation does no cope well with flows near strain. Indeed, even at very

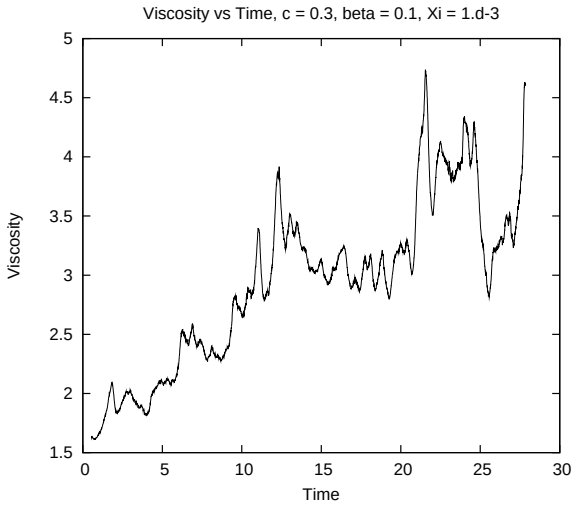

Figure 4.12: Averaged Viscosity $c = 0.3$, $\beta = 0.1$, $\xi = 10^{-3}$

low concentrations (as seen in figure 4.8, $c = 0.1$) we saw that the viscosity climbs sharply and does not converge for these straining flows. This can be seen again on some partial data for $c = 0.3$, figure 4.12.

First Normal Stress Difference

In simple shear $\mathbf{u}^{\infty} = (\dot{\gamma}y, 0)$, the first normal stress difference N_1 is the difference between the two diagonal fluid stresses $\sigma_{11} - \sigma_{22}$. A positive normal stress results in the Weissenberg effect where by a fluid climbs a rotating rod. The results for the first normal stress difference were noisy just as they had been in the smooth sphere case. The results hovered around $N_1 = 0 \pm 1.97\times$ Sd, (standard deviation), meaning that they were within a 95% confidence interval of zero. Considering this it it hard to draw any real conclusion from the first normal stress difference results for hard contact. This is actually true across both true across both hard contact and the compressible asperities contact model.

4.6.4 Tabulated rough sphere results

Tabulated results of the runs for terminal viscosity, and their respective standard deviations. Results in bold represent runs that did not reach a stable viscosity such those shown in figure 4.12.

c	$\beta = 0.1$	$\beta = 0.3$	$\beta = 0.45$	$\beta = 0.55$	$\beta = 0.7$
0.1	**2.05248**	**1.69418**	1.37266	1.25370	1.28909
0.3	–	–	–	1.83276	1.69175
0.5	–	–	–	–	2.88504

Table 4.4: Terminal viscosity, $\beta = 0.1 - 0.7$, $\xi = 10^{-2}$

c	$\beta = 0.1$	$\beta = 0.3$	$\beta = 0.45$	$\beta = 0.55$	$\beta = 0.7$
0.1	**1.18476**	**0.977921**	0.792478	0.723824	0.744257
0.3	–	–	–	1.05812	0.976688
0.5	–	–	–	–	1.66560

Table 4.5: Terminal viscosity standard deviation, $\beta = 0.1 - 0.7$, $\xi = 10^{-2}$.

c	$\beta = 0.1$	$\beta = 0.3$	$\beta = 0.45$	$\beta = 0.55$	$\beta = 0.7$
0.1	**1.66685**	**1.62768**	1.39468	1.26904	1.33247
0.3	**3.74617**	–	–	1.74062	1.86567
0.5	–	–	–	–	3.06010

Table 4.6: Terminal viscosity, $\beta = 0.1 - 0.7$, $\xi = 10^{-3}$

c	$\beta = 0.1$	$\beta = 0.3$	$\beta = 0.45$	$\beta = 0.55$	$\beta = 0.7$
0.1	**0.962358**	**0.939674**	0.805131	0.732664	0.769268
0.3	**2.16233**	–	–	1.00493	1.07710
0.5	–	–	–	–	1.76667

Table 4.7: Terminal viscosity standard deviation, $\beta = 0.1 - 0.7$, $\xi = 10^{-3}$.

4.7 Rough Spheres, Compressible Asperities

4.7.1 Compressible Asperities

Considering compressible asperities, as described in section 4.3.2, where we derived our force law from a fit to published experimental data (two data sets yielding two separate fits) and were left with one additional dimensionless parameter to describe the strength of the interparticle force relative to hydrodynamic forces, which we denote as ff. Because of numerical difficulties (described later in this section) we were restricted to rather weak forces (or strong flows), with a maximum force factor of 0.003.

For each of the parameter combinations given in table 4.8 (and the corresponding force law parameters from table 4.1) three runs were done with $n = 30$ particles in a box, for 30 repetitions of the box.

Parameter	Values
Concentration c	0.1, 0.3, 0.5, 0.7
Surface roughness ξ	0.0034, 0.0044
Shear ratio β	0.1, 0.3, 0.45, 0.55, 0.7
Force factor ff	0.001, 0.002, 0.003

Table 4.8: Combinations of squishy runs

Surface roughness shows a limited but still significant effect on terminal viscosity, this effect is most pronounced at high concentrations.

Viscosity

When we compare our terminal viscosity results with the equivalent results for smooth spheres, the results are consistent with the literature. We see higher viscosities at higher concentrations (where the particles seem larger than if they were smooth). This can be seen in figure 4.13. The cross over point appears to be at approximately $c = 0.6$. This can be seen again on figure

4.20, but with the crossing over appearing at slightly lower concentration, the highest valid concentration this set of run ran for was $c = 0.6$ hence the still visible but less pronounced higher viscosities than show in figure 4.13. The literature also shows slightly lower viscosities due to roughness at low concentrations (because of the reduction in lubrication stresses), however this is less apparent in the close to straining flow of $\beta = 0.1$ but more so for $\beta = 0.3$ shown in figure 4.20 except for the case where $ff = 0.003$. This may be due to the fact that as we approach shear, viscosities overall become greater, therefore the the rough contact force becomes less significant.

The different roughness heights seemed to show little effect to the overall viscosity except for at the highest concentrations. The differences at the higher concentrations can be seen in figure 4.14.

During the computation, many of the runs, particularly those at the rotation end of the strain–shear–rotation spectrum, produced data that were not suitable to be analysed using our curve fitting (or in some cases were unphysical). The two situations occurring were,

1. crystallization
2. Viscosities less than the Einstein value of $1 + \frac{5}{3}c$.

The first situation is one that also occurred in the smooth sphere runs. Jamming occurs because of the higher viscosities at non-dilute concentrations. This obviously is a sign of crystallization to occurring earlier on rough sphere than smooth spheres as higher concentrations. The crystallization results in extremely large viscosity values, this is a physical situation which occurs in suspensions.

The second, unphysical, situation is a problem where the viscosities are less than the Einstein value. This occurs due to the extra force felt on the particle due to the inter-particle contact the particle moves too much during a time step. This results in a particle overlap. This overlap produces garbage when input into the hydrodynamic functions. The particle overlap, in turn, may be

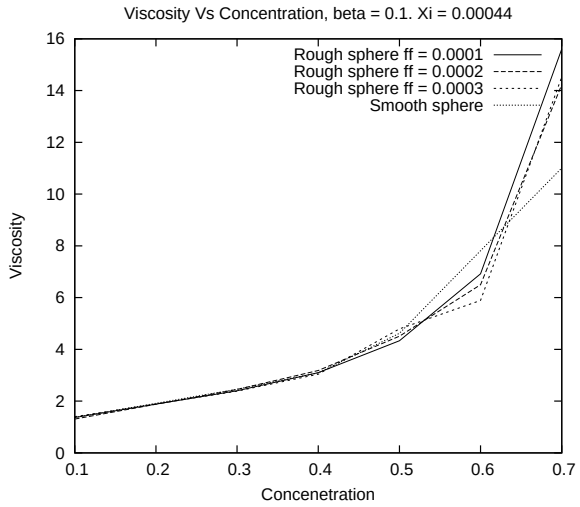

Figure 4.13: Graph of Viscosity against concentration, $\beta = 0.1$

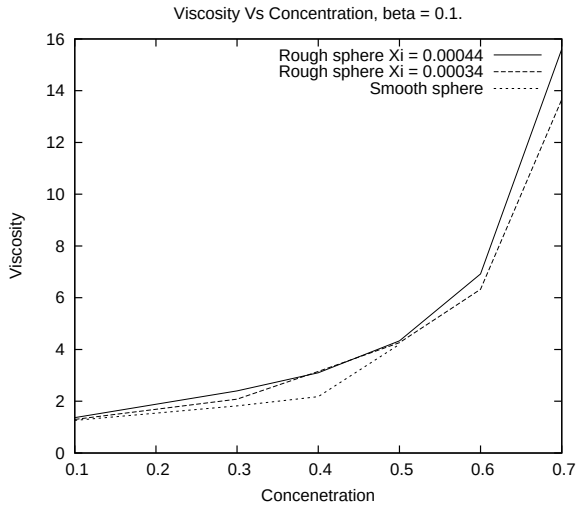

Figure 4.14: Graph of Viscosity against concentration, $\beta = 0.1$, comparing ξ.

avoided by taking smaller timesteps: it is a symptom of particles moving from separated to overlapping without feeling the lubrication forces associated with very close pairs. However, our timestep is already 5×10^{-4}, and to reduce it further would be prohibitive in terms of computational time needed to see meaningful results.

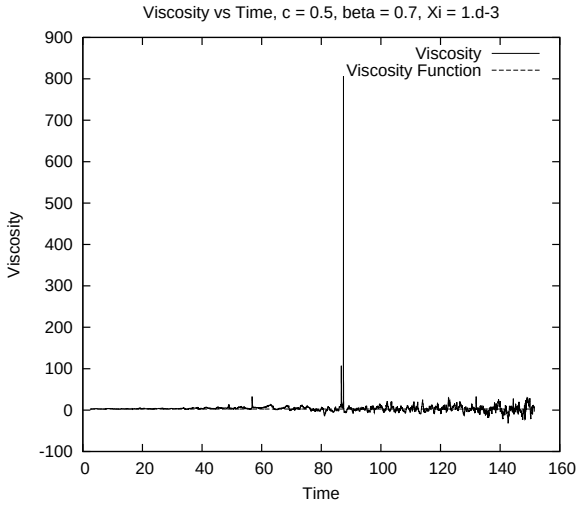

Figure 4.15: Graph of Viscosity against time $ff = 0.0001$, $c = 0.5$, $\beta = 0.1$

Both of these problems can be seen in figure 4.15. At time $T \approx 90$ there is a clear viscosity spike indicating the jamming occurring. Although hard to make out from this graph it is also possible to see the occurrence of a negative viscosity around $T \approx 140$.

Physically, we expect that this problem is also restricted to scenarios very close to jamming: indeed, this phenomenon has been observed by Melrose et al 1997 [26] and Dratler and Schowalter 1996 [20] for concentrated suspensions. So, unsatisfactory as it may be, we have two numerical difficulties which both suggest that the physical system we are studying is close to jamming, or crystallising. Despite this there are still further conclusions that can be made from the remaining results.

The effect of flow type on viscosity of smooth particle compared to particles

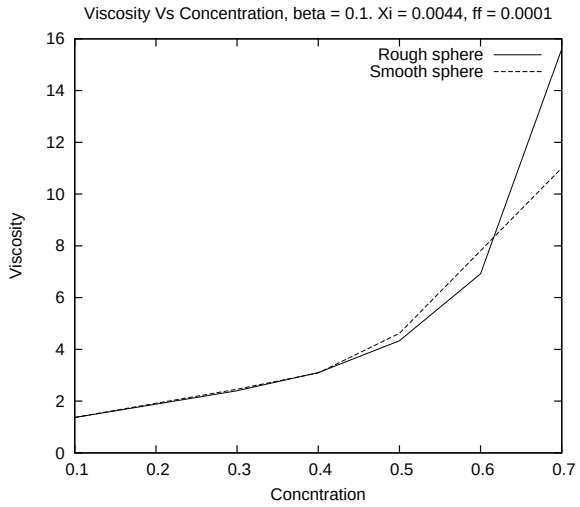

Figure 4.16: Graph of Viscosity *vs* Concentration $ff = 0.0001$, $\beta = 0.1$

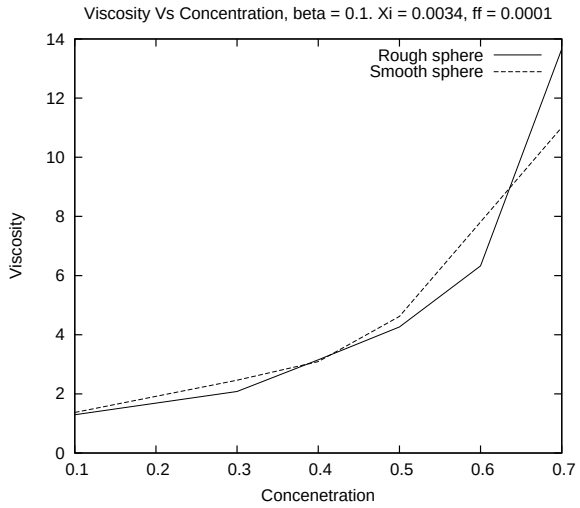

Figure 4.17: Graph of Viscosity *vs* Concentration $ff = 0.0001$, $\beta = 0.1$

with surface roughness is minimal in absolute terms, but the flow does affect the onset of crystallisation. This is consistent with the results found in section 3.5. The hard contact model showed greater rates of failure for flow with large amounts of strain, resulting in the program getting stuck due to overlapping particles. The smooth sphere results produced results with very high viscosity spikes as flow closer to shear suggesting crystallization; the compressible asperities model results were similar with the volatility and order of the viscosity increasing with flows approaching shear. We can see this increased volatility in 4.18 in comparison with 4.19. The peak viscosities are however somewhat lower than that of the smooth sphere case, figure 3.9; this is consistent with the hypnosis that the surface roughness produces slightly lower viscosities at lower concentrations. However before crystallization occurs the viscosities on the rough sphere model appear to be slightly lower the onset of crystallisation occurs at approximately the same point. Taking $c = 0.4$ as an example the progression from $\beta = 0.45$ to $\beta = 0.55$ result in extreme spike viscosities suggestion crystallization in both smooth sphere results and the compressible asperities model. Further mirroring the smooth sphere results the viscosity drops back again for flow approaching rotation. Without further research using finer parameter spread it is impossible to say if compressible asperities result in later onset of crystallization; even though pre-crystallization viscosities at lower concentrations are slightly lower when surface roughness is taken into account. A possible hypothesis is that during flows which cause crystallization areas occur where local concentration is higher than global concentration; therefore any viscosity reduction that found be felt at lower concentrations are mitigated by the local higher concentrations at which point the asperities become a hindrance in terms of particles passing. In figure 4.20 we show the graphs of viscosity against concentration for both smooth spheres and rough spheres with a force factor of $ff = 0.001$, 0.002 and 0.003 for a flow parameter $\beta = 0.3$ and for the fit parameters for Galvin's separation vs angle of inclination with $\xi = 0.0044$. All four graphs are remarkably

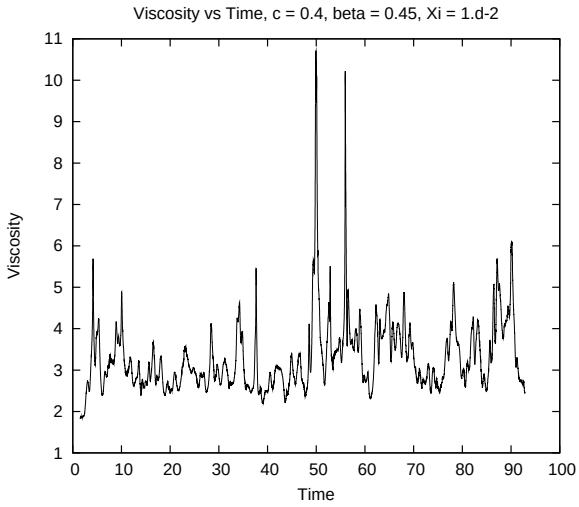

Figure 4.18: Graph of Viscosity *vs* time, $ff = 0.0001$, $\beta = 0.45$, $\xi = 0.0044$

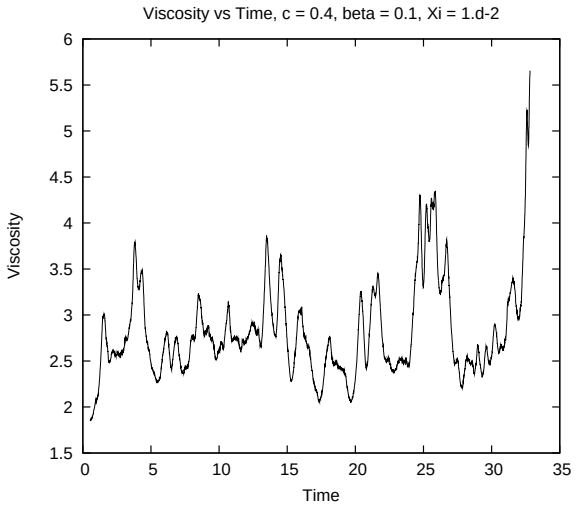

Figure 4.19: Graph of Viscosity *vs* time, $ff = 0.0001$, $\beta = 0.1$, $\xi = 0.0044$

similar, indicating that (at least at these strengths) the contact force does not have a dramatic effect on the fluid rheology. In all viscosity *vs* concentration

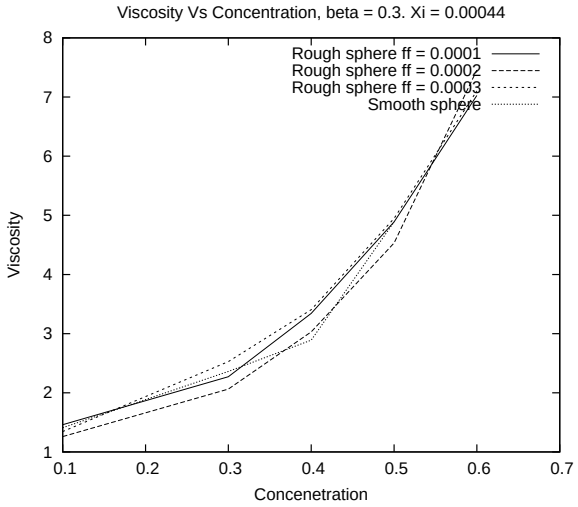

Figure 4.20: Graph of Viscosity *vs* Concentration all ff, $\beta = 0.3$, $\xi = 0.0044$

graphs runs which led to exceptionally high viscosities due to crystallization results have been removed. This is why some graphs only run for concentrations up to $c = 0.5$ as for $c > 0.5$ crystallisation occurred making viewing the graph unproductive.

4.7.2 Tabulated Rough Sphere Results Compressible Asperities

Tabulated results of the runs for terminal viscosity, first normal stress difference and their respective standard deviations.

c	$\beta = 0.1$	$\beta = 0.3$	$\beta = 0.45$	$\beta = 0.55$	$\beta = 0.7$
0.1	1.29563	1.39426	1.36642	1.25018	1.31048
0.3	2.08152	2.80898	2.55698	3899.35	2.11899
0.5	4.26295	5.38853	232662	714807	2.64894
0.6	6.32645	7.08151	633132	2.35324E+6	10.1175
0.7	13.6585	829761	2.63461E+6	3.69309E+6	2.431E+6

Table 4.9: Terminal viscosity, $\beta = 0.1 - 0.7$, $\xi = 0.0034, ff = 0.0001$

c	$\beta = 0.1$	$\beta = 0.3$	$\beta = 0.45$	$\beta = 0.55$	$\beta = 0.7$
0.1	0.748032	0.804915	0.788819	0.721778	0.756572
0.3	1.20177	1.62165	1.47611	2251.24	1.22335
0.5	2.46121	3.11084	134313	412685	1.5293
0.6	3.65258	4.08822	365499	1.35861E+6	5.84106
0.7	7.88571	479028	1.52093E+6	2.13216E+6	1.40348E+6

Table 4.10: Terminal viscosity standard deviation, $\beta = 0.1 - 0.7$, $\xi = 0.0034, ff = 0.0001$

c	$\beta = 0.1$	$\beta = 0.3$	$\beta = 0.45$	$\beta = 0.55$	$\beta = 0.7$
0.1	1.36924	1.46107	1.34769	1.27018	1.3036
0.3	2.4029	2.27113	2.46801	2.63528	1.81245
0.5	4.33539	4.8901	492821	747108	5.79634
0.6	6.91858	7.02623	1.64245E+6	933165	100586
0.7	15.606	809131	3.06597E+6	1.38609E+6	2.15905E+6

Table 4.11: Terminal viscosity, $\beta = 0.1 - 0.7$, $\xi = 0.0044, ff = 0.0001$

c	$\beta = 0.1$	$\beta = 0.3$	$\beta = 0.45$	$\beta = 0.55$	$\beta = 0.7$
0.1	0.79029	0.843488	0.778006	0.733321	0.752601
0.3	1.38731	1.31114	1.42475	1.52145	1.04637
0.5	2.50304	2.8231	284499	431333	3.34637
0.6	3.99444	4.0563	948163	538751	58071
0.7	9.01015	467118	1.76995E+6	800243	1.24647E+6

Table 4.12: Terminal viscosity standard deviation, $\beta = 0.1 - 0.7$, $\xi = 0.0044, ff = 0.0001$

c	$\beta = 0.1$	$\beta = 0.3$	$\beta = 0.45$	$\beta = 0.55$	$\beta = 0.7$
0.1	1.37495	1.54566	1.25099	1.32534	1.28675
0.3	2.50604	2.68653	4.78497	2081.59	2.09312
0.5	3.04573	5.16663	234851	995791	-0.974666
0.6	4.51059	4.98904	894024	1.51612E+6	-13.0934
0.7	15.4149	1.06219E+6	2.58271E+6	2.13944E+6	1.87496E+6

Table 4.13: Terminal viscosity, $\beta = 0.1 - 0.7$, $\xi = 0.0034, ff = 0.0002$

c	$\beta = 0.1$	$\beta = 0.3$	$\beta = 0.45$	$\beta = 0.55$	$\beta = 0.7$
0.1	0.793664	0.892194	0.722233	0.765188	0.742908
0.3	1.44656	1.55073	2.7625	1201.8	1.20846
0.5	1.75809	2.9823	135586	5.7492E+5	0.562724
0.6	2.60366	2.88042	516127	875324	7.55932
0.7	8.89705	613258	1.49102E+6	1.23519E+6	1.08248E+6

Table 4.14: Terminal viscosity standard deviation, $\beta = 0.1 - 0.7$, $\xi = 0.0034, ff = 0.0002$

c	$\beta = 0.1$	$\beta = 0.3$	$\beta = 0.45$	$\beta = 0.55$	$\beta = 0.7$
0.1	1.30743	1.26019	1.29148	1.4247	1.30804
0.3	2.45391	2.0628	2.84091	61412.8	1.91817
0.5	4.51104	4.5319	1.09132E+6	755085	34934.6
0.6	6.49928	7.45554	1.81909E+6	1.09115E+6	30.0422
0.7	14.228	3.7027E+5	1.814E+6	1.28317E+6	1.14664E+6

Table 4.15: Terminal viscosity, $\beta = 0.1 - 0.7$, $\xi = 0.0044, ff = 0.0002$

c	$\beta = 0.1$	$\beta = 0.3$	$\beta = 0.45$	$\beta = 0.55$	$\beta = 0.7$
0.1	0.754769	0.727414	0.74561	0.822551	0.755196
0.3	1.41633	1.19096	1.64008	35456.3	1.10743
0.5	2.60365	2.6165	630029	435944	20169.1
0.6	3.7512	4.30446	1.05017E+6	629971	17.3445
0.7	8.21203	213775	1.04724E+6	740829	661999

Table 4.16: Terminal viscosity standard deviation, $\beta = 0.1 - 0.7$, $\xi = 0.0044, ff = 0.0001$

c	$\beta = 0.1$	$\beta = 0.3$	$\beta = 0.45$	$\beta = 0.55$	$\beta = 0.7$
0.1	1.36619	1.43832	1.36732	-0.188881	1.41015
0.3	2.25925	2.55995	-0.330288	39369.2	3.27281
0.5	4.32165	4.35588	184838	240371	-10.3984
0.6	5.43974	0.0756197	654342	841296	-29.6799
0.7	12.8114	589425	2.66882E+6	2.12867E+6	2.15205E+6

Table 4.17: Terminal viscosity, $\beta = 0.1 - 0.7$, $\xi = 0.0034, ff = 0.0003$

c	$\beta = 0.1$	$\beta = 0.3$	$\beta = 0.45$	$\beta = 0.55$	$\beta = 0.7$
0.1	0.788772	0.830357	0.789337	0.109048	0.814113
0.3	1.30438	1.47788	0.190671	22729.3	1.88947
0.5	2.49511	2.51469	106705	138775	6.00323
0.6	3.14064	0.0436559	377744	485712	17.135
0.7	7.39669	3.4028E+5	1.54067E+6	1.22896E+6	1.24243E+6

Table 4.18: Terminal viscosity standard deviation, $\beta = 0.1 - 0.7$, $\xi = 0.0034, ff = 0.0003$

c	$\beta = 0.1$	$\beta = 0.3$	$\beta = 0.45$	$\beta = 0.55$	$\beta = 0.7$
0.1	1.40121	1.34539	1.6346	2.00899	1.30462
0.3	2.38904	2.52707	1.72569	5.24292	2.66492
0.5	4.79341	4.94784	193424	514094	4.95241
0.6	5.89018	7.10316	2.07725E+6	2.09969E+6	19.6956
0.7	14.5243	3.2778E+5	1.5924E+6	862952	3.00169E+6

Table 4.19: Terminal viscosity, $\beta = 0.1 - 0.7$, $\xi = 0.0044, ff = 0.0003$

c	$\beta = 0.1$	$\beta = 0.3$	$\beta = 0.45$	$\beta = 0.55$	$\beta = 0.7$
0.1	0.808992	0.776703	0.943631	1.15987	0.753187
0.3	1.37931	1.4589	0.996216	3.02694	1.53853
0.5	2.76748	2.85643	111661	296806	2.85915
0.6	3.4007	4.10071	1.19917E+6	1.21223E+6	11.3708
0.7	8.38562	1.8923E+5	919274	498215	1.73295E+6

Table 4.20: Terminal viscosity standard deviation, $\beta = 0.1 - 0.7$, $\xi = 0.0044, ff = 0.0003$

4.8 Conclusion

The model for compressible asperities was a more stable code than the hard contact model producing a wider range and more reliable results. Both models were sensitive to time step however with a already small time step further reduction would be at considerable computational cost.

Hard contact runs agreed well with the literature of Wilson and Davis [63],[64] but due the unsuccessful nature of the runs limited conclusions were possible. Compressible asperities led to more robust results and clearer conclusions. General trends fit with the literature showing a lower viscosity due to particle roughness at low concentration and a higher viscosity and jamming occurrence at high concentration. However the lower viscosity effect at low concentrations was less pronounced was the flow moved towards shear. Normal stress continued to be a noisy data source with standard deviation frequently of the same order as the signal.

The onset of crystallisation was shown to occur earlier as flows moved from strain to shear, just as it did in the smooth sphere case. In the literature for shear flows, the crossover concentration between the dilute regime, where roughness lowers the viscosity, and the concentrated regime, where viscosity is raised, was shown to be around c=0.4. We confirm this with a flow close to shear at $\beta = 0.45$, but for a straining flow we observe the crossover at a much higher concentration $c = 0.6$. We hypothesise that this is due to the near-parallel flows close to shear (for which crystallisation occurs earlier even for smooth spheres) causing areas where the local concentration is much higher than the global concentration. Thus, if a global concentration of $c = 0.6$ (say) is the true crossover into the concentrated regime, there may well be regions in our shear flow in which the local concentration does exceed $c = 0.6$. Further investigation with a tighter parameter space around the $c = 0.3 \ldots 0.5$ and $\beta = 0.45 \ldots 0.55$ may be able to give more accurate results along with some sort of measure on local clustering.

Surprising results were the lack of effect of force factor factor compared to roughness height, although once the compressible asperities force function is plotted the effect is clear.

The compressible asperities produces good results consistent with other even though the curve fitting method for Galvin [29] figure 10 and 11 resulted in different values for roughness height.

Chapter 5

Conclusions and Future Work

5.1 Summary of the Thesis

Throughout this thesis we have investigated the flow of suspensions of solid spheres in a viscous fluid. We considered a monolayer of particles in an unbounded fluid, and carried out numerical simulations of its behaviour under a variety of linear flows. We used the numerical technique of Stokesian Dynamics, and considered cases of smooth and rough spheres.

The first research task was to implement a self-replicating lattice basis for general two-dimensional flows. Self-replicating bases already existed for shear and plain strain; we introduced first a basis for mixed shear and strain flow, and then a more general basis for any linear two dimensional flow. To achieve this, we defined a generic flow form that covers all linear two-dimensional flows: that is, any flow on the spectrum from pure rotation to plane strain, including shear flow as the midpoint of that spectrum. Later in the chapter, we proved that this generic flow covers all linear two-dimensional incompressible flows, by considering various rotations of the underlying axes to convert any given flow into the generic flow form.

The derivation of a self-replicating basis under this flow was then split into two parts: flows having more rotation than strain, and those having less rotation

than strain. (If the strain and rotation parts are equally strong we have a shear flow, which fits into neither formalism and has been extensively studied in the literature, so we did not study the shear case.) The split is needed because the former flow has complex eigenvalues and eigenvectors for one of the key matrices. The bases for both classes of flows were derived and linked. At this stage we also had to make a choice of convention for the definition of first normal stress difference under flows other than shear. Previous literature studies had only considered shear and strain flow: the first normal stress difference N_1 is well known under shear and must (for symmetry reasons) be zero under pure strain. We made the simplest choice which was consistent with these two fixed points, defining a normal stress based on the off-diagonal terms of the stress tensor under our flow form.

As a test of the correct implementation of different aspect ratios and rotations of lattice basis, we carried out static simulations of these flows for various concentration suspensions of smooth spheres. These static simulations are essentially the first timestep of a dynamic simulation: the spheres are placed at random in their periodically replicating box, the flow is imposed, and the resultant stresses calculated, but the particles never move from their initial positions so the system does not build up any flow-induced microstructure. The resultant stresses are called the short-time rheology of the system.

We found, as expected, that the short-time stresses were isotropic (i.e. Newtonian: the stress tensor, on average, was a scalar multiple of the rate-of-strain tensor). This is a direct result of the random placement of the particles. We also found that the viscosity – the scalar multiple relating stress to rate of strain – was independent of which flow and which lattice basis we were using, as expected. Finally (also as expected), the viscosity increases with increasing concentration. This numerical study was more of a sanity check than a serious piece of research; however, while short-time viscosities have been published before for 3D systems (from both numerical and experimental studies) our graph is the first such calculation for 2D systems.

We then moved onto the more interesting problem of dynamical simulations: simulations in which we moved beyond the initial timestep and evolve the positions of the particles according to the flow and the hydrodynamic stresses it causes. At this point, because the simulations became much more time-consuming, we had to make a reduction in the number of particles in each replicating lattice box, down to 30 particles per box. This reduction increased the statistical noise on the data, but when we later compared our viscosity results with a few choice runs with many more particles, we found that the average stresses were largely unaffected by the system size as long as the systems were at least as large as those we chose: 30 particles is enough for a good measure of viscosity.

As expected, the initial stresses recorded in the dynamic simulations match those from our earlier static calculations (subject to the higher values of noise commented on above). As the flow continues, a microstructure forms which results (at least at low to moderate concentrations) in the viscosities initially rising and then plateauing once the microstructure has formed.

As the concentration was increased we saw characteristic "spikes" in the plots of viscosity against time – events which were short in duration, during which the viscosity could increase by many orders of magnitude, and which therefore had a measurable effect on the time-averaged viscosity measure. These spikes were taken to be indicative of crystallisation or jamming: moments when a cluster of closely-spaced particles spanned the periodic box.

As expected, these crystal regions formed more strongly as the area concentration was increased; but we also presented results on the effect of the flow type parameter (which ranges from 0 for strain flow, through 1/2 for shear flow, to 1 for pure rotation) on the onset of crystallisation. This effect is quite marked, with flows that are close to shear flow (close to 1/2) showing the onset of crystallisation at much lower concentrations than other flow types. We hypothesised that this may be because of the unidirectional nature of shear flow: because flows close to shear flow are almost unidirectional, any crys-

talline regions which build up along the principal flow direction are likely to remain as there is little flow out of that line to break them up. Flows with a larger strain or rotation component are more multi-directional, and so although small crystals can form, they are then more likely to be broken up by the flow.

Of course, once a microstructure is allowed to form under the action of flow, the macroscopic fluid is no longer isotropic, and so the rheological response to flow does not have to be purely Newtonian. This means that, in addition to the viscosity as discussed above, we were able to investigate the first normal stress difference generated by the flow. Since at low concentrations the viscosity is finite but the normal stress zero, these data show a much lower magnitude relative to the noise in the signal. We found that the noise – which is part of the physical response of the system to flow – was correlated between the viscosity and normal stress signals: when the viscosity showed a spike, there would be a large (positive or negative) deviation in the normal stress signal, although not at the same order of magnitude as in the viscosity. There was no clear trend on the normal stress results (even the sign of the long-term averaged first normal stress difference is unclear) except that the noise, and the average magnitude of the normal stress signal, is larger at higher concentrations.

The final investigation of chapter 3 was a study of the rate at which the microstructure was formed by the flow. This was accessed through a curve-fitting program which assumed an exponential rate of build-up of microstructure with rate constant α, starting from the short-time value of the static simulations and ending with the long-time average rheology. Because of the low signal-to-noise ratio in the first normal stress data, these results were not suitable for the curve fitting; but since the same microstructure causes changes in both the viscosity and normal stress (as evidenced by the coincident spikes), it is reasonable to take these rate values from the viscosity time series alone. We found (unsurprisingly) that the microstructure forms more quickly at higher concentrations; there is little dependence on flow type.

As a final illustration of our results on smooth spheres, we showed some indicative snapshots of the particle positions during flows where some crystallisation had occurred. Some regions of regular particle arrangement, consistent with crystallisation, could be seen, and we proposed these crystallisation clusters as the mechanism of the spikes in the viscosity profile and the large short-lived deviations in the normal stress created by the flow.

In chapter 4 we considered the effects of surface roughness on a suspension of spheres. Guided by existing results in the literature (almost all of which were either for shear flow or for just two interacting particles), we used two different models for the inter-particle interaction caused by roughness. Both models treat the roughness as being able to cause some form of contact between two spheres when their nominal surfaces are still separated: in the "hard contact" model, the contact acts (via a purely repulsive force) to keep the spheres at a certain minimum separation, whereas in the "compressible asperities" model, the contact force is again purely repulsive but depends on the separation between the spheres. We chose to neglect tangential forces even though they are known to be necessary to accurately reproduce two-sphere experiments, as studies in shear flow have shown that the tangential part of the contact force is much less important to the rheology than the repulsive normal force.

The hard contact model we used is fairly widely used (though with variations in the detail of implementation in the literature) because it is a limiting case of many different contact models. The compressible asperities model was new in this work, so we began by deriving the form of the force law to reproduce some key experimental observations [29]. We fitted the experimental data (two distinct sets) with a non-linear spring law with four free parameters, and left ourselves with a single dimensionless parameter, which we called the force factor ff, a measure of the strength of the spring force relative to the hydrodynamic forces generated by the flow. We used three different values of ff (along with our two spring laws) to assess the effects of the soft-contact model; for hard contact, in which the only physical parameter is the roughness

height, we used two different heights.

In all the runs we carried out for rough spheres (using either model), the normal stress signal was extremely noisy: indeed, in every case the computed long-term average normal stress was within 1.96 standard deviations of zero, which means that we cannot detect an average normal stress different from zero at the 95% confidence level. Indeed, there is no consistent trend in our long-term average results for the sign of N_1: so we can only conclude that normal stresses are highly variable in these systems, and draw the rest of our conclusions from consideration of the viscosity alone.

We now move on to considering the two roughness models separately. When we implemented the hard contact model, we attempted to calculate the correct contact force for each pair of particles, such that their approach velocity was reduced to zero by the contact. This is in contrast to some of the literature work, in which a simple (large) Heaviside function was used for the force potential (in the presence of Brownian motion); this formalism does not reduce to the correct contact force in the limit of no Brownian motion. Instead, we calculated the contact force based on the relative approach velocity of the two spheres in the absence of any contact forces. Because of the approximations inherent in this pair-based approach (and because of numerical noise) we then needed to correct the positions of some particles to keep their separation close to the contact separation. Unfortunately, the result of this was a simulation that was very sensitive to timestep, requiring an unfeasibly small timestep to avoid an infinite loop in the position correction routine. This looping behaviour was taken to be indicative of the physical system coming close to crystallisation or jamming, in which many pairs of particles are in contact and the correction algorithm becomes difficult to use. The runs which had greatest success were those closer to pure strain or rotational flow; problems occurred more with flows closer to shear. This agrees with our results for smooth spheres, in which we concluded that unidirectional flows are more susceptible to crystallisation and jamming than other flows. At lower con-

centrations, where jamming is unlikely, our runs did complete, and we found some interesting results.

For flows close to shear flow, our results agreed with the conclusions of Wilson and Davis [63]: the addition of roughness to the particles lowers viscosities at low to moderate concentrations. However, for some flows close to strain flow in particular, we found that the viscosity climbed slowly over time, with no apparent stabilisation to a long-term value. However, after only 30 box repetitions we cannot hypothesis about the true long-term viscosity; we can, however, predict that if the viscosity does plateau (as we would expect, as a stable microstructure eventually builds up) its value for these parameters would be higher than for the equivalent smooth-sphere system. Flow type has an important effect on viscosity, even for low concentrations: in flows close to strain, the viscosity is raised by inter-particle roughness; close to shear flow, it is lowered.

The mechanism for the lowering of viscosity is well understood. This is because the repulsive forces cause the particles to spend less time in very close configurations than they would in the absence of roughness. Configurations where two sphere surfaces are very close together cause much of the dissipation (and hence viscosity) in the system, because these close zones produce large lubrication stresses: so reducing the time the particles spend close together is a mechanism to reduce the overall viscosity.

In flows close to strain, our results are surprising: a calculation in plane strain flow by Wilson [62] showed that, in an asymptotically dilute system, viscosity is reduced by exactly the hard contact model we have implemented here. The concentrations at which we see the rise in viscosity are as low as $c = 0.1$, which should fall within the asymptotically dilute regime. As yet we have found no explanation for these counter-intuitive results.

The argument explaining the expected lowering of viscosity by roughness is only valid for relatively dilute systems: systems, roughly, where (on average) the act of the contact force pushing two close particles apart does not result

in either of them coming into close contact with a third particle. At higher concentrations, only numerical investigation can provide information on the effects of roughness.

The final piece of research in this thesis was the investigation into roughness modelled with compressible asperities. In this case, independent of flow type (and according to expectation), at low concentrations we found a slightly lower viscosity due to the contact forces between the particles. At higher concentrations, we found that once crystallisation starts to occur its onset is more rapid than for smooth spheres, resulting in a higher viscosity at high concentrations. There was little difference between the results for our two different spring laws, which is not very surprising: although they were fit to different experimental data sets, the two spring laws have similar asymptotes for very close particles, and similar values of the cut off separation beyond which no contact force applies. Perhaps more surprisingly, the force factor ff had little effect on the viscosity results other than causing a small increase in viscosity at high concentrations. However, this was perhaps because we were limited to rather small values of ff by numerical difficulties. Similar to the hard-contact model, we found a high sensitivity to timestep, particularly if ff was not very small, and some runs could not be completed.

The effect of the flow type was similar to the smooth sphere case, with flows nearer shear showing a higher viscosity and more crystallization occurring. Despite the slightly lower viscosities at low concentrations with rough spheres compared to smooth spheres, the onset of crystallisation was unaffected by roughness in terms of both flow type and concentration. This suggests that the details of the roughness model used, and indeed of any inter-particle forces, may be unimportant for determining the onset of crystallisation: the two basic parameters of area concentration and the unidirectional nature of the flow are the most critical.

5.1.1 Ewald summation

In Appendix A we looked again at the problem of simulating systems in an infinite domain, and investigated the potential solution of the Ewald summation method. This method is now fairly standard in three-dimensional simulations, but has never been implemented for a purely two-dimensional system. The reason to use it is the problems of convergence in accounting for long-ranging mobility interactions over very large domains; Ewald summation deals with this problem by considering a Fourier transform of part of the function to be summed and carrying out the summation of that contribution in the resulting reciprocal space.

In order to use a purely two-dimensional periodic lattice, the formulae governing Ewald summation in Stokesian Dynamics need to be re-derived. We began by stating the mobility relations for both inter-particle interactions and self interactions in terms of derivatives of the Oseen tensor J_{ij}. We then presented the derivation of the standard three-dimensional Ewald summation, explaining the use of the Poisson summation formula. We were then able to present the required modifications to the derivation to take it from three dimensions to two dimensions.

In order to use Ewald summation in two dimensions, several specific mobility relations need to be derived. One ingredient of this calculation is the Fourier transform of the Oseen tensor $\mathbf{J}$. We derived this Fourier transform in some detail, using the conversion of the two-dimensional Fourier transform of an axisymmetric function into a Hankel transform. The derivation of the Hankel transform of the function $r\,\mathrm{erf}\,(\lambda r)$ was the most difficult task in the appendix. To carry it out, we used the theory of generalised functions [44] to justify the methods we used; derived a rule for calculating the Hankel transform of $r^2 f(r)$ when we know the transform of $f(r)$, and then worked up from the Hankel transform of r^1 to the required transform of $r\,\mathrm{erf}\,(\lambda r)$. Along with the relationship of the Fourier transform of a derivative of a function to the

Hankel transform of the same function, this allowed us to calculate all the reciprocal-space mobility relations.

Unfortunately at this stage we encountered a problem with the form of the Hankel transform in terms of how it decays in reciprocal space: i.e. only algebraically. This left us with the difficult problem of finding another sigmoidal curve to try and transform to obtain the required convergent reciprocal space summation.

Despite this setback, we presented a full list of all the real space mobility relations as these are still valid in three dimensions and provide minor corrections to those available in the literature.

5.2 Outlook

The work we have presented in this thesis opens up many possibilities for further study. There are several immediate questions raised from the thesis. In chapter 3 (using smooth spheres) we saw that a more unidirectional flow causes crystallisation to occur at a lower concentration than for multi-directional flows like strain and near-rotation flows. However, we are using a box containing only 30 particles. At the moment, when a moderate-sized crystal forms the clustering described in section 3.5.5 it can span our periodic box and cause a very large viscosity spike. It is quite likely that true crystallisation – in which a macroscopic system would jam – occurs at a higher concentration than the one we predict. A series of runs around the onset of crystallisation would help to ascertain more accurately at which β value flow, and at which area concentration, crystallisation begins to form. Additionally, a selection of runs with a larger number of particles per box might allow us to see a situation where there are clusters of crystallisation and areas of free flowing particles coexisting. This would allow us to more quantitatively predict real suspension viscosities. Studying the formation of these clusters would also help with determining the approximate number of particles needed per box to generate

reliable simulations for a given concentration. This could be studied for both smooth and rough spheres. It might be interesting to develop some kind of measure of local vs global concentration, to give insight into the development of the clusters; this value could then be tracked near the point of crystallisation. A complete formulation for Ewald summation in two dimensions would be an ideal area for further study and was one original aim of this thesis. The nature of the issues we had, make it clear that any sigmoidal curve will not do for the decaying function in real space. The problem is to find a function which decays appropriately (exponentially or better) in real space, and whose Hankel transform decays exponentially in reciprocal space. This is a case where the three dimensional case seems to work more straightforwardly than the two dimensional case.

Another major undertaking would be to implement a form of Brownian motion. This has been done elsewhere in the literature, but always in a shear flow. It would be a improvement in realism and as mentioned in section 1.3.12, Dratler [20] talks of the problem of overlapping particles in Stokesian Dynamics and how Brownian motion can solve this problem. Because of the extra motion in the system, an expected result of this would be to slightly delay the onset of crystallisation, although numerical experiments are clearly necessary to see whether this would be universal or whether the flow type has a critical effect.

Finally, another area of interest is the counter-intuitive results we saw at low concentrations in straining flow with rough spheres (e.g. figure 4.10), in which the viscosity grows, apparently indefinitely, with time, well beyond the equivalent smooth sphere viscosity, although theory predicts the long-term average viscosity to be lower than that for smooth spheres. Some longer runs for these situations would be of interest, to see whether the viscosity does plateau in the long term, and at what value. Equally, it would be nice to carry out a detailed comparison with a system of smooth spheres starting from the same initial conditions, to see where the two systems deviate from

one another and where the extra stresses originate.

Appendix A

Ewald Summation

A.1 Introduction

So far in this thesis we have used an imperfect extension of Stokesian Dynamics to suspensions which are infinite in extent in two spatial dimensions. As is usual in simulating large systems, we have taken a moderate number of particles in a tessellating box, and replicated that box throughout space.

In the resultant system, there is an infinite family of copies of each of our numbered particles. When calculating particle-pair interactions, we have simply used the closest copy of the particle in question – always taken from within the tessellating box or one of the eight lattice boxes surrounding it. We never consider the interaction of a particle with a more distant copy, nor with any of its own copies.

This means of course that we are neglecting the effects on the flow of all far field particles. This has no great implications for the two-body resistance forms, which decay quickly in space; but the mobility expressions decay rather slowly in space and so our approximation is rather poor. To rectify this we need to recalculate the far-field mobility matrix, taking account of particle images in many different replicating periodic boxes. The far-field mobility matrix describes the relationship between the forces, torques and stresslets,

and the velocities, rotations and background flow. A full description of the mobility matrix can be found in section 1.3.9. The problem with increasing the distances over which we sum our known two body far-field interactions is the poor convergence for large r, the distance between particle centres.

To overcome this problem we shall use Ewald summation [24] that is also used in electrostatics and can be used on many periodic systems. Ewald summation overcomes the problem by splitting it into two, transforming one sum into Fourier space performing the long range summation in Fourier space where there is good convergence and then transforming back into regular space and adding the result on to the other, real space summation.

Ewald summation is now a standard technique of Stokesian Dynamics (and indeed electromagnetism) for accelerating the calculation of pairwise relations across many particles in periodic boxes. However, for obvious physical reasons, the technique has been thoroughly developed in three dimensions.

Ewald summation was first applied to hydrodynamic problems by Beenakker [7]. Its essence lies in separating the function to be calculated into two parts, one of which may be summed quickly in real space and the other converging quickly when summed in reciprocal space. This theory is explained in more detail in section A.1.2.

Brady et al. in [13] extended Stokesian Dynamics to infinite suspensions. This itself was an extension of O'Brien's work [47] using a periodic lattice and Ewald sums to extend Stokesian Dynamics to an infinite three dimensional domain. In this chapter, we shall present the derivation of the necessary components to implement two dimensional Ewald summation on Stokesian Dynamics.

Unfortunately, after much work we discovered that one of our calculated functions did not converge rapidly as required (or indeed at all), as explained in section A.4.6 Nonetheless, we present the calculations of the mobility forms here for completeness

A.1.1 Mobility matrix entries in terms of J

In this section we give for reference the explicit forms of the individual mobility tensors used in $\mathcal{M}^\infty$ in terms of the Stokes–Oseen tensor $\mathbf{J}$. We are using here the notational convention of Kim & Karrila [37]:

$$\begin{pmatrix} \mathbf{U}^\infty - \mathbf{U} \\ \mathbf{\Omega}^\infty - \mathbf{\Omega} \\ \mathbf{E}^\infty \end{pmatrix} = \begin{pmatrix} \mathbf{a} & \tilde{\mathbf{b}} & \tilde{\mathbf{g}} \\ \mathbf{b} & \mathbf{c} & \tilde{\mathbf{h}} \\ \mathbf{g} & \mathbf{h} & \mathbf{m} \end{pmatrix} \begin{pmatrix} \mathbf{F} \\ \mathbf{T} \\ \mathbf{S} \end{pmatrix}, \tag{A.1}$$

to label the sub-matrices of the mobility matrix $\mathcal{M}^\infty$.

The elements of of the mobility matrix satisfy symmetry relations:

$$\begin{array}{lll} a_{ij} = a_{ji} & c_{ij} = c_{ji} & m_{ijkl} = m_{klij} \\ b_{ij} = \tilde{b}_{ji} & g_{ijk} = -\tilde{g}_{kij} & h_{ijk} = -\tilde{h}_{kij}, \end{array} \tag{A.2}$$

and the two tensors $\mathbf{b}$ and $\mathbf{h}$ are in fact pseudo-tensors. Because of the symmetry, we will not explicitly write out the tilde forms $\tilde{\mathbf{b}}$, $\tilde{\mathbf{g}}$ and $\tilde{\mathbf{h}}$. Throughout this section we use r_i to represent the vector joining sphere center α to sphere center β, r its length and $e_i = r_i/r$ the unit vector in the same direction. All lengths are made dimensionless using the particle radius a, and all mobility

tensors with $6\pi\mu a^n$ for whichever value of n is appropriate.

$$
\begin{aligned}
a_{ij}^{\alpha\beta} &= \frac{3}{4}J_{ij} + \frac{1}{4}\nabla^2 J_{ij} && \text{(A.3)}\\
&= \left[\frac{3}{4} + \frac{1}{4}\nabla^2\right] J_{ij} && \text{(A.4)}\\
b_{ij}^{\alpha\beta} &= -\frac{3}{16}\epsilon_{lkj}[\nabla_k J_{il} - \nabla_l J_{ik}] && \text{(A.5)}\\
&= -\frac{3}{16}\epsilon_{lkj}\left[\delta_{lp}\nabla_k - \delta_{kp}\nabla_l\right] J_{ip} && \text{(A.6)}\\
c_{ij}^{\alpha\beta} &= -\frac{3}{16}\nabla^2 J_{ij} && \text{(A.7)}\\
g_{ijk}^{\alpha\beta} &= -\frac{3}{8}\left[\nabla_i J_{jk} + \nabla_j J_{ik}\right] - \frac{1}{10}\nabla^2\left[\nabla_i J_{jk} + \nabla_j J_{ik}\right] && \text{(A.8)}\\
&= -\left[\frac{3}{8} + \frac{1}{10}\nabla^2\right]\left[\delta_{jl}\nabla_i + \delta_{il}\nabla_j\right] J_{lk} && \text{(A.9)}\\
h_{ijk}^{\alpha\beta} &= \frac{3}{16}\nabla^2[\epsilon_{jkl}J_{il} + \epsilon_{ikl}J_{jl}] && \text{(A.10)}\\
&= \frac{3}{16}\nabla^2[\delta_{il}\epsilon_{jkm} + \delta_{jl}\epsilon_{ikm}]J_{lm} && \text{(A.11)}\\
m_{ijkl}^{\alpha\beta} &= -\frac{3}{16}[\nabla_j\nabla_l J_{ik} + \nabla_j\nabla_k J_{il} + \nabla_i\nabla_l J_{jk} + \nabla_i\nabla_k J_{jl}]\\
&\quad - \frac{3}{80}\nabla^2[\nabla_j\nabla_l J_{ik} + \nabla_j\nabla_k J_{il} + \nabla_i\nabla_l J_{jk} + \nabla_i\nabla_k J_{jl}]. && \text{(A.12)}\\
&= -\left[\frac{3}{16} + \frac{3}{80}\nabla^2\right][\delta_{ip}\delta_{kq}\nabla_j\nabla_l\\
&\quad + \delta_{ip}\delta_{lq}\nabla_j\nabla_k + \delta_{jp}\delta_{kq}\nabla_i\nabla_l + \delta_{jp}\delta_{lq}\nabla_i\nabla_k]J_{pq}. && \text{(A.13)}
\end{aligned}
$$

We can use these forms to define a linear differential operator $\mathcal{L}^w$ for each mobility tensor $\mathbf{w}$, such that

$$\mathbf{w} = \mathcal{L}^w\mathbf{J} \qquad w_{ij(kl)} = \mathcal{L}^w_{ij(kl)pq}J_{pq} : \tag{A.14}$$

$$\mathcal{L}^a_{ijpq} = \left[\frac{3}{4} + \frac{1}{4}\nabla^2\right]\delta_{ip}\delta_{jq} \tag{A.15}$$

$$\mathcal{L}^b_{ijpq} = -\frac{3}{16}\epsilon_{lkj}\left[\delta_{lq}\nabla_k - \delta_{kq}\nabla_l\right]\delta_{ip} \tag{A.16}$$

$$\mathcal{L}^c_{ijpq} = -\frac{3}{16}\nabla^2\delta_{ip}\delta_{jq} \tag{A.17}$$

$$\mathcal{L}^g_{ijkpq} = -\left[\frac{3}{8} + \frac{1}{10}\nabla^2\right]\left[\delta_{jp}\nabla_i + \delta_{ip}\nabla_j\right]\delta_{kq} \tag{A.18}$$

$$\mathcal{L}^h_{ijkpq} = \frac{3}{16}\nabla^2[\delta_{ip}\epsilon_{jkq} + \delta_{jp}\epsilon_{ikq}] \tag{A.19}$$

$$\begin{aligned}\mathcal{L}^m_{ijklpq} = &-\left[\frac{3}{16} + \frac{3}{80}\nabla^2\right][\delta_{ip}\delta_{kq}\nabla_j\nabla_l \\ &+ \delta_{ip}\delta_{lq}\nabla_j\nabla_k + \delta_{jp}\delta_{kq}\nabla_i\nabla_l + \delta_{jp}\delta_{lq}\nabla_i\nabla_k].\end{aligned} \tag{A.20}$$

We also have the Stokes Oseen tensor in terms of derivatives of r from equation (1.28) of section 1.3.4:

$$J_{ij} = \left(\delta_{ij}\nabla^2 - \nabla_i\nabla_j\right)r. \tag{A.21}$$

This in turn allows us to represent the mobility relations in terms of derivatives of r. We shall use this fact later.

We also need the self-interaction terms, which are only nonzero for the tensors **a**, **c** and **m**:

$$a^{\alpha\alpha}_{ij} = \delta_{ij} \tag{A.22}$$

$$c^{\alpha\alpha}_{ij} = \frac{3}{4}\delta_{ij} \tag{A.23}$$

$$m^{\alpha\alpha}_{ijkl} = \frac{3}{20}(3\delta_{ik}\delta_{jl} + 3\delta_{il}\delta_{jk} - 2\delta_{ij}\delta_{kl}). \tag{A.24}$$

A.1.2 Ewald Summation

The first thing we must do is define the lattice. The lattice is constructed with basis **B** consisting of our basis vectors $\mathbf{b}_1, \ldots, \mathbf{b}_n$, where n is the number of dimensions. We will present the working in two dimensions but we shall first show a summary of the standard method of Ewald summation in three dimensions.

Considering the three dimensional case, if we consider a point $\mathbf{x}$ in one of our boxes, as our lattice is periodic a particle placed at $\mathbf{x}$ has images of itself at

positions $\mathbf{x} + \mathbf{x}_{lmn}$ where

$$\mathbf{x}_{lmn} = l\mathbf{b}_1 + m\mathbf{b}_2 + n\mathbf{b}_3 \tag{A.25}$$

and $l, m, n \in \mathbb{Z}$. This image particle experiences the same flow conditions (except for a solid-body motion) as the particle at $\mathbf{x}$. The effect of that particle and all its images on the other particles within the central box is what is calculated by the Ewald summation. In section (1.1) we derived the Stokes Oseen tensor which defines the fluid velocity produced by a point force. This can rewritten using matrix notation:

$$\mathbf{J}(\mathbf{x}) = \left(\frac{\mathbf{I}}{r} + \frac{\mathbf{x} \cdot \mathbf{x}}{r^3}\right). \tag{A.26}$$

The velocity relationship is

$$\mathbf{u} = \frac{1}{8\pi\mu}\mathbf{J}(\mathbf{x}) \cdot \mathbf{F}. \tag{A.27}$$

The tensor $\mathbf{J}$ is used in the derivation of all the key formulae of Stokesian Dynamics, as we calculate the flow resulting from a distribution of forces on the surface of each particle.

Now suppose each particle and all the forces on its surface is replicated periodically in space using our lattice. Clearly we must take these multiple copies into account. We can define our new relationship as

$$\begin{aligned} \mathbf{J}^{rep}(\mathbf{x}) &= \mathbf{J}(\mathbf{x}) + \mathbf{J}^{extra}(\mathbf{x}) \\ &= \mathbf{J}(\mathbf{x}) + \Sigma'_{l,m,n}\mathbf{J}(\mathbf{x} + \mathbf{x}_{lmn}) - L^{-3}\int \mathbf{J}(\mathbf{x} + \mathbf{x}')\mathrm{d}\mathbf{V}' \end{aligned} \tag{A.28}$$

where Σ' refers to the sum over all l, m, n except $l = m = n = 0$ and the integral is taken over all space. The first term is the contribution of the particle within the first lattice box that we are considering. The second term is the contribution from the particle images in the other lattice boxes. The third term represents a balancing of the forces applied to a particle in the fluid to stop the system having unbounded acceleration. If we simply apply a force to particle α in each box, the whole system will accelerate: instead, we must also

apply an equal and opposite force to each periodic box, distributed through the space in the box. This is equivalent to the background flow $\mathbf{u}_\infty$ in equation (1.29) in section 1.3.5, the difference is in section 1.3.5 we are considering an infinite unbounded domain were as here the domain has a bound in a sense of a very distant bounding surface. In this case equation (1.29) is written as

$$\begin{aligned} u_i(\mathbf{x}) = &- \frac{1}{8\pi\mu} \sum_{\alpha=1}^{N} \int_{S_\alpha} J_{ij}(\mathbf{x}-\mathbf{y}) f_j(\mathbf{y}) \mathrm{d}S_y \\ &. - \frac{1}{8\pi\mu} \sum_{\alpha=1}^{N} \int_{S_\Gamma} J_{ij}(\mathbf{x}-\mathbf{y}) f_j(\mathbf{y}) \mathrm{d}S_y \end{aligned} \tag{A.29}$$

where Γ is the outward bounding surface, more in Brady 1988 [13] and Ladyzhenskaya 1963 [43]. Finally $L^3 = |(\mathbf{b}_1 \wedge \mathbf{b}_2) \cdot \mathbf{b}_3|$ is the volume of the cell.

The theory and method used for the two dimensional case is of course similar but with only two basis vectors; we will see the full two dimensional calculation in section A.3. The main differences will be the conversion of the Fourier transform to two dimensions (which involves the Hankel transform) and the resulting different mobility formulas.

Equivalent forms to the equation (A.28) can be written for each of the mobility tensors given in section A.1.1. We replace the mobility tensors $\mathbf{w}^{\alpha\alpha}$ and $\mathbf{w}^{\alpha\beta}$ with their versions appropriate for a repeating cell of particles, $\mathbf{w}^{\alpha\alpha;rep}$ and $\mathbf{w}^{\alpha\beta;rep}$. This is essentially accomplished by replacing the Stokes–Oseen tensor $\mathbf{J}$ in each mobility tensor $\mathbf{w}$ by $\mathbf{J}^{rep}$.

For a particle's self-interactions, we must also include its interactions with other images of it: so a similar modification is made, by adding a contribution given by the form $\mathbf{w}^{\alpha\beta}$ and the modified Stokes Oseen tensor $\mathbf{J}^{extra}(\mathbf{0})$ to the original mobility tensor $\mathbf{w}^{\alpha\alpha}$.

Clearly, the difficult task here is the computation of $\mathbf{J}^{extra}(\mathbf{x})$ and the mobility matrices derived from it. Both the sum and the integral in equation (A.28) converge very slowly as the outer boundary is taken to infinity. It is this computation that is made possible by the method of Ewald summation.

A.2 Ewald summation and Poisson summation

To tackle the poorly-converging sum in equation (A.28), we use the Poisson summation formula:

$$\Sigma_{l,m,n} g(\mathbf{x}_{lmn}) = L^{-3} \Sigma_{l,m,n} \tilde{g}(\mathbf{k}_{lmn}), \tag{A.30}$$

with

$$\mathbf{k}_{lmn} = 2\pi(l\mathbf{b}_1 \wedge \mathbf{b}_3 + m\mathbf{b}_3 \wedge \mathbf{b}_2 + n\mathbf{b}_1 \wedge \mathbf{b}_2)/L^3, \tag{A.31}$$

We arbiterally choose this form for $\mathbf{k}$. We have defined the Fourier transform as

$$\tilde{g}(\mathbf{k}) = \int \exp(-i\mathbf{k}.\mathbf{x}) g(\mathbf{x}) \mathrm{d}\mathbf{V} \tag{A.32}$$

and inverse

$$g(\mathbf{x}) = \frac{1}{(2\pi)^3} \int \exp(i\mathbf{k}.\mathbf{x}) \tilde{g}(\mathbf{k}) \mathrm{d}\mathbf{V}_k \tag{A.33}$$

By applying this to $\mathbf{J}^{rep}$ and then inverting back to real space we obtain

$$\mathbf{J}^{rep}(\mathbf{x}) = L^{-3} \Sigma'_{l,m,n} e^{-i\mathbf{k}_{lmn}.\mathbf{x}} \tilde{\mathbf{J}}(\mathbf{k}_{lmn}), \tag{A.34}$$

for $\mathbf{x} \neq \mathbf{0}$. Upon analysing this, it is clear that this sum does not converge very well for large k, which corresponds to small r; but the problem for the original summation was the convergence for large r. This leads to the approach of splitting the summation into near and far field parts, nearfield to be summed in real space $\mathbf{r}$, and farfield to be summed in reciprocal space, $\mathbf{k}$. To do this we shall rewrite $\mathbf{J}$ in an alternative form for convenience,

$$\mathbf{J}(\mathbf{x}) = (\mathbf{I}\nabla^2 - \nabla\nabla) r. \tag{A.35}$$

This is equivalent to our form of the Stokes Oseen tensor. Consider

$$\frac{\partial^2}{\partial x_i \partial x_j} r = \frac{\delta_{ij}}{r} - \frac{x_i x_j}{r^3},$$

if we let $i = j$ we get

$$\frac{\partial^2}{\partial x_i \partial x_i} r = \frac{2}{r},$$

adding gives us

$$\delta_{ij}\nabla^2 r - \frac{\partial^2}{\partial x_i \partial x_j} r = \frac{\delta_{ij}}{r} + \frac{x_i x_j}{r^3} = J_{ij}.$$

We define

$$\mathbf{J}^r = (\mathbf{I}\nabla^2 - \nabla\nabla)[r\,\mathrm{erfc}(\lambda r)], \tag{A.36}$$

$$\mathbf{J}^k = (\mathbf{I}\nabla^2 - \nabla\nabla)[r\,\mathrm{erf}(\lambda r)], \tag{A.37}$$

so that

$$\mathbf{J} = \mathbf{J}^r + \mathbf{J}^k. \tag{A.38}$$

Here erf and erfc are the error function and complementary error function, respectively:

$$\mathrm{erf}(y) = \frac{2}{\sqrt{\pi}} \int_0^y e^{-t^2}\,\mathrm{d}t \qquad \mathrm{erfc}(y) = 1 - \mathrm{erf}(y). \tag{A.39}$$

The parameter λ effectively determines the radius at which the major contribution switches from $\mathbf{J}^r$ to $\mathbf{J}^k$: if λ is very large $\mathbf{J} \approx \mathbf{J}^k$ for moderate r, whereas for very small λ, $\mathbf{J} \approx \mathbf{J}^r$ over most values of r. A suggested value by Beenakker [7] is $\lambda = \sqrt{\pi}/L$.

Now splitting $\mathbf{J}^{extra}$ in a similar way to $\mathbf{J}$, we find that for $\mathbf{J}^r$ both the sum and the integral converge quickly in the far-field because of the strong decay of the complementary error function $\mathrm{erfc}(\lambda r)$:

$$\mathbf{J}^{r;extra}(\mathbf{x}) = \Sigma'_{l,m,n}\mathbf{J}^r(\mathbf{x} + \mathbf{x}_{lmn}) - L^{-3}\int \mathbf{J}^r(\mathbf{x} + \mathbf{x}')\,\mathrm{d}^3\mathbf{x}'. \tag{A.40}$$

Indeed, the integral can easily be shown to be identically zero for $\lambda \neq 0$.

$$\begin{aligned}\int \mathbf{J}^r_{ij}(\mathbf{x} + \mathbf{x}')\,\mathrm{d}^3\mathbf{x}' &= \int \mathbf{J}^r_{ij}(\mathbf{x})\,\mathrm{d}^3\mathbf{x} \\ &= \int (\delta_{ij}\nabla^2 - \nabla_i\nabla_j)[r\,\mathrm{erfc}(\lambda r)]\,\mathrm{d}^3\mathbf{x} \\ &= (\delta_{ij}\delta_{pq} - \delta_{ip}\delta_{jq}) \int \nabla_p\nabla_q[r\,\mathrm{erfc}(\lambda r)]\,\mathrm{d}^3\mathbf{x},\end{aligned} \tag{A.41}$$

and an isotropy condition gives

$$\int \nabla_p \nabla_q [r \operatorname{erfc}(\lambda r)] \, \mathrm{d}^3\mathbf{x} = A\delta_{pq}. \tag{A.42}$$

Now putting $p = q$

$$\begin{aligned} 3A &= \int \nabla^2 [r \operatorname{erfc}(\lambda r)] \, \mathrm{d}^3\mathbf{x}, \\ &= \int_{\theta=0}^{\pi} \int_{\phi=0}^{2\pi} \int_{r=0}^{\infty} \frac{1}{r^2} \frac{\partial}{\partial r} \left(r^2 \frac{\partial}{\partial r} \left(r \operatorname{erfc}(\lambda r) \right) \right) r^2 \sin\theta \mathrm{d}r \mathrm{d}\phi \mathrm{d}\theta, \\ &= \int_{\theta=0}^{\pi} \int_{\phi=0}^{2\pi} \left[r^2 \frac{\partial}{\partial r} (r \operatorname{erfc}(\lambda r)) \right]_{r=0}^{\infty} \mathrm{d}\phi \, \mathrm{d}\theta = 0. \end{aligned} \tag{A.43}$$

The contributions of this part of $\mathbf{J}$ to the mobility tensors can be deduced:

$$\mathbf{w}^{r;extra}(\mathbf{x}) = \Sigma'_{l,m,n} \mathcal{L}^w \mathbf{J}^r(\mathbf{x} + \mathbf{x}_{lmn}) - L^{-3} \int \mathcal{L}^w \mathbf{J}^r(\mathbf{x} + \mathbf{x}') \, \mathrm{d}^3\mathbf{x}', \tag{A.44}$$

where $\mathcal{L}^w$ are the linear differential operators defined in section A.1.1 to express the mobility matrices in terms of $\mathbf{J}$.

There remains the k part of the Stokes–Oseen tensor, $\mathbf{J}^k$, the far field part of the summation done in reciprocal space. The sum and integral associated with this part suffer from the same convergence issues as the original tensor did; and this is where Fourier transforms and the Poisson summation formula come in.

A.2.1 Sums and the Fourier Transform

In this section we will show how the calculation of $\mathbf{J}^{k;extra}$ and its contributions to the mobility tensors can be made into a rapidly-converging sum using the Fourier transform. The key definitions are (for each mobility tensor $\mathbf{w}$):

$$\mathbf{J}^{k;extra}(\mathbf{x}) = \Sigma'_{l,m,n} \mathbf{J}^k(\mathbf{x} + \mathbf{x}_{lmn}) - L^{-3} \int \mathbf{J}^k(\mathbf{x} + \mathbf{x}') \, \mathrm{d}^3\mathbf{x}' \tag{A.45}$$

$$\mathbf{w}^{k;extra}(\mathbf{x}) = \Sigma'_{l,m,n} \mathcal{L}^w \mathbf{J}^k(\mathbf{x} + \mathbf{x}_{lmn}) \tag{A.46}$$

$$- L^{-3} \int \mathcal{L}^w \mathbf{J}^k(\mathbf{x} + \mathbf{x}') \, \mathrm{d}^3\mathbf{x}', \tag{A.47}$$

in which

$$\mathbf{J}^k(\mathbf{x}) = (\mathbf{I}\nabla^2 - \nabla\nabla)[r \operatorname{erf}(\lambda r)]. \tag{A.48}$$

The $\mathrm{erf}(\lambda r)$ and $\mathrm{erfc}(\lambda r)$ act as slow switches between the real and reciprocal space summation. The entire summation involved in $\mathbf{J}^{extra}$ could be done in either real or reciprocal space, however the two sums converge well at opposite ends of the summation. The real space part $\mathbf{J}^r$ converges well in real space, but the reciprocal space part $\mathbf{J}^k$ does not. The results we stated earlier about the Poisson summation can now be used on $\mathbf{J}^k$ to convert it to a reciprocal space sum which converges well in $\mathbf{k}$. It is in this way that we use the properties of each summation to our advantage. To see the details, we need to take Fourier transforms of the Stokes Oseen relationship and the mobility relationships. We defined the Fourier transform in equations (A.32) and (A.33). Substituting those definitions into the sum:

$$\begin{aligned}
&\sum_{l,m,n} g(\mathbf{x}_0 + l\mathbf{b}_1 + m\mathbf{b}_2 + n\mathbf{b}_3) \\
&\quad = (2\pi)^{-3} \int \sum_l \sum_m \sum_n e^{i\mathbf{k}\cdot(\mathbf{x}_0 + l\mathbf{b}_1 + m\mathbf{b}_2 + n\mathbf{b}_3)} \tilde{g}(\mathbf{k})\, \mathrm{d}^3\mathbf{k} \\
&\quad = (2\pi)^{-3} \int \sum_l \exp\left[il\mathbf{k}\cdot\mathbf{b}_1\right] \sum_m \exp\left[im\mathbf{k}\cdot\mathbf{b}_2\right] \\
&\qquad \times \sum_n \exp\left[in\mathbf{k}\cdot\mathbf{b}_3\right] \exp\left[i\mathbf{k}\cdot\mathbf{x}_0\right] \tilde{g}(\mathbf{k})\, \mathrm{d}^3\mathbf{k}.
\end{aligned} \tag{A.49}$$

Now if we write $\mathbf{k} = 2\pi(u\mathbf{b}_1 \wedge \mathbf{b}_3 + v\mathbf{b}_3 \wedge \mathbf{b}_2 + w\mathbf{b}_1 \wedge \mathbf{b}_2)/L^3$ we can change the integral to

$$\begin{aligned}
&\sum_{l,m,n} g(\mathbf{x}_0 + l\mathbf{b}_1 + m\mathbf{b}_2 + n\mathbf{b}_3) \\
&\quad = L^{-3} \int_w \int_v \int_u \sum_l \exp\left[2\pi ilv\right] \sum_m \exp\left[2\pi imu\right] \sum_n \exp\left[2\pi inw\right] \\
&\qquad \times \exp\left[2\pi i(u\mathbf{b}_1 \wedge \mathbf{b}_3 + v\mathbf{b}_3 \wedge \mathbf{b}_2 + w\mathbf{b}_1 \wedge \mathbf{b}_2)\cdot\mathbf{x}_0/L^3\right] \\
&\qquad \times \tilde{g}(2\pi(u\mathbf{b}_1 \wedge \mathbf{b}_3 + v\mathbf{b}_3 \wedge \mathbf{b}_2 + w\mathbf{b}_1 \wedge \mathbf{b}_2)/L^3)\, \mathrm{d}u\, \mathrm{d}v\, \mathrm{d}w.
\end{aligned} \tag{A.50}$$

Now we use the Fourier series

$$\sum_n \delta(v - n) = \sum_m \exp\left[2\pi imv\right], \tag{A.51}$$

to get

$$\begin{aligned}
&\sum_{l,m,n} g(\mathbf{x}_0 + l\mathbf{b}_1 + m\mathbf{b}_2 + n\mathbf{b}_3) \\
&\quad = L^{-3} \int_w \int_v \int_u \sum_l \delta(v-l) \sum_m \delta(u-m) \sum_n \delta(w-n) \\
&\qquad \times \exp\left[2\pi i(u\mathbf{b}_1 \wedge \mathbf{b}_3 + v\mathbf{b}_3 \wedge \mathbf{b}_2 + w\mathbf{b}_1 \wedge \mathbf{b}_2) \cdot \mathbf{x}_0/L^3\right] \\
&\qquad \times \tilde{g}(2\pi(u\mathbf{b}_1 \wedge \mathbf{b}_3 + v\mathbf{b}_3 \wedge \mathbf{b}_2 + w\mathbf{b}_1 \wedge \mathbf{b}_2)/L^3)\, \mathrm{d}u\, \mathrm{d}v\, \mathrm{d}w. \\
&\quad = L^{-3} \sum_{l,m,n} \exp\left[2\pi i(m\mathbf{b}_1 \wedge \mathbf{b}_3 + l\mathbf{b}_3 \wedge \mathbf{b}_2 + n\mathbf{b}_1 \wedge \mathbf{b}_2) \cdot \mathbf{x}_0/L^3\right] \\
&\qquad \times \tilde{g}(2\pi(m\mathbf{b}_1 \wedge \mathbf{b}_3 + l\mathbf{b}_3 \wedge \mathbf{b}_2 + n\mathbf{b}_1 \wedge \mathbf{b}_2)/L^3).
\end{aligned} \tag{A.52}$$

We have derived the Poisson summation formula:

$$\begin{aligned}
&\sum_{l,m,n} g(\mathbf{x}_0 + l\mathbf{b}_1 + m\mathbf{b}_2 + n\mathbf{b}_3) \\
&\quad = L^{-3} \sum_{l,m,n} \exp\left[2\pi i(m\mathbf{b}_1 \wedge \mathbf{b}_3 + l\mathbf{b}_3 \wedge \mathbf{b}_2 + n\mathbf{b}_1 \wedge \mathbf{b}_2) \cdot \mathbf{x}_0/L^3\right] \\
&\qquad \times \tilde{g}(2\pi(m\mathbf{b}_1 \wedge \mathbf{b}_3 + l\mathbf{b}_3 \wedge \mathbf{b}_2 + n\mathbf{b}_1 \wedge \mathbf{b}_2)/L^3)
\end{aligned} \tag{A.53}$$

(note that in this case the sums are over *all* values of l, m and n). If we define

$$\mathbf{k}_{lmn} = 2\pi[l\mathbf{b}_3 \wedge \mathbf{b}_2 + m\mathbf{b}_1 \wedge \mathbf{b}_3 + n\mathbf{b}_1 \wedge \mathbf{b}_2]/L^3, \tag{A.54}$$

we obtain

$$\sum_{l,m,n} g(\mathbf{x}_0 + \mathbf{x}_{lmn}) = L^{-3} \sum_{l,m,n} \exp\left[i\mathbf{k}_{lmn} \cdot \mathbf{x}_0\right] \tilde{g}(\mathbf{k}_{lmn}) \tag{A.55}$$

and hence

$$\Sigma'_{l,m,n} g(\mathbf{x}_0 + \mathbf{x}_{lmn}) = L^{-3} \sum_{l,m,n} \exp\left[i\mathbf{k}_{lmn} \cdot \mathbf{x}_0\right] \tilde{g}(\mathbf{k}_{lmn}) - g(\mathbf{x}_0). \tag{A.56}$$

The quantity we wanted to calculate from equation (A.47) was

$$\mathbf{w}^{k;extra}(\mathbf{x}) = \Sigma'_{l,m,n} \mathcal{L}^w \mathbf{J}^k(\mathbf{x} + \mathbf{x}_{lmn}) - L^{-3} \int \mathcal{L}^w \mathbf{J}^k(\mathbf{x} + \mathbf{x}')\, \mathrm{d}^3\mathbf{x}', \tag{A.57}$$

and we can now use equation (A.56) to rewrite this as

$$\begin{aligned}
\mathbf{w}^{k;extra}(\mathbf{x}) = L^{-3} \sum_{l,m,n} \exp\left[i\mathbf{k}_{lmn} \cdot \mathbf{x}\right] \widetilde{\mathcal{L}^w \mathbf{J}^k}(\mathbf{k}_{lmn}) \\
- \mathcal{L}^w \mathbf{J}^k(\mathbf{x}) - L^{-3} \int \mathcal{L}^w \mathbf{J}^k(\mathbf{x} + \mathbf{x}')\, \mathrm{d}^3\mathbf{x}'.
\end{aligned} \tag{A.58}$$

Since

$$\tilde{g}(\mathbf{0}) = \int g(\mathbf{x}')\,\mathrm{d}^3\mathbf{x}' = \int g(\mathbf{x}+\mathbf{x}')\,\mathrm{d}^3\mathbf{x}', \tag{A.59}$$

the integral contribution cancels with the summation term from $\mathbf{k} = \mathbf{0}$ (or $l = m = n = 0$) and we can deduce for each mobility function:

$$\mathbf{w}^{k;extra}(\mathbf{x}) = L^{-3}\Sigma'_{l,m,n}\exp\left[i\mathbf{k}_{lmn}\cdot\mathbf{x}\right]\widetilde{\mathcal{L}^w\mathbf{J}^k}(\mathbf{k}_{lmn}) - \mathcal{L}^w\mathbf{J}^k(\mathbf{x}). \tag{A.60}$$

Unlike the real-space summation of $\mathbf{J}^k$ which did not converge in the far field, the terms $\widetilde{\mathcal{L}^w\mathbf{J}^k}(\mathbf{k}_{lmn})$ decay rapidly as $|\mathbf{k}_{lmn}| \to \infty$, and this sum can be truncated without great loss of accuracy.

A.2.2 Constructing the mobility tensors for a periodic system

For a given tensor $\mathbf{w}$, we construct its periodic equivalent using contributions derived from $\mathbf{J}^r$ and $\mathbf{J}^k$. For the self-interaction, we must include the original self-interaction and the summed interactions of our particle with its images in other periodic boxes:

$$\begin{aligned}
\mathbf{w}^{\alpha\alpha;rep} &= \mathbf{w}^{\alpha\alpha} + \Sigma'_{l,m,n}\mathcal{L}^w\mathbf{J}(\mathbf{x}_{lmn}) - L^{-3}\int \mathcal{L}^w\mathbf{J}(\mathbf{x}')\,\mathrm{d}^3\mathbf{x}' && \text{(A.61)}\\
&= \mathbf{w}^{\alpha\alpha} + \mathbf{w}^{r;extra}(\mathbf{x}) + \mathbf{w}^{k;extra}(\mathbf{0}), && \text{(A.62)}
\end{aligned}$$

Using our derived result (A.60):

$$\begin{aligned}
\mathbf{w}^{\alpha\alpha;rep} =& \mathbf{w}^{\alpha\alpha} + \Sigma'_{l,m,n}\mathcal{L}^w\mathbf{J}^r(\mathbf{x}_{lmn}) - L^{-3}\int \mathcal{L}^w\mathbf{J}^r(\mathbf{x}')\,\mathrm{d}^3\mathbf{x}'\\
&+ L^{-3}\Sigma'_{l,m,n}\widetilde{\mathcal{L}^w\mathbf{J}^k}(\mathbf{k}_{lmn}) - \mathcal{L}^w\mathbf{J}^k(\mathbf{0}).
\end{aligned} \tag{A.63}$$

In a similar way,

$$\begin{aligned}
\mathbf{w}^{\alpha\beta;rep}(\mathbf{x}) &= \mathbf{w}^{\alpha\beta}(\mathbf{x}) + \Sigma'_{lmn}\mathcal{L}^w\mathbf{J}(\mathbf{x}+\mathbf{x}_{lmn})\\
&\qquad - L^{-3}\int \mathcal{L}^w\mathbf{J}(\mathbf{x}+\mathbf{x}')\,\mathrm{d}^3\mathbf{x}' && \text{(A.64)}\\
&= \mathbf{w}^{\alpha\beta}(\mathbf{x}) + \mathbf{w}^{r;extra}(\mathbf{x}) + \mathbf{w}^{k;extra}(\mathbf{x}) && \text{(A.65)}\\
&= \Sigma_{l,m,n}\mathcal{L}^w\mathbf{J}^r(\mathbf{x}+\mathbf{x}_{lmn}) - L^{-3}\int \mathcal{L}^w\mathbf{J}^r(\mathbf{x}+\mathbf{x}')\,\mathrm{d}^3\mathbf{x}'\\
&\quad + L^{-3}\Sigma'_{l,m,n}\exp\left[i\mathbf{k}_{lmn}\cdot\mathbf{x}\right]\widetilde{\mathcal{L}^w\mathbf{J}^k}(\mathbf{k}_{lmn}). && \text{(A.66)}
\end{aligned}$$

For the Stokes Oseen tensor alone, we note that

$$\mathbf{J}_{ij}^{k}(\mathbf{0}) \;=\; (\delta_{ij}\delta_{kl}-\delta_{ik}\delta_{jl})\left[\nabla_k\nabla_l[r\,\mathrm{erf}(\lambda r)]\right]_{\mathbf{r=0}}. \tag{A.67}$$

Letting

$$\begin{aligned}
A\delta_{kl} &= \left[\nabla_k\nabla_l[r\,\mathrm{erf}(\lambda r)]\right]_{\mathbf{r=0}} && \text{(A.68)}\\
3A &= \left[\nabla^2[r\,\mathrm{erf}(\lambda r)]\right]_{\mathbf{r=0}} && \text{(A.69)}\\
&= \left[\frac{1}{r}\frac{\mathrm{d}}{\mathrm{d}r}\left(r\frac{\mathrm{d}}{\mathrm{d}r}[r\,\mathrm{erf}(\lambda r)]\right)\right]_{\mathbf{r=0}} && \text{(A.70)}\\
&= \left[\frac{1}{r}\frac{\mathrm{d}}{\mathrm{d}r}\left(r\left[\mathrm{erf}(\lambda r)+r\frac{2\lambda}{\sqrt{\pi}}\exp\left[-(\lambda r)^2\right]\right]\right)\right]_{\mathbf{r=0}} && \text{(A.71)}\\
&= \left[\frac{1}{r}\frac{\mathrm{d}}{\mathrm{d}r}\left(r\,\mathrm{erf}(\lambda r)+r^2\frac{2\lambda}{\sqrt{\pi}}\exp\left[-(\lambda r)^2\right]\right)\right]_{\mathbf{r=0}} && \text{(A.72)}\\
&= \left[\frac{1}{r}\left(\mathrm{erf}(\lambda r)+(3-2\lambda^2r^2)\frac{2\lambda r}{\sqrt{\pi}}\exp\left[-(\lambda r)^2\right]\right)\right]_{\mathbf{r=0}} && \text{(A.73)}\\
&= \left[\frac{1}{r}\,\mathrm{erf}(\lambda r)+(3-2\lambda^2r^2)\frac{2\lambda}{\sqrt{\pi}}\exp\left[-(\lambda r)^2\right]\right]_{\mathbf{r=0}} && \text{(A.74)}\\
&= \left[\frac{1}{r}\frac{2}{\sqrt{\pi}}\int_0^{\lambda r}e^{-t^2}\,\mathrm{d}t+\frac{6\lambda}{\sqrt{\pi}}\right]_{\mathbf{r=0}} && \text{(A.75)}\\
&= \left[\frac{1}{r}\frac{2}{\sqrt{\pi}}\int_0^{\lambda r}(1-t^2+t^4/2-\cdots)\,\mathrm{d}t+\frac{6\lambda}{\sqrt{\pi}}\right]_{\mathbf{r=0}} && \text{(A.76)}\\
&= \left[\frac{1}{r}\frac{2}{\sqrt{\pi}}\left[t-\frac{t^3}{3}+\frac{t^5}{10}-\cdots\right]_0^{\lambda r}+\frac{6\lambda}{\sqrt{\pi}}\right]_{\mathbf{r=0}} && \text{(A.77)}\\
&= \left[\frac{1}{r}\frac{2}{\sqrt{\pi}}\left(\lambda r-\frac{\lambda^3r^3}{3}+\cdots\right)+\frac{6\lambda}{\sqrt{\pi}}\right]_{\mathbf{r=0}}=\frac{8\lambda}{\sqrt{\pi}}, && \text{(A.78)}
\end{aligned}$$

finally giving,

$$A \;=\; \frac{8\lambda}{3\sqrt{\pi}}, \tag{A.79}$$

which allows us to say

$$\begin{aligned}
\left[\nabla_k\nabla_l[r\,\mathrm{erf}(\lambda r)]\right]_{\mathbf{r=0}} &= \frac{8\lambda}{3\sqrt{\pi}}\delta_{kl} && \text{(A.80)}\\
\mathbf{J}_{ij}^{k}(\mathbf{0}) &= \frac{16\lambda}{3\sqrt{\pi}}\delta_{ij}, && \text{(A.81)}
\end{aligned}$$

hence

$$\mathbf{J}^{k}(\mathbf{0})=\frac{16\lambda}{3\sqrt{\pi}}\mathbf{I}. \tag{A.82}$$

A.3 Modified calculation for a two-dimensional lattice

We have reviewed the theory of Ewald summation in three dimensions. Now we present the modifications which must be made, in order to carry out the same summations for a system which replicates periodically in just two dimensions. Listing the changes which must be made in moving from three dimensions to two dimensions:

Fourier Transform definition

We define the two dimensional Fourier transform of any function $g(\mathbf{x})$ as

$$\tilde{g}(\mathbf{k}) = \int \exp\left[-i\mathbf{k}\cdot\mathbf{x}\right] g(\mathbf{x})\, \mathrm{d}^2\mathbf{x}, \tag{A.83}$$

with the integral taken over two-dimensional space. The inverse Fourier transform is then given by

$$g(\mathbf{x}) = (2\pi)^{-2} \int e^{i\mathbf{k}\cdot\mathbf{x}} \tilde{g}(\mathbf{k})\, \mathrm{d}^2\mathbf{k}. \tag{A.84}$$

Box volume

The volume of the box becomes an area

$$L^2 = |\mathbf{b}_1 \wedge \mathbf{b}_2| \tag{A.85}$$

Summations

Summations are only over m and n; not the triplet $\{l, m, n\}$. The lattice vector $\mathbf{x}_{lmn}$ becomes $\mathbf{x}_{mn}$:

$$\mathbf{x}_{mn} = m\mathbf{b}_1 + n\mathbf{b}_2. \tag{A.86}$$

Reciprocal space basis vectors

In three dimensions we were able to define

$$\mathbf{k}_{lmn} = 2\pi(l\mathbf{b}_1 \wedge \mathbf{b}_3 + m\mathbf{b}_3 \wedge \mathbf{b}_2 + n\mathbf{b}_1 \wedge \mathbf{b}_2)/L^3, \tag{A.87}$$

without defining any new vectors. In two dimensions we first define a unit vector out of the plane of our system, $\mathbf{e}_z = (\mathbf{b}_1 \wedge \mathbf{b}_2)/L^2$, and then use it to define the two dimensional reciprocal basis vectors:

$$\mathbf{k}_a = 2\pi \mathbf{e}_z \wedge \mathbf{b}_1 / L^2, \qquad \mathbf{k}_b = 2\pi \mathbf{b}_2 \wedge \mathbf{e}_z / L^2. \tag{A.88}$$

We can then define

$$\mathbf{k}_{mn} = m\mathbf{k}_a + n\mathbf{k}_b. \tag{A.89}$$

Dimensionality of space

All integration only occurs over two dimensions of space; and each instance of L^3 or $(2\pi)^3$ is replaced by L^2 or $(2\pi)^2$ respectively.

Taking all of these changes into account the important results are as follows. The Poisson summation formula becomes

$$\sum_{m,n} g(\mathbf{x}_0 + \mathbf{x}_{mn}) = L^{-2} \sum_{m,n} \exp\left[i\mathbf{k}_{mn} \cdot \mathbf{x}_0\right] \tilde{g}(\mathbf{k}_{mn}) \tag{A.90}$$

For each mobility function the extra contribution due to the summation in reciprocal space becomes

$$\mathbf{w}^{k;extra}(\mathbf{x}) = L^{-2} \sum_{m,n \neq 0} \exp\left[i\mathbf{k}_{mn} \cdot \mathbf{x}\right] \widetilde{\mathcal{L}^w \mathbf{J}^k}(\mathbf{k}_{mn}) - \mathcal{L}^w \mathbf{J}^k(\mathbf{x}). \tag{A.91}$$

The two key results of equations (A.63) and (A.66) become

$$\begin{aligned} \mathbf{w}^{\alpha\alpha;rep} =& \mathbf{w}^{\alpha\alpha} + \Sigma'_{m,n} \mathcal{L}^w \mathbf{J}^r(\mathbf{x}_{mn}) - L^{-2} \int \mathcal{L}^w \mathbf{J}^r(\mathbf{x}') \, \mathrm{d}^2\mathbf{x}' \\ &+ L^{-2} \Sigma'_{m,n} \widetilde{\mathcal{L}^w \mathbf{J}^k}(\mathbf{k}_{mn}) - \mathcal{L}^w \mathbf{J}^k(\mathbf{0}) \end{aligned} \tag{A.92}$$

and

$$\begin{aligned} \mathbf{w}^{\alpha\beta;rep}(\mathbf{x}) \quad = \quad & \Sigma_{m,n} \mathcal{L}^w \mathbf{J}^r(\mathbf{x} + \mathbf{x}_{mn}) - L^{-2} \int \mathcal{L}^w \mathbf{J}^r(\mathbf{x} + \mathbf{x}') \, \mathrm{d}^2\mathbf{x}' \\ & + L^{-2} \Sigma'_{m,n} \exp\left[i\mathbf{k}_{mn} \cdot \mathbf{x}\right] \widetilde{\mathcal{L}^w \mathbf{J}^k}(\mathbf{k}_{mn}). \end{aligned} \tag{A.93}$$

When calculating explicit formulae to be summed in the real and reciprocal space, we also need to calculate the new, two-dimensional Fourier transform of $r \operatorname{erf}(\lambda r)$ and its derivatives; these will be different from their three dimensional forms, as we will see in section A.4.

A.4 Fourier transform of $\mathbf{J}^k$.

The relationship between real and reciprocal space has been explained in A.2. The Fourier transforms of all our mobility relationships need to be calculated. This is done by first considering the Fourier transform of the far-field contribution to the Stokes Oseen tensor $\mathbf{J}$, and then calculating the transform of all the derivatives of $\mathbf{J}^k$. However, because we are now in two dimensions, our Fourier transform becomes a Hankel transform. Once we understand what a Hankel transform is we can start to calculate the Hankel transform of our relationships. The mobility relations in Stokesian Dynamics are expressed in terms of linear differential operators acting on the Stokes Oseen tensor, so to calculate the Hankel transforms of the mobility relations we will need the transforms of derivatives of $\mathbf{J}^k$.

To calculate the Hankel transforms $\mathbf{J}^k$ and the reciprocal space part of our mobility relations we will build up through six stages:

1. Hankel function definition;
2. The derivative rule;
3. Rule for multiplication by r^2;
4. Generalised functions;
5. Hankel transform of r^{-1};
6. Hankel transform of $r\,\mathrm{erf}(\lambda r)$.

A.4.1 Fourier transform to Hankel transform

The 2D Fourier transform of a function $f(\mathbf{x}) = f(x, y)$ was defined in equation (A.83) as

$$\begin{aligned} F(k_1, k_2) :=& \tilde{f}(\mathbf{k}) \\ &= \int \exp\left[-i\mathbf{k}\cdot\mathbf{x}\right] f(\mathbf{x})\,\mathrm{d}^2\mathbf{x}. \end{aligned} \tag{A.94}$$

If the function to be transformed is axisymmetric about the origin, i.e. $f(x,y) = g(r)$ with $r^2 = x^2 + y^2$, then the 2D Fourier transform of f becomes

$$F(k_1,k_2) = \int_{x=-\infty}^{\infty}\int_{y=-\infty}^{\infty} f(x,y)e^{-i(k_1x+k_2y)}\,dy\,dx \tag{A.95}$$

and if we denote $k^2 = k_1^2 + k_2^2$ then $F(k_1,k_2) = G(k)$ where

$$G(k) = \int_{r=0}^{\infty}\int_{\theta=0}^{2\pi} rg(r)e^{-ikr\cos\theta}\,d\theta\,dr = 2\pi\int_{r=0}^{\infty} rg(r)J_0(kr)\,dr \tag{A.96}$$

where J_0 is the Bessel function of the first kind, zeroth order, which means it is the function satisfying

$$x^2\frac{d^2(J_0(x))}{dx^2} + x\frac{d(J_0(x))}{dx} + x^2J_0(x) = 0 \tag{A.97}$$

with $J_0(0) = 1$.

Thus the Fourier transform of a radially symmetric function $g(r)$ is its Hankel transform:

$$H[g(r)] := G(k) = 2\pi\int_{r=0}^{\infty} rg(r)J_0(kr)\,dr. \tag{A.98}$$

A.4.2 Derivative rule

The 2D Fourier transform of a derivative of a radially symmetric function can be expressed in terms of the Fourier transform of the original function, and hence of its Hankel transform. It is calculated from equation (A.83) by integration by parts, and yields:

$$\widetilde{\nabla_i f(r)} = ik_iH\left[f(r)\right]. \tag{A.99}$$

A.4.3 Rule for multiplication by r^2

Recall the definition of the Hankel transform:

$$F(k) = 2\pi\int_0^{\infty} f(r)rJ_0(kr)\mathrm{d}r. \tag{A.100}$$

Now let us consider a function $g(r) = r^2f(r)$ where we already know the Hankel transform of f, denoted $F(k)$. We have

$$G(k) = 2\pi\int_0^{\infty} g(r)rJ_0(kr)\mathrm{d}r = 2\pi\int_0^{\infty} f(r)r^3J_0(kr)\mathrm{d}r. \tag{A.101}$$

If we briefly change variables to $x = kr$ we can write this as

$$G(k) = 2\pi k^{-4} \int_0^\infty f(x/k) x^3 J_0(x) \mathrm{d}x. \tag{A.102}$$

Since J_0 satisfies Bessel's equation (A.97), this can also be written as

$$G(k) = -2\pi k^{-4} \int_0^\infty f(x/k) x^2 \left[x \frac{d^2(J_0(x))}{dx^2} + \frac{d(J_0(x))}{dx} \right] \mathrm{d}x. \tag{A.103}$$

Changing variables back to r gives

$$G(k) = -2\pi \int_0^\infty r^2 \left[r J_0''(kr) + k^{-1} J_0'(kr) \right] f(r) \mathrm{d}r. \tag{A.104}$$

Finally, noting that

$$\frac{d}{dk} J_0(kr) = r J_0'(kr) \tag{A.105}$$

gives

$$\begin{aligned} G(k) &= -2\pi \int_0^\infty \left[\frac{d^2}{dk^2} J_0(kr) + k^{-1} \frac{d}{dk} J_0(kr) \right] r f(r) \mathrm{d}r \\ &= -2\pi \left[\frac{d^2}{dk^2} + k^{-1} \frac{d}{dk} \right] \int_0^\infty J_0(kr) r f(r) \mathrm{d}r \\ &= - \left[\frac{d^2}{dk^2} + k^{-1} \frac{d}{dk} \right] F(k). \end{aligned} \tag{A.106}$$

This gives us a straightforward method to calculate the Hankel transform of $r^2 f(r)$ where we already know $F(k)$.

A.4.4 Good functions and Generalised functions

The theory we use to take the Hankel transform is that of the "good functions" described in chapter 2 of Lighthill's book on Generalised Function Theory [44]. All of the definitions, theorems and examples can be found there. What is done below is to try and highlight the key definitions and theorems used in our derivation of the Hankel transforms of r^{-1} and $r \operatorname{erf}(\lambda r)$, needed to calculate the mobility relations.

The definitions needed are those of *good functions*, *fairly good functions*, and the relations between them; and the definition of *generalised functions* and a theorem about their convergence.

Definition 1 *A* good function *is one which is everywhere differentiable any number of times and such that it and all its derivatives are* $O(|x|^{-N})$ *as* $|x| \to \infty$*, for all* N*.*

Example: e^{-x^2}

Definition 2 *A* fairly good function *is one which is everywhere differentiable any number of times and such that it and all its derivatives are* $O(|x|^{N})$ *as* $|x| \to \infty$ *for some* N*.*

Example: Any polynomial.

Theorem 1 *The derivative of a good function is a good function. The sum of two good functions is a good function. The product of a fairly good function and a good function is a good function.*

The important bit of this theorem is the last sentence, "The product of a fairly good function and a good function is a good function". We will rely on this in many steps of the derivation of the Hankel transform of $r\,\mathrm{erf}(\lambda r)$.

Definition 3 *A sequence* $f_n(x)$ *of good functions is called* regular *if, for any good function* $F(x)$ *whatever, the limit*

$$\lim_{n\to\infty} \int_{-\infty}^{\infty} f_n(x)F(x)dx, \tag{A.107}$$

exists.

Example: The sequence $f_n(x) = e^{-x^2/n}$ is regular.

Definition 4 *Two regular sequences of good functions are called* equivalent *if, for any good function* $F(x)$ *whatever, the limit (A.107) is the same for each sequence.*

Example: The sequences $f_n(x) = e^{-x^2/n}$ and $f_n(x) = e^{-x^2/n^2}$ are equivalent.

Definition 5 *A* generalised function $f(x)$ *is defined as a regular sequence* $f_n(x)$ *of good functions, but two generalised functions are said to be equal if the corresponding regular sequences are equivalent. Thus each generalised function is really the class of all regular sequences equivalent to a given sequence. The integral*

$$\int_{-\infty}^{\infty} f(x)F(x)dx \tag{A.108}$$

of the product of a generalised function $f(x)$ *and a good function* $F(x)$ *is defined as*

$$\lim_{n\to\infty} = \int_{-\infty}^{\infty} f_n(x)F(x)dx. \tag{A.109}$$

This is permissible because the limit is the same for all equivalent sequences $f_n(x)$*.*

Example: The sequence $f_n(x) = e^{-x^2/n}$ and all its equivalent sequences define a generalised function $I(x)$ such that.

$$\int_{-\infty}^{\infty} I(x)F(x)dx = \int_{-\infty}^{\infty} F(x)dx. \tag{A.110}$$

This last definition is also very important and we will use it repeatedly in the rest of this section. The key points to note are Theorem (1) and Definition (5). They work by allowing us to neglect parts of the calculation which otherwise would not converge without using generalised functions.

A.4.5 Hankel Transform of r^{-1}

Equipped with the knowledge of generalised functions and the derivative rule we can begin to calculate the Hankel transforms needed for the mobility relationships. We start by calculating the Hankel transform of r^{-1} and deriving from it the Hankel transform of r, and then move on to our target of the Hankel transform of $r\,\mathrm{erf}(\lambda r)$.

The Hankel transform of $f(r)$ is defined as

$$H(k) = 2\pi \int_0^{\infty} f(r) r J_0(kr) dr \tag{A.111}$$

as in equation (Hankeldef). An alternative form for J_0 is given in equation (9.1.18) of Abramowitz and Stegun [2] as

$$J_0(kr) = \frac{1}{\pi}\int_0^\pi \cos(kr\cos\theta)d\theta. \tag{A.112}$$

Considering the transform of $f(r) = r^{-1}$ means that we will have to treat $f(r)$ as a generalised function: that is, as a regular sequence of good functions. The good functions which we shall be using are $r^{-1}\exp[-r/n]$: as the product of the fairly good function r^{-1} and the good function $\exp[-r/n]$ we know that each of these is a good function. This results in the integral

$$H[r^{-1}] = H(k) = \lim_{n\to\infty} 2\pi\int_0^\infty \exp[-r/n]J_0(kr)dr, \tag{A.113}$$

and substituting in our integral representation of the Bessel function we get

$$H(k) = \lim_{n\to\infty} 2\int_0^\infty \exp[-r/n]\int_0^\pi \cos(kr\cos(\theta))d\theta dr. \tag{A.114}$$

This where the convergence properties of good functions are used, as if we take the limit $n\to\infty$ first the r-integral would not converge uniformly. Swapping the order of integration and writing $\cos(kr\cos\theta) = \Re[\exp(irk\cos(\theta))]$, we carry out the r integration:

$$\begin{aligned}
H(k) &= \lim_{n\to\infty} 2\int_0^\pi\int_0^\infty \exp[-r/n]\Re[\exp(ikr\cos(\theta))]\,\mathrm{d}r\mathrm{d}\theta \\
&= \lim_{n\to\infty} 2\int_0^\pi\int_0^\infty \Re[\exp(ikr\cos(\theta) - r/n)]\,\mathrm{d}r\mathrm{d}\theta \\
&= \lim_{n\to\infty} 2\int_0^\pi \left[\Re\left\{\frac{\exp(ikr\cos(\theta) - r/n)}{ik\cos(\theta) - 1/n}\right\}\right]_{r=0}^\infty \mathrm{d}\theta \\
&= \lim_{n\to\infty} 2\int_0^\pi \Re\left[\frac{-1}{ik\cos(\theta) - 1/n}\right]\mathrm{d}\theta \\
&= \lim_{n\to\infty} 2\int_0^\pi \Re\left[\frac{n + ikn^2\cos(\theta)}{1 + k^2n^2\cos^2(\theta)}\right]\mathrm{d}\theta \\
&= \lim_{n\to\infty} 2\int_0^\pi \frac{n}{1 + k^2n^2\cos^2(\theta)}\mathrm{d}\theta.
\end{aligned} \tag{A.115}$$

Due to the symmetry of $\cos^2\theta$ over $[0,\pi]$ we can say

$$H(k) = \lim_{n\to\infty} 4\int_0^{\pi/2} \frac{n}{1 + k^2n^2\cos^2\theta}\mathrm{d}\theta. \tag{A.116}$$

Using the substitution $y = \tan(\theta)/\sqrt{1+n^2k^2}$ this becomes

$$\begin{aligned} H(k) = &\lim_{n\to\infty} 4\int_0^\infty \frac{n}{(1+n^2k^2)(1+y^2)}\sqrt{1+n^2k^2}\mathrm{d}y \\ =&\frac{4}{k}\int_0^\infty \frac{1}{(1+y^2)}\mathrm{d}y. \end{aligned} \tag{A.117}$$

Now taking the substitution $y = \tan(\theta)$ again,

$$H[r^{-1}] = \frac{4}{k}\int_0^{\pi/2}\mathrm{d}\theta = \frac{2\pi}{k}. \tag{A.118}$$

A.4.6 Hankel transform of $r\,\mathrm{erf}(\lambda r)$

The final quantity whose Hankel transform we need is $r\,\mathrm{erf}(\lambda r)$. To do this we first transform the generalised function defined by the sequence $f_n(r) = r^{-1}\,\mathrm{erf}(\lambda r)e^{-r/n}$ and then use our rule for multiplication by r^2 to deduce the transform of the generalised function defined by $g_n(r) = r\,\mathrm{erf}(\lambda r)e^{-r/n}$.

We start, as in section A.4.5, from the definition of the Hankel transform, and substitute the definition of the error function erf and Parseval's form for the Bessel function, equation (A.112):

$$\begin{aligned} H[r^{-1}\,\mathrm{erf}(\lambda r)] = F(k) &= 2\pi\int_0^\infty \mathrm{erf}(\lambda r)J_0(kr)\mathrm{d}r \\ &= \lim_{n\to\infty}\int_0^\infty \mathrm{erf}(\lambda r)J_0(kr)e^{-r/n}\mathrm{d}r \\ &= \frac{1}{\pi}\frac{2}{\sqrt{\pi}}\lim_{n\to\infty}\int_{\theta=0}^{\pi}\int_{r=0}^{\infty}\int_{t=0}^{\lambda r} e^{-t^2}\mathrm{d}t\cos(kr\cos\theta)e^{-r/n}\mathrm{d}r\,\mathrm{d}\theta \\ &= \frac{1}{\pi}\frac{2}{\sqrt{\pi}}\lim_{n\to\infty}\int_{\theta=0}^{\pi}\int_{r=0}^{\infty}\int_{t=0}^{\lambda r} e^{-t^2}\mathrm{d}t\Re\left\{\exp\left[ikr\cos\theta - r/n\right]\right\}\mathrm{d}r\,\mathrm{d}\theta \\ &= \frac{1}{\pi}\frac{2}{\sqrt{\pi}}\lim_{n\to\infty}\int_{\theta=0}^{\pi}\Re\left\{\int_{r=0}^{\infty}\int_{t=0}^{\lambda r} e^{-t^2}\mathrm{d}t\exp\left[ikr\cos\theta - r/n\right]\mathrm{d}r\right\}\mathrm{d}\theta. \end{aligned} \tag{A.119}$$

Now we integrate by parts over r, differentiating the error function and inte-

grating the rest:

$$\begin{aligned}
F(k) =& \frac{1}{\pi}\frac{2}{\sqrt{\pi}} \lim_{n\to\infty} \int_{\theta=0}^{\pi} \Re \left\{ \left[\int_{t=0}^{\lambda r} e^{-t^2} \mathrm{d}t \frac{\exp(ikr\cos\theta - r/n)}{ik\cos\theta - 1/n} \right]_{r=0}^{\infty} \right. \\
& \left. - \int_{r=0}^{\infty} \lambda \exp[-\lambda^2 r^2] \frac{\exp(ikr\cos\theta - r/n)}{ik\cos\theta - 1/n} \mathrm{d}r \right\} \mathrm{d}\theta \\
=& \frac{\lambda}{\pi}\frac{2}{\sqrt{\pi}} \lim_{n\to\infty} \int_{\theta=0}^{\pi} \Re \left\{ \frac{n(ink\cos\theta + 1)}{(n^2k^2\cos^2\theta + 1)} \right. \\
& \left. \times \int_{r=0}^{\infty} \exp\left[-\lambda^2 r^2 - \frac{r}{n} + ikr\cos\theta \right] \mathrm{d}r \right\} \mathrm{d}\theta \\
=& \frac{\lambda}{\pi}\frac{2}{\sqrt{\pi}} \int_{\theta=0}^{\pi} \Re \left\{ \frac{i}{k\cos\theta} \int_{r=0}^{\infty} \exp\left[-\lambda^2 r^2 + ikr\cos\theta \right] \mathrm{d}r \right\} \mathrm{d}\theta \\
=& -\frac{\lambda}{\pi}\frac{2}{\sqrt{\pi}} \int_{\theta=0}^{\pi} \int_{r=0}^{\infty} \exp\left[-\lambda^2 r^2 \right] \frac{\sin(kr\cos\theta)}{k\cos\theta} \mathrm{d}r\mathrm{d}\theta \\
=& -\frac{\lambda}{\pi}\frac{4}{\sqrt{\pi}} \int_{\theta=0}^{\pi/2} \int_{r=0}^{\infty} \exp\left[-\lambda^2 r^2 \right] \frac{\sin(kr\cos\theta)}{kr\cos\theta} r\mathrm{d}r\mathrm{d}\theta.
\end{aligned} \tag{A.120}$$

Returning to Cartesian coordinates:

$$\begin{aligned}
F(k) =& -\frac{\lambda}{\pi}\frac{4}{\sqrt{\pi}} \int_{x=0}^{\infty} \int_{y=0}^{\infty} \exp\left[-\lambda^2(x^2+y^2) \right] \frac{\sin(kx)}{kx} \mathrm{d}y\mathrm{d}x \\
=& -\frac{\lambda}{\pi}\frac{4}{\sqrt{\pi}} \int_{x=0}^{\infty} \exp\left[-\lambda^2 x^2 \right] \frac{\sin(kx)}{kx} \mathrm{d}x \int_{y=0}^{\infty} \exp\left[-\lambda^2 y^2 \right] \mathrm{d}y \\
=& -\frac{\lambda}{\pi}\frac{4}{\sqrt{\pi}} \int_{x=0}^{\infty} \exp\left[-\lambda^2 x^2 \right] \frac{\sin(kx)}{kx} \mathrm{d}x \frac{\sqrt{\pi}}{2\lambda} \\
=& -\frac{2}{\pi} \int_{x=0}^{\infty} \exp\left[-\lambda^2 x^2 \right] \frac{\sin(kx)}{kx} \mathrm{d}x.
\end{aligned} \tag{A.121}$$

We now use the power series expansion of $\sin(kx)$:

$$\begin{aligned}
F(k) =& -\frac{2}{\pi} \int_{x=0}^{\infty} \exp\left[-\lambda^2 x^2 \right] \frac{1}{kx} \sum_{n=0}^{\infty} \frac{(-1)^n}{(2n+1)!} (kx)^{2n+1} \mathrm{d}x \\
=& -\frac{2}{\pi} \sum_{n=0}^{\infty} \frac{(-1)^n k^{2n}}{(2n+1)!} \int_{x=0}^{\infty} x^{2n} \exp\left[-\lambda^2 x^2 \right] \mathrm{d}x.
\end{aligned} \tag{A.122}$$

We shall calculate the integral by iteration: define

$$P_n = \int_{x=0}^{\infty} x^{2n} \exp\left[-\lambda^2 x^2 \right] \mathrm{d}x, \tag{A.123}$$

and we have (for $n \geq 1$)

$$\begin{aligned} P_n =& \frac{-1}{2\lambda^2}\int_{x=0}^{\infty} x^{2n-1}(-2\lambda^2 x)e^{-\lambda^2x^2}\mathrm{d}x \\ =& \frac{-1}{2\lambda^2}\left\{\left[x^{2n-1}e^{-\lambda^2x^2}\right]_{x=0}^{\infty} - \int_{x=0}^{\infty}(2n-1)x^{2n-2}e^{-\lambda^2x^2}\mathrm{d}x\right\} \\ =& \frac{(2n-1)}{2\lambda^2}\int_{x=0}^{\infty} x^{2n-2}e^{-\lambda^2x^2}\mathrm{d}x = \frac{(2n-1)}{2\lambda^2}P_{n-1} \\ P_0 =& \int_{x=0}^{\infty} e^{-\lambda^2x^2}\mathrm{d}x = \frac{\sqrt{\pi}}{2\lambda} \end{aligned} \tag{A.124}$$

and so we deduce that

$$P_n = \frac{(2n-1)!!}{2^n\lambda^{2n}}\frac{\sqrt{\pi}}{2\lambda} = \frac{\sqrt{\pi}(2n-1)!}{2^{n+1}\lambda^{2n+1}2^{n-1}(n-1)!} = \frac{\sqrt{\pi}(2n-1)!}{2^{2n}\lambda^{2n+1}(n-1)!} \tag{A.125}$$

(where !! denotes the odd factorial operation) and hence

$$\begin{aligned} F(k) =& -\frac{2}{\pi}\sum_{n=0}^{\infty}\frac{(-1)^n k^{2n}}{(2n+1)!}P_n \\ =& -\frac{2}{\sqrt{\pi}}\sum_{n=0}^{\infty}\frac{(2n-1)!}{(2n+1)!}\frac{(-1)^n k^{2n}}{2^{2n}\lambda^{2n+1}(n-1)!} \\ =& -\frac{2}{k\sqrt{\pi}}\sum_{n=0}^{\infty}\frac{1}{2n(2n+1)}\frac{(-1)^n k^{2n+1}}{2^{2n}\lambda^{2n+1}(n-1)!} \\ =& -\frac{2}{k\sqrt{\pi}}\sum_{n=0}^{\infty}\frac{(-1)^n}{n!}\frac{1}{(2n+1)}\left(\frac{k}{2\lambda}\right)^{2n+1}. \end{aligned} \tag{A.126}$$

We now note that

$$\begin{aligned} \sum_{n=0}^{\infty}\frac{(-1)^n}{n!}\frac{y^{2n+1}}{(2n+1)} &= \int_{t=0}^{y}\sum_{n=0}^{\infty}\frac{(-1)^n}{n!}t^{2n}\mathrm{d}t \\ &= \int_{t=0}^{y}\sum_{n=0}^{\infty}\frac{(-t^2)^n}{n!}\mathrm{d}t \\ &= \int_{t=0}^{y}\exp[-t^2]\mathrm{d}t = \frac{\sqrt{\pi}}{2}\operatorname{erf}(y), \end{aligned} \tag{A.127}$$

so

$$H[r^{-1}\operatorname{erf}(\lambda r)] = F(k) = -\frac{2}{k\sqrt{\pi}}\frac{\sqrt{\pi}}{2}\operatorname{erf}\left(\frac{k}{2\lambda}\right) = -\frac{1}{k}\operatorname{erf}\left(\frac{k}{2\lambda}\right) \tag{A.128}$$

Now we can use our rule for multiplication by r^2, equation (A.106), to deduce

the Hankel transform of $r\,\mathrm{erf}(\lambda r)$, which is the result we will need:

$$\begin{aligned} H[r\,\mathrm{erf}(\lambda r)] &= -\left(\frac{d^2}{dk^2}+\frac{1}{k}\frac{d}{dk}\right) H[r^{-1}\,\mathrm{erf}(\lambda r)] \\ &= -\left(\frac{d^2}{dk^2}+\frac{1}{k}\frac{d}{dk}\right)\left[-\frac{1}{k}\,\mathrm{erf}\left(\frac{k}{2\lambda}\right)\right] \\ &= \left(\frac{d}{dk}+\frac{1}{k}\right)\frac{d}{dk}\left[\frac{1}{k}\,\mathrm{erf}\left(\frac{k}{2\lambda}\right)\right] \\ &= \left(\frac{d}{dk}+\frac{1}{k}\right)\left[-\frac{1}{k^2}\,\mathrm{erf}\left(\frac{k}{2\lambda}\right)+\frac{1}{k\lambda\sqrt{\pi}}\exp\left[-\left(\frac{k}{2\lambda}\right)^2\right]\right] \\ &= \frac{1}{k^3}\,\mathrm{erf}\left(\frac{k}{2\lambda}\right)-\frac{1}{\lambda\sqrt{\pi}}\left(\frac{1}{k^2}+\frac{1}{2\lambda^2}\right)\exp\left[-\left(\frac{k}{2\lambda}\right)^2\right]. \end{aligned} \tag{A.129}$$

This gives us the Hankel transform, and hence the Fourier transform, of the scalar function $r\,\mathrm{erf}(\lambda r)$. Along with the derivatives rule for Fourier transforms, this will allow us to calculate both $\widetilde{\mathbf{J}^k}$ and the transforms of the mobility relations, $\widetilde{\mathcal{L}^w\mathbf{J}^k}$.

This however shows any problem with our choice of sigmoidal curve. We multiply our mobility relation by the Hankel transform of $r\,\mathrm{erf}(\lambda r)$ but the relation does not decay after a the Hankel transform as it does in the three dimensional case of the Fourier transform used by Brady et el [13]. The problem occurs with any mobility relation containing a term of order $\geq k^3$ which we multiply by the Hankel transform of $r\,\mathrm{erfc}(\lambda r)$. Looking at the first term of the transform we have $1/k^3\,\mathrm{erf}(k/2\lambda) \to 0$ which is $O(1/k^3)$ as $k \to \infty$. As previously stated the problem occurs if whatever is multiplying $H[r\,\mathrm{erf}(\lambda r)]$ has order greater than of equal to k^3. Let's take a_{ij} as an example,

$$a_{ij} = \left(\frac{3}{4}+\frac{1}{4}\nabla^2\right) J_{ij} \tag{A.130}$$

with

$$J_{ij} = (\delta_{ij}\nabla^3 - \nabla_i\nabla_j)r \tag{A.131}$$

Using the derivative rule the reciprocal space relation is

$$a^k_{ij} = 1/4(\delta_{ij}k^4 - k_ik_jk^2 - 3\delta_{ij}k^2 + 3k_ik_j)H[r\,\mathrm{erf}(\lambda r)] \tag{A.132}$$

This is $O(k^4)$ hence when summation of the reciprocal space occurs and $k \to \infty$ the contribution from the reciprocal space to Ewald summation is non convergent.

To solve this problem we would need to find another sigmoidal function, try the Hankel transform and see if the function still decays. Determing an appropriate plan of attack is beyond this thesis.

We shall still list include the real mobility relations as they are still correct and useful (subject to change of sigmoidal curve) and they make some minor corrections to some of Brady's mobility relations [21]. Due to the problem with the Hankel transform we will not list the reciprocal space relations.

A.5 Real and Reciprocal Space Mobility Relations

There are six mobility relations, which we will consider in turn, giving expressions for their summed forms in real and reciprocal space. As discussed in section A.1.1, these tensors and pseudo-tensors relate the velocities and background flow gradient to the forces, torques and stresslets acting on the particles.

Within this section we will repeatedly use derivatives of the error function $\mathrm{erf}\,(\lambda r)$, so for convenience we introduce the notation

$$\mathcal{E} = \frac{2}{\sqrt{\pi}} \exp(-\lambda^2 r^2). \tag{A.133}$$

for the quantity which will appear regularly.

In equations (A.92) and (A.93) we found

$$\begin{aligned} \mathbf{w}^{\alpha\alpha;rep} =& \mathbf{w}^{\alpha\alpha} + \Sigma'_{m,n} \mathcal{L}^w \mathbf{J}^r(\mathbf{x}_{mn}) - L^{-2} \int \mathcal{L}^w \mathbf{J}^r(\mathbf{x}') \, \mathrm{d}^2\mathbf{x}' \\ &+ L^{-2} \Sigma'_{m,n} \widetilde{\mathcal{L}^w \mathbf{J}^k}(\mathbf{k}_{mn}) - \mathcal{L}^w \mathbf{J}^k(\mathbf{0}) \end{aligned} \tag{A.134}$$

and

$$\begin{aligned}\mathbf{w}^{\alpha\beta;rep}(\mathbf{x}) = \Sigma_{m,n}\mathcal{L}^w\mathbf{J}^r(\mathbf{x}+\mathbf{x}_{mn}) - L^{-2}\int \mathcal{L}^w\mathbf{J}^r(\mathbf{x}+\mathbf{x}')\,\mathrm{d}^2\mathbf{x}' \\ + L^{-2}\Sigma'_{m,n}\exp\left[i\mathbf{k}_{mn}\cdot\mathbf{x}\right]\widetilde{\mathcal{L}^w\mathbf{J}^k}(\mathbf{k}_{mn}).\end{aligned} \tag{A.135}$$

Let us consider first the second-rank tensor $\mathbf{a}$. This gives the relationship between the translational velocity and the force. In its standard form it is

$$a_{ij} = \frac{1}{4}(3 + \nabla^2\nabla^2 - \nabla_i\nabla_j\nabla^2 + 3\delta_{ij}\nabla^2 - 3\nabla_i\nabla_j)\,r. \tag{A.136}$$

When used in the Ewald summation and split into real and reciprocal space parts it becomes

$$a^r_{ij} = \frac{1}{4}(3 + \nabla^2\nabla^2 - \nabla_i\nabla_j\nabla^2 + 3\delta_{ij}\nabla^2 - 3\nabla_i\nabla_j)\,(r\,\mathrm{erfc}(\lambda\,r)), \tag{A.137}$$

$$a^k_{ij} = \frac{1}{4}(3 + \nabla^2\nabla^2 - \nabla_i\nabla_j\nabla^2 + 3\delta_{ij}\nabla^2 - 3\nabla_i\nabla_j)\,(r\,\mathrm{erf}(\lambda\,r)). \tag{A.138}$$

Using this notation, we can write the summed contributions as

$$\begin{aligned}\mathbf{a}^{\alpha\alpha;rep} &= \mathbf{a}^{\alpha\alpha} + \Sigma'_{m,n}\mathbf{a}^r(\mathbf{x}_{mn}) - L^{-2}\int \mathbf{a}^r(\mathbf{x}')\,\mathrm{d}^2\mathbf{x}' \\ &\quad + L^{-2}\Sigma'_{m,n}\widetilde{\mathbf{a}^k}(\mathbf{k}_{mn}) - \mathbf{a}^k(\mathbf{0}) \qquad \text{(A.139)} \\ \mathbf{a}^{\alpha\beta;rep}(\mathbf{x}) &= \Sigma_{m,n}\mathbf{a}^r(\mathbf{x}+\mathbf{x}_{mn}) - L^{-2}\int \mathbf{a}^r(\mathbf{x}+\mathbf{x}')\,\mathrm{d}^2\mathbf{x}' \\ &\quad + L^{-2}\Sigma'_{m,n}\exp\left[i\mathbf{k}_{mn}\cdot\mathbf{x}\right]\widetilde{\mathbf{a}^k}(\mathbf{k}_{mn}). \qquad \text{(A.140)}\end{aligned}$$

The quantities we need to know are $\mathbf{a}^{\alpha\alpha}$, which was given in equation (A.22), and the new quantities $\mathbf{a}^r$, $\widetilde{\mathbf{a}^k}$ and $\mathbf{a}^k(\mathbf{0})$. We will show these, and their equivalents for the other five mobility tensors, in the following sections.

A.5.1 Tensor a

The real space contribution $\mathbf{a}^r$ is simply an expansion of equation (A.137):

$$
\begin{aligned}
a_{ij}^{r} = \delta_{ij} & \left\{ \left(\frac{3}{4r} + \frac{1}{2r^3} \right) \operatorname{erfc}(\lambda\, r) \right. \\
& \left. + \frac{1}{2} \left(4\lambda^7 r^4 + 3\lambda^3 r^2 - 20\lambda^5 r^2 - \frac{9}{2}\lambda + 14\lambda^3 + \lambda\, r^{-2} \right) \mathcal{E} \right\} \\
& + e_i e_j \left\{ \left(\frac{3}{4r} - \frac{3}{2r^3} \right) \operatorname{erfc}(\lambda\, r) \right. \\
& \left. + \frac{1}{2} \left(-4\lambda^7 r^4 - 3\lambda^3 r^2 + 16\lambda^5 r^2 + \frac{3}{2}\lambda - 2\lambda^3 - 3\lambda r^{-2} \right) \mathcal{E} \right\}
\end{aligned}
\tag{A.141}
$$

in which the vector $e_i = r_i/r$ is the unit vector of $\mathbf{r}$.

The rest of the mobility relations follow on in much the same vein and are given from here on without any further explanation.

A.5.2 Pseudo-Tensor b

The b_{ij} relation in its lone form is

$$
b_{ij} = -\frac{3}{4}\epsilon_{ijk}\frac{e_k}{r^2} = \frac{3}{8}\epsilon_{ijk}\nabla^2\nabla_k r \tag{A.142}
$$

The real space contribution is

$$
b_{ij}^{r} = \frac{3}{8}\epsilon_{ijk}\nabla^2\nabla_k \left(r \operatorname{erfc}(\lambda\, r) \right) \tag{A.143}
$$

which expands to become

$$
b_{ij}^{r} = -\frac{3}{4}\epsilon_{ijk}e_k \left[\left\{ \frac{1}{r^2} \operatorname{erfc}(\lambda\, r) + \frac{\lambda}{r} \left(1 - 6\lambda^2 r^2 + 2\lambda^4\, r^4 \right) \mathcal{E} \right\} \right] \tag{A.144}
$$

A.5.3 Tensor c

The real-space contribution to c_{ij} is

$$
c_{ij}^{r} = -\frac{3}{16} \left(\delta_{ij}\nabla^2 - \nabla_i\nabla_j \right) \nabla^2 \left(r \operatorname{erfc}(r\, \lambda) \right) \tag{A.145}
$$

which expands to become

$$
\begin{aligned}
c_{ij}^{r} = &-\frac{3}{8}\delta_{ij}\left[\frac{\operatorname{erfc}(\lambda r)}{r^3} + \frac{\lambda}{r^2}(1 + 14\lambda^2 r^2 - 20\lambda^4 r^4 + 4\lambda^6 r^6)\mathcal{E}\right] \\
&+ \frac{3}{8}e_i e_j\left[\frac{3}{r^3}\operatorname{erfc}(\lambda r) + \frac{\lambda}{r^2}(3 + 2\lambda^2 r^2 - 16\lambda^4 r^4 + 4\lambda^6 r^6)\mathcal{E}\right]
\end{aligned}
\tag{A.146}
$$

A.5.4 Tensor g

The g_{ijk} relation in its lone form is

$$
g_{ijk} = -\left(\frac{3}{8} + \frac{1}{10}\nabla^2\right)(\delta_{jk}\nabla_i\nabla^2 + \delta_{ik}\nabla_j\nabla^2 - 2\nabla_i\nabla_j\nabla_k)r. \tag{A.147}
$$

In real space the contribution is given by

$$
g_{ijk}^{r} = -\left(\frac{3}{8} + \frac{1}{10}\nabla^2\right)(\delta_{jk}\nabla_i\nabla^2 + \delta_{ik}\nabla_j\nabla^2 - 2\nabla_i\nabla_j\nabla_k)(r\operatorname{erfc}(\lambda r)) \tag{A.148}
$$

which expands to become

$$
\begin{aligned}
g_{ijk}^{r} = \frac{3}{8}\Bigg\{ &-X_1\left[e_i\delta_{jk} + e_j\delta_{ik}\right] - 2\left(\frac{1}{r^2}\operatorname{erfc}(\lambda r) + X_2\right)e_k\delta_{ij} \\
&+ 2\left(\frac{3}{r^2}\operatorname{erfc}(\lambda r) - X_3\right)e_i e_j e_k \\
&+ \frac{4}{15}\Bigg[\left(\frac{12}{r^4}\operatorname{erfc}(\lambda r) - X_4\right)\left[e_i\delta_{jk} + e_j\delta_{ik}\right] + \left(\frac{12}{r^4}\operatorname{erfc}(\lambda r) - X_5\right)e_k\delta_{ij} \\
&- \left(\frac{60}{r^4}\operatorname{erfc}(\lambda r) + X_6\right)e_i e_j e_k\Bigg]\Bigg\}
\end{aligned}
\tag{A.149}
$$

with

$$
\begin{aligned}
X_1 &= \frac{2\lambda}{r}(4\lambda^2 r^2 - 2\lambda^4 r^4)\mathcal{E} \\
X_2 &= \frac{\lambda}{r}(1 - 2\lambda^2 r^2)\mathcal{E} \\
X_3 &= -\frac{\lambda}{r}(3 + 2\lambda^2 r^2 - 4\lambda^4 r^4)\mathcal{E} \\
X_4 &= -4\frac{\lambda}{r^3}(3 + 2\lambda^2 r^2 + 26\lambda^4 r^4 - 26\lambda^6 r^6 + 4\lambda^8 r^8)\mathcal{E} \\
X_5 &= -4\frac{\lambda}{r^3}(3 + 2\lambda^2 r^2 - 16\lambda^4 r^4 + 4\lambda^6 r^6)\mathcal{E} \\
X_6 &= 4\frac{\lambda}{r^3}(15 + 10\lambda^2 r^2 + 4\lambda^4 r^4 - 40\lambda^6 r^6 + 8\lambda^8 r^8)\mathcal{E}.
\end{aligned}
$$

A.5.5 Pseudo-tensor h

The h_{ijk} relation in its lone form is

$$
h_{ijk} = -\frac{3}{16}\left(\epsilon_{ikl}\nabla^2\nabla_j\nabla_l + \epsilon_{jkl}\nabla^2\nabla_i\nabla_l\right) r \tag{A.150}
$$

The real space contribution is

$$
h^r_{ijk} = -\frac{3}{16}\left(\epsilon_{ikl}\nabla^2\nabla_j\nabla_l + \epsilon_{jkl}\nabla^2\nabla_i\nabla_l\right)\left(r\,\mathrm{erfc}(\lambda\, r)\right) \tag{A.151}
$$

which expands to become

$$
\begin{aligned}
h^r_{ijk} = -\frac{3}{16}\Bigg\{ &\frac{6}{r^3}\,\mathrm{erfc}(\lambda\, r) + 2\frac{\lambda}{r^2}(3 + 2\lambda^2 r^2 \\
&-16\lambda^4 r^4 + 4\lambda^6 r^6)\mathcal{E}\Big\}\left[\epsilon_{ikl}e_j e_l + \epsilon_{jkl}e_i e_l\right].
\end{aligned} \tag{A.152}
$$

A.5.6 The tensor m

The m_{ijkl} relation in its lone form is

$$
\begin{aligned}
m_{ijkl} =& \frac{3}{4}\nabla_i\nabla_j\nabla_k\nabla_l r + \frac{3}{20}\nabla^2\nabla_i\nabla_j\nabla_k\nabla_l r \\
&- \frac{3}{16}[\delta_{ik}\nabla_j\nabla_l + \delta_{il}\nabla_j\nabla_k + \delta_{jk}\nabla_i\nabla_l + \delta_{jl}\nabla_i\nabla_k]\nabla^2 r \\
&- \frac{3}{80}\nabla^2\nabla^2(\delta_{ik}\nabla_j\nabla_l + \delta_{il}\nabla_j\nabla_k + \delta_{jk}\nabla_i\nabla_l + \delta_{jl}\nabla_i\nabla_k) r
\end{aligned} \tag{A.153}
$$

in which we have kept some terms involving $\nabla^2\nabla^2 r$ because of their physical derivation from equation (A.13) in terms of the Stokes Oseen tensor.
The real space contribution expands to become

$$\begin{aligned}
m^r_{ijkl} = &-\frac{3}{4}[e_ie_je_ke_l]\{15r^{-3}\operatorname{erfc}\lambda r + Y_1\mathcal{E}\} \\
&+\frac{3}{8}[\delta_{ik}e_je_l + \delta_{il}e_je_k + \delta_{jk}e_ie_l + \delta_{jl}e_ie_k]\{3r^{-3}\operatorname{erfc}\lambda r + Y_2\mathcal{E}\} \\
&+\frac{3}{4}[\delta_{ij}e_ke_l + \delta_{kl}e_ie_j]\{3r^{-3}\operatorname{erfc}\lambda r + Y_3\mathcal{E}\} \\
&+\frac{3}{4}[\delta_{ik}\delta_{jl} + \delta_{il}\delta_{jk}]\{Y_4\mathcal{E}\} - \frac{3}{4}[\delta_{kl}\delta_{ij}]\{r^{-3}\operatorname{erfc}\lambda r + Y_5\mathcal{E}\} \\
&+\frac{3}{20}[e_ie_je_ke_l]\{210r^{-5}\operatorname{erfc}\lambda r + Y_6\mathcal{E}\} \\
&-\frac{3}{20}[\delta_{ik}e_je_l + \delta_{il}e_je_k + \delta_{jk}e_ie_l + \delta_{jl}e_ie_k]\{30r^{-5}\operatorname{erfc}\lambda r + Y_7\mathcal{E}\} \\
&-\frac{3}{20}[\delta_{ij}e_ke_l + \delta_{kl}e_ie_j]\{30r^{-5}\operatorname{erfc}\lambda r + Y_8\mathcal{E}\} \\
&+\frac{3}{20}[\delta_{ik}\delta_{jl} + \delta_{il}\delta_{jk}]\{6r^{-5}\operatorname{erfc}\lambda r + Y_9\mathcal{E}\} \\
&+\frac{3}{20}[\delta_{kl}\delta_{ij}]\{6r^{-5}\operatorname{erfc}\lambda r + Y_{10}\mathcal{E}\}
\end{aligned} \tag{A.154}$$

with

$$\begin{aligned}
Y_1 =&\lambda r^{-2}(15 + 10\lambda^2r^2 + 4\lambda^4r^4 - 8\lambda^6r^6) \\
Y_2 =&\lambda r^{-2}(3 + 2\lambda^2r^2 + 8\lambda^4r^4 - 4\lambda^6r^6) \\
Y_3 =&\lambda r^{-2}(3 + 2\lambda^2r^2 - 4\lambda^4r^4) \\
Y_4 =&\lambda r^{-2}(-4\lambda^2r^2 + 2\lambda^4r^4) \\
Y_5 =&\lambda r^{-2}(1 - 2\lambda^2r^2) \\
Y_6 =&2\lambda r^{-4}(105 + 70\lambda^2r^2 + 28\lambda^4r^4 + 8\lambda^6r^6 - 96\lambda^8r^8 + 16\lambda^{10}r^{10}) \\
Y_7 =&2\lambda r^{-4}(15 + 10\lambda^2r^2 + 4\lambda^4r^4 + 32\lambda^6r^6 - 30\lambda^8r^8 + 4\lambda^{10}r^{10}) \\
Y_8 =&2\lambda r^{-4}(15 + 10\lambda^2r^2 + 4\lambda^4r^4 - 40\lambda^6r^6 + 8\lambda^8r^8) \\
Y_9 =&2\lambda r^{-4}(3 + 2\lambda^2r^2 + 26\lambda^4r^4 - 26\lambda^6r^6 + 4\lambda^8r^8) \\
Y_{10} =&2\lambda r^{-4}(3 + 2\lambda^2r^2 - 16\lambda^4r^4 + 4\lambda^6r^6).
\end{aligned} \tag{A.155}$$

test [29]

Bibliography

[1] Legion cluster ucl.

[2] Milton Abramowitz and Irene A Stegun. *Handbook of Mathematical Functions with Formulas, Graphs, and Mathematical Tables*. Dover, New York, 1964.

[3] P M Adler and H Brenner. Spatially periodic suspensions of convex particles in linear shear flows. *Journal of Multiphase Flow*, 11:361, 1985.

[4] P A Arp and S G Mason. The kinetics of flowing dispersions: IX. Doublets of rigid spheres (experimental). *Journal of Colloid and Interface Science*, 61(1):44–61, 1977.

[5] P A Arp and S G Mason. The kinetics of flowing dispersions: VIII. Doublets of rigid spheres (theoretical). *Journal of Colloid and Interface Science*, 61(1):21–43, 1977.

[6] G K Batchelor and J T Green. The hydrodynamic interaction of two small freely-moving spheres in a linear flow field. *Journal of Fluid Mechanics*, 56(2):375–400, 1972.

[7] C W J Beenakker. Ewald sum of the Rotne-Prager tensor. *Journal of Chemical Physics*, 83:1581, 1986.

[8] F Blanc, F Peters, and E Lemaire. *Journal of Rheology*.

[9] G Bossis and J F Brady. Dynamic simulations of sheared suspensions. I. General method. *Journal of Chemical Physics*, 80:5141–5154, 1984.

[10] J F Brady and G Bossis. The rheology of concentrated suspensions of spheres in simple shear-flow by numerical-simulation. *Journal of Fluid Mechanics*, 155:105–129, 1985.

[11] J F Brady and G Bossis. Stokesian Dynamics. *Annual Reviews of Fluid Mechanics*, 20:111–157, 1988.

[12] J F Brady and J F Morris. Microstructure of strongly sheared suspensions and its impact on rheology and diffusion. *Journal of Fluid Mechanics*, 348(1):103–139, 1997.

[13] J F Brady, R J Phillips, J C Lester, and G Bossis. Dynamic simulation of hydrodynamically interacting suspensions. *Journal of Fluid Mechanics*, 195:257–280, 1988.

[14] M D A Cooley and M E O'Neill. On the slow rotation of a sphere about a diameter parallel to a nearby plane wall. *IMA Journal of Applied Mathematics*, 4(2):163–173, 1968.

[15] F R da Cunha and E J Hinch. Shear-induced dispersion in a dilute suspension of rough spheres. *Journal of Fluid Mechanics*, 309:211–223, 1996.

[16] T Darden, D York, and L Pedersen. Particle Mesh Ewald: An $n\log(n)$ method for Ewald sums in large systems. *Journal of Chemical Physics*, 98:10089–10092, 1993.

[17] R H Davis. Effects of surface roughness on a sphere sedimenting through a dilute suspension of neutrally buoyant spheres. *Physics of Fluids*, 4(12):2607–2619, 1992.

[18] R H Davis and N A Hill. Hydrodynamic diffusion of a sphere sedimenting through a dilute suspension of neutrally buoyant spheres. *Journal of Fluid Mechanics*, 236(1):513–533, 1992.

[19] R H Davis, Y Zhao, K P Galvin, and H J Wilson. *Philosophical Transactions: Mathematical, Physical and Engineering Sciences*.

[20] D I Dratler and W R Schowalter. Dynamic simulation of suspensions of non-Brownian hard spheres. *Journal of Fluid Mechanics*, 325:53–77, 1996.

[21] L Durlofsky, J F Brady, and G Bossis. Dynamic simulation of hydrodynamically interacting particles. *Journal of Fluid Mechanics*, 180:21–49, 1987.

[22] A Einstein. Eine neue Bestimmung der Moleküledimensionen. *Annalen der Physik*, 19(2):289–306, 1906.

[23] M L Ekiel-Jeżewska, F Feuillebois, N Lecoq, K Masmoudi, R Anthore, F Bostel, and E Wajnryb. Hydrodynamic interactions between two spheres at contact. *Physical Review E*, 59(3):3182–3191, Mar 1999.

[24] P P Ewald. Die Berechnung optischer und elektrostatischer Gitterpotentiale. *Annalen der Physik*, 369:253–287, 1921.

[25] A Fall, N Huang, F Bertrand, G Ovarlez, and D Bonn. Shear thickening of cornstarch suspensions as a reentrant jamming transition. *Physical Review Letters*, 100:018301, 2008.

[26] R S Farr, J R Melrose, and R C Ball. Kinetic theory of jamming in hard-sphere startup flows. *Physical Review E*, 55:7203, 1997.

[27] G G Fuller and L G Leal. Flow birefringence of dilute polymer solutions in two-dimensional flows. *Rheologica Acta*, 19:580–600, 1980.

[28] G G Fuller and L G Leal. Flow birefringence of concentrated polymer solutions in two-dimensional flows. *Journal of Polymer Science: Polymer Physics Edition*, 19:557–587, 1981.

[29] K P Galvin, Y Zhao, and R H Davis. Time-averaged hydrodynamic roughness of a noncolloidal sphere in low Reynolds number motion down an inclined plane. *Physics of Fluids*, 13(11):3108–3119, 2001.

[30] P Ganatos, R Pfeffer, and S Weinbaum. A numerical-solution technique for three-dimensional Stokes flows, with application to the motion of strongly interacting spheres in a plane. *Journal of Fluid Mechanics*, 84:79–111, 1978.

[31] H Giesekus. Strömungen mit konstantem Geschwindigkeitsgradienten und die Bewegung von darin suspendierten Teilchen. *Rheologica Acta*, 2(2):112–122, 1962.

[32] R W Hockney and J W Eastwood. *Computer simulation using particles*. I.O.P. Publishing Philadelphia, 1988. ISBN 978-0852743928.

[33] P J Hoogerbrugge and J M V A Koelman. Simulating microscopic hydrodynamic phenomena with dissipative particle dynamics. *Europhysics Letters*, 19:155–160, 1992.

[34] D J Jeffrey and Y Onishi. Calculation of the resistance and mobility functions for two unequal rigid spheres in low-Reynolds-number flow. *Journal of Fluid Mechanics*, 139:261–290, 1984.

[35] A S Khair and J F Brady. On the motion of two particles translating with equal velocities through a colloidal dispersion. *Proceedings of the Royal Society*, 463:223–240, 2007.

[36] S Kim and R T Mifflin. The resistance and mobility functions of two equal spheres in low-Reynolds-number flow. *Physics of Fluids*, 28:2033–2045, 1985.

[37] Sangtae Kim and Seppo J Karrila. *Microhydrodynamics: Principles and Selected Applications*. Butterworth Heinemann, 1st edition, 1991.

[38] L N Krishnamurthy, E C Weigert, N J Wagner, and D C Boris. The shear viscosity of polyampholyte (gelatin) stabilized colloidal dispersions. *Journal of Colloid and Interface Science*, 280:264–275, 2004.

[39] S D Kulkarni and J F Morris. Ordering transition and structural evolution under shear in Brownian suspensions. *Journal of Rheology*, 53:417–439, 2009.

[40] G J Kynch. The slow motion of two or more spheres through a viscous fluid. *Journal of Fluid Mechanics*, 5:193–208, 1959.

[41] A J C Ladd. Numerical simulations of particulate suspensions via a discretized Boltzmann equation. Part 1. Theoretical foundation. *Journal of Fluid Mechanics*, 271:285–309, 1994.

[42] A J C Ladd. Numerical simulations of particulate suspensions via a discretized Boltzmann equation. Part 2. Numerical results. *Journal of Fluid Mechanics*, 271:311–339, 1994.

[43] O A Ladyzhenskaya. *The mathematical theory of viscous incompressible flow*. Gordon and Breach, 1963.

[44] M J Lighthill. *Introduction To Fourier Analysis and Generalised Functions*. Cambridge University Press, 1958.

[45] A Malidi and O G Harlen. Numerical simulations of suspensions of elastic particles in polymer melts. In *Proceedings of the XVth International Congress on Rheology*. The Society of Rheology 80th Annual Meeting, 2008.

[46] R St J Manley and S G Mason. The viscosity of suspensions of spheres: A note on the particle interaction coefficient. *Canadian Journal of Chemistry*, 32:763, 1954.

[47] R W O'Brien. A method for the calculation of the effective transport properties of suspensions of interacting particles. *Journal of Fluid Mechanics*, 91(01):17–39, 1979.

[48] M E O'Neill and S R Majumdar. Asymmetrical slow viscous fluid motions caused by the translation or rotation of two spheres. Part II: Asymptotic forms of the solutions when the minimum clearance between the spheres approaches zero. *Zeitschrift für Angewandte Mathematik und Physik*, 21(2):180–187, 1970.

[49] I Rampall, J R Smart, and D T Leighton. The influence of surface roughness on the particle-pair distribution function of dilute suspensions of non-colloidal spheres in simple shear flow. *Journal of Fluid Mechanics*, 339:1–24, 1997.

[50] S Sami. Stokesian Dynamics simulations of Brownian suspensions in extensional flow, chapter 5. Master's thesis, California Institute of Technology, 1996.

[51] A S Sangani and G Mo. An $O(N)$ algorithm for Stokes and Laplace interactions of particles. *Physics of Fluids*, 8:1990–2010, 1996.

[52] A Sierou and J F Brady. Accelerated Stokesian Dynamics simulations. *Journal of Fluid Mechanics*, 448:115–146, 2001.

[53] J R Smart, S Beimfohr, and D T Leighton. Measurement of the translational and rotational velocities of a noncolloidal sphere rolling down a smooth inclined plane at loq reynolds.

[54] J R Smart and D T Leighton. Measurement of the hydrodynamic surface roughness of non-colloidal spheres. *Physics of Fluids* A, 1(1):52–60, 1989.

[55] M Swaroop and J F Brady. The bulk viscosity of suspensions. *Journal of Rheology*, 51:409–428, 2007.

[56] M Tabatabaian and R G Cox. Effect of contact forces on sedimenting spheres in Stokes flow. *International Journal of Multiphase Flow*, 17(3):395–413, 1991.

[57] V Vand. Viscosity of solutions and suspensions. I. Theory. *Journal of Physical Chemistry*, 52:277–299, 1948.

[58] V Vand. Viscosity of solutions and suspensions. II. Experimental determination of the viscosityconcentration function of spherical suspensions. *Journal of Physical Chemistry*, 52:300–314, 1948.

[59] N D Vassileva, D van den Ende, F Mugele, and J Mellema. Restructuring and break-up of two-dimensional aggregates in shear flow. *Langmuir*, 22(11):4959–4967, 2006.

[60] N D Vassileva, D van den Ende, F Mugele, and J Mellema. Fragmentation and erosion of two-dimensional aggregates in shear flow. *Langmuir*, 23(5):2352–2361, 2007.

[61] S Weinbaum, P Ganatos, and Z-Y Yan. Numerical multipole and boundary integral equation techniques in Stokes flow. *Annual Reviews of Fluid Mechanics*, 22:275, 1990.

[62] H J Wilson. An analytic form for the pair distribution function and rheology of a dilute suspension of rough spheres in plane strain flow. *Journal of Fluid Mechanics*, 534:97–114, 2005.

[63] H J Wilson and R H Davis. The viscosity of a dilute suspension of rough spheres. *Journal of Fluid Mechanics*, 421:339–367, 2000.

[64] H J Wilson and R H Davis. Shear stress of a monolayer of rough spheres. *Journal of Fluid Mechanics*, 452:425–441, 2002.

[65] H J Wilson and R H Davis. The effect of different particle contacts on suspension rheology. *XXI ICTAM*, 2004.

[66] L Yang, J R T Seddon, T Mullin, C del Pino, and J Ashmore. The motion of a rough particle in a Stokes flow adjacent to a boundary. *Journal of Fluid Mechanics*, 557:337–346, 2006.

[67] G K Youngren and A Acrivos. Stokes flow past a particle of arbitrary shape: a numerical method of solution. *Journal of Fluid Mechanics*, 69:377–403, 1975.

[68] S Zeng, E T Kerns, and R H Davis. The nature of particle contacts in sedimentation. *Physics of Fluids*, 8(6):1389–1396, 1996.

[69] Y Zhao, K P Galvin, and R H Davis. Motion of a sphere down a rough plane in a viscous fluid. *International Journal of Multiphase Flow*, 28(11):1787–1800, 2002.